

CLIMATE CHANGE MONITORING REPORT 2022

July 2023

Published by the
Japan Meteorological Agency

3-6-9 Toranomom, Minato City, Tokyo 105-8431, Japan

E-mail iao-jma@met.kishou.go.jp

**CLIMATE CHANGE MONITORING REPORT
2022**

July 2023

JAPAN METEOROLOGICAL AGENCY

Preface

The Japan Meteorological Agency (JMA) has published annual reports under the title of Climate Change Monitoring Report since 1996 to provide up-to-date information on climate change in Japan and around the world based on the outcomes of its observations and its monitoring of the atmosphere and oceans.

The Intergovernmental Panel on Climate Change (IPCC) Sixth Assessment Report (AR6) emphasizes that the frequency and intensity of extreme weather events are expected to continue increasing as global warming progresses.

Many parts of the world experienced extreme weather events in 2022, including record-high temperatures in Europe and China and heavy rains in Pakistan. Record-high temperatures were also seen from late June to early July in Japan, with studies revealing a significant link to global warming (see News I in this report). JMA's Meteorological Research Institute has conducted research on the effect of climate change on individual events, such as the Heavy Rain Event of July 2017 in Northern Kyushu, the Heavy Rain Event of July 2018, and Typhoon Hagibis (T1919). This report touches on the outcomes of such work.

Against this background, JMA released Climate Change in Japan 2020 – Assessment Report on Observed and Projected Climate Change in the Atmosphere, on Land and in Oceans – in December 2020 in conjunction with Japan's Ministry of Education, Culture, Sports, Science and Technology (MEXT). The report presents scientific expertise on climate change in Japan, including differences observed and future projections for the global average temperature changes detailed in the RCP 2.6 and 8.5 scenarios (called the “2°C and 4°C warming scenarios” in the report). The observation details in the report are updated from the latest observation data in this Climate Change Monitoring Report.

In December 2022, MEXT and JMA compiled 15 sets of climate projection data developed by various organizations along with its guidebook. The compilation is designed to support detailed climate change impact assessment and promotion of climate change adaptation based on familiarity with an overview of scientific findings from Climate Change in Japan 2020 and the Climate Change Monitoring Report.

This report is intended to raise awareness of climate change, and is expected to be particularly useful to related organizations and stakeholders worldwide in their responses to climate change.



OBAYASHI Masanori
Director-General
Japan Meteorological Agency

Index

News	1
I Record-breaking high temperatures from late June to early July 2022	1
II Record-high sea surface temperatures southeast of Hokkaido and east of Honshu from July 2022	5
III Stratospheric aerosol spread and climatic effects associated with the 2022 Hunga Tonga-Hunga Ha'apai volcanic eruption	7
IV Largest annual increase in atmospheric methane concentrations since records began	10
Chapter 1 Climate in 2022	13
1.1 Global climate summary	13
1.2 Climate in Japan	17
1.2.1 Annual characteristics.....	17
1.2.2 Seasonal characteristics	19
1.3 Atmospheric circulation and oceanographic conditions	23
1.3.1 Characteristics of individual seasons	23
1.3.2 Global average temperature in the troposphere	34
1.3.3 Asian summer monsoon	35
1.3.4 Tropical cyclones over the western North Pacific and the South China Sea.....	36
Chapter 2 Climate Change	38
2.1 Greenhouse gases'	38
2.1.1 Concentration of carbon dioxide.....	39
2.1.2 Concentration of methane.....	44
2.1.3 Concentration of nitrous oxide	45
2.1.4 Concentration of halocarbons	46
2.2 Aerosols and surface radiation	50
2.2.1 Aerosols.....	50
2.2.2 Kosa (Aeolian dust).....	51
2.2.3 Solar radiation and downward infrared radiation.....	51
2.3 Temperature	54
2.3.1 Global surface temperature.....	54
2.3.2 Surface temperature over Japan.....	56
2.3.3 Long-term trends of extreme temperature events in Japan	57

2.3.4	Urban heat island effect at urban stations in Japan	58
2.4	Precipitation	61
2.4.1	Global precipitation over land	61
2.4.2	Precipitation over Japan.....	61
2.4.3	Long-term trends of extreme precipitation events in Japan	62
2.5	Snow depth and snow cover	68
2.5.1	Snow cover in the Northern Hemisphere.....	68
2.5.2	Snow depth and Snowfall in Japan	70
2.6	Tropical cyclones over the western North Pacific and the South China Sea	73
2.7	Phenology of cherry blossoms and acer leaves in Japan.....	74
2.8	Sea surface temperature	75
2.8.1	Global sea surface temperature.....	75
2.8.2	Global ocean heat content.....	76
2.8.3	Sea surface temperature (around Japan)	76
2.9	El Niño/La Niña and PDO (Pacific Decadal Oscillation)	78
2.9.1	El Niño/La Niña	78
2.9.2	Pacific Decadal Oscillation.....	79
2.10	Sea levels around Japan.....	80
2.11	Sea ice.....	82
2.11.1	Sea ice in Arctic and Antarctic areas.....	82
2.11.2	Sea ice in the Sea of Okhotsk	84
2.12	Ocean carbon dioxide and ocean acidification	85
2.12.1	Ocean carbon dioxide	85
2.12.2	Ocean acidification	88

<i>Explanatory note on detection of statistical significance in long-term trends.....</i>	<i>92</i>
--	------------------

<i>Glossary.....</i>	<i>94</i>
-----------------------------	------------------

<i>References.....</i>	<i>100</i>
-------------------------------	-------------------

News

I Record-breaking high temperatures from late June to early July 2022

- Summer temperatures in 2022 were higher than normal across Japan. In particular, the period from late June to early July was characterized by record-high temperatures in eastern and western parts of the country. Ten-day temperature anomalies were the highest since 1946 at $+4.0^{\circ}\text{C}$ over eastern Japan, $+3.2^{\circ}\text{C}$ over western Japan in late June, and $+3.2^{\circ}\text{C}$ over northern Japan in early July.
- The record-high temperatures observed from late June to early July are primarily attributed to a northward meandering of the upper-tropospheric subtropical jet stream near Japan, unprecedented intensification of the upper-tropospheric high and the Pacific High at surface level, and a persistent warming trend.

I.1 Climate conditions

Northward extension of the Pacific High at surface level strengthened in late June, and record-high temperatures were recorded over eastern and western Japan toward early July (Figure I.1). Ten-day temperature anomalies were the highest since 1946 at $+4.0^{\circ}\text{C}$ over eastern Japan, $+3.2^{\circ}\text{C}$ over western Japan in late June, and $+3.2^{\circ}\text{C}$ over northern Japan in early July. Also from late June to early July, 24 of the 914 stations in Japan observed record-breaking high temperatures. In particular, Isesaki in Gunma Prefecture recorded daily maxima above 40°C on June 25/29 and July 1, and Tokyo also observed daily maxima above 35°C for a record nine consecutive days from June 25 onward.

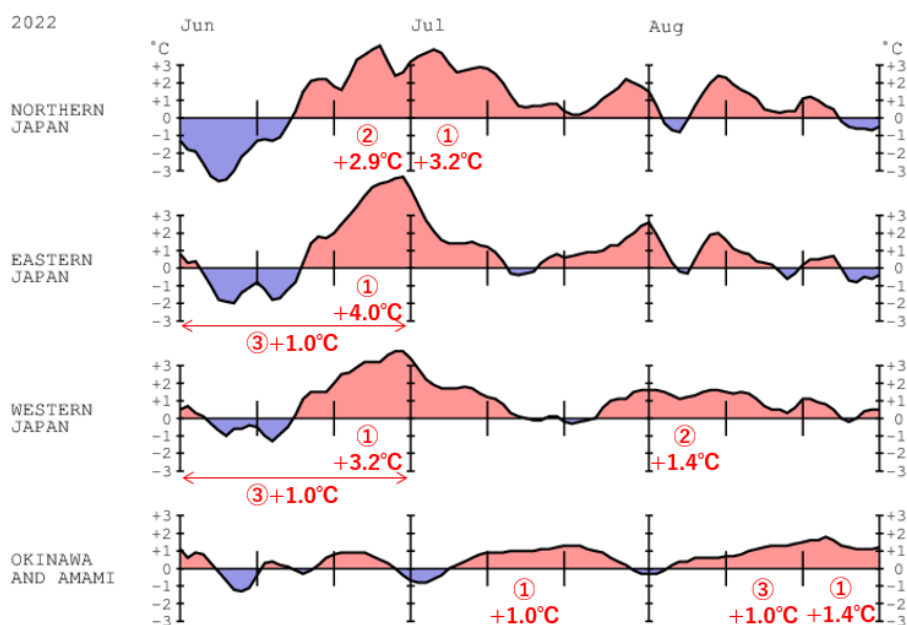


Figure I-1. Time-series representations of 5-day running mean temperature anomalies [degree C] for June – August 2022

The base period for the normal is 1991 – 2020. The red circled numbers and values indicate the rank from highest average temperatures since 1946 and anomalies for each month and each ten-day period (up to the top three).

I.2 Characteristics of large-scale atmospheric circulation

The Japan Meteorological Agency (JMA), in conjunction with the Tokyo Climate Center Advisory Panel on Extreme Climatic Events (a JMA body staffed by prominent academics and researchers in the field of climate science), investigated and summarized factors considered to have contributed to the record-high temperatures as described below.

Near Japan, both the upper-level high and the Pacific High were significantly strengthened for this time of year (Figures I.2 (a) and (b)). A tall anticyclone characterized by warm air covered the area around Japan, and enhanced solar radiation associated with strong downward motion and persistent stable clear skies brought warm conditions to the region. Combined with the influence of localized over-mountain air currents, this resulted in record-breaking high temperatures exceeding 40°C in some areas.

The strengthened extension of the upper-level anticyclone toward Japan and the Pacific High were influenced by the continued significant northward meandering of the upper-level subtropical jet (STJ) near Japan. This meander may have been partly caused by a large meander of the jet stream over the North Atlantic to Europe, and its influence extended downstream (Figure I.2 (a)).

Extremely enhanced cumulus convective activity near the Philippines from late June onward compared to the normal (Figure I.3 (a)) was also associated with the strengthening of the Pacific High's extension toward Japan (Pacific–Japan (PJ) pattern, Figure I.3 (b)). In addition to higher-than-normal sea surface temperatures in the vicinity of the Philippines, the strengthening of an upper-level anticyclone near Japan (making the area more susceptible to upper-level cold air intrusion into the subtropical region to the south of the anticyclone) may have contributed to increased cumulus convective activity near the Philippines.

In addition to the strengthened Pacific High and upper-level anticyclones, a continued rising trend in global temperatures associated with global warming and significantly higher tropospheric temperatures in the Northern Hemisphere mid-latitudes since late 2020 may have further contributed to the record-breaking high temperatures observed. The persistence of high tropospheric temperatures in the mid-latitudes of the Northern Hemisphere is considered to have been influenced by the La Niña event that persisted from summer 2020 to spring 2021 and fall 2021 onward, resulting in lower temperatures in the troposphere over the tropics, while the STJ shifted northward from its normal position throughout the Northern Hemisphere. Event attribution analysis¹ conducted under the Advanced Research Program for Climate Change Prediction run by the Ministry of Education, Culture, Sports, Science and Technology (MEXT) in collaboration with JMA's Meteorological Research Institute of JMA indicates that the high temperatures observed had a periodicity as rare as once every 1,200 years with the same La Niña and other effects that would have occurred in the assumption that global warming had not affected the region. This suggests that global warming may have an impact on this case.

The large-scale atmospheric circulation characteristics of the record-high temperatures are summarized in Figure I.4.

¹ A method for probabilistic estimation of how much the occurrence of individual phenomena has changed due to global warming by comparing a number of simulation experiments conducted under past climate conditions using a climate model and simulations conducted under a scenario with no global warming caused by human activity.

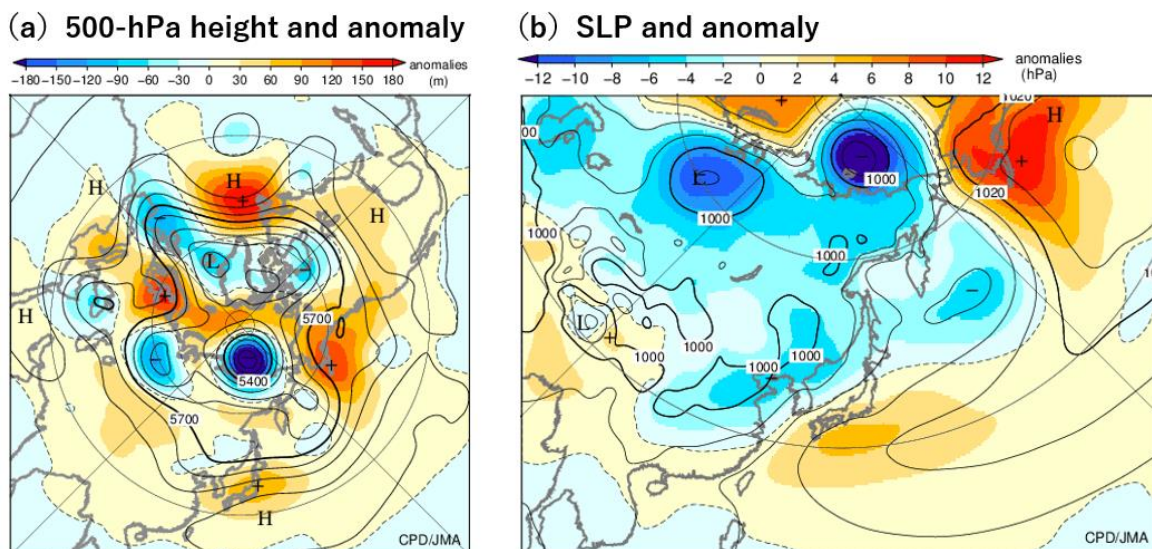


Figure I.2. (a) 500-hPa height (contours) and anomalies (shading), and (b) sea level pressure (contours) and anomalies (shading) averaged for late June 2022
Units are (a) m and (b) hPa. The base period of the normal is from 1991 to 2020. Information is based on the Japanese 55-year reanalysis (JRA-55) dataset.

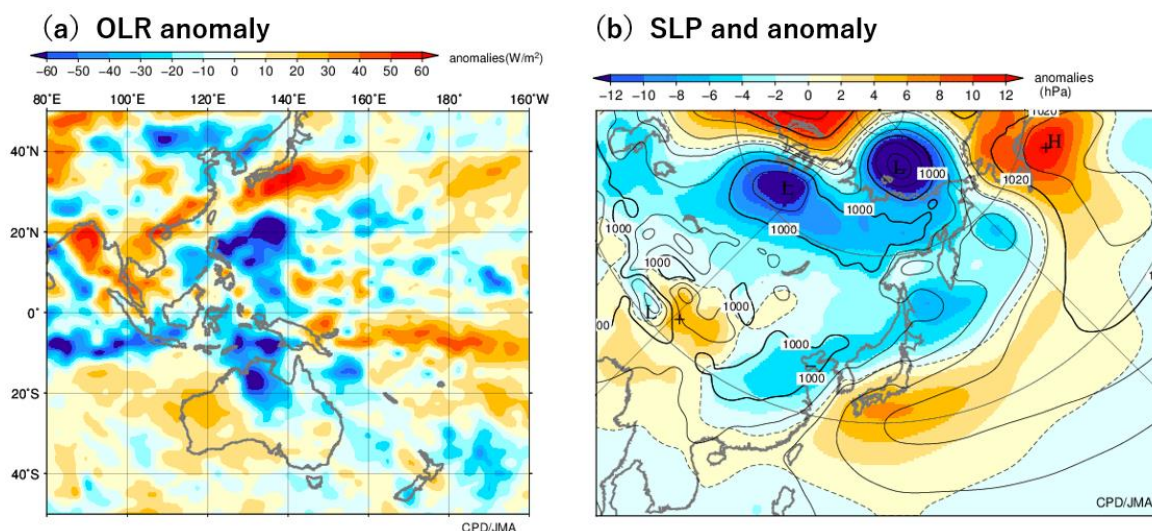


Figure I.3. (a) Outgoing longwave radiation (OLR) anomalies, and (b) sea level pressure (contours) and anomalies (shading) averaged from 25 to 29 June 2022
Units are (a) W/m² and (b) hPa. The base period of normal is from 1991 to 2020. (a) is from the National Oceanic and Atmospheric Administration (NOAA), and (b) is from the Japanese 55-year reanalysis (JRA-55) dataset.

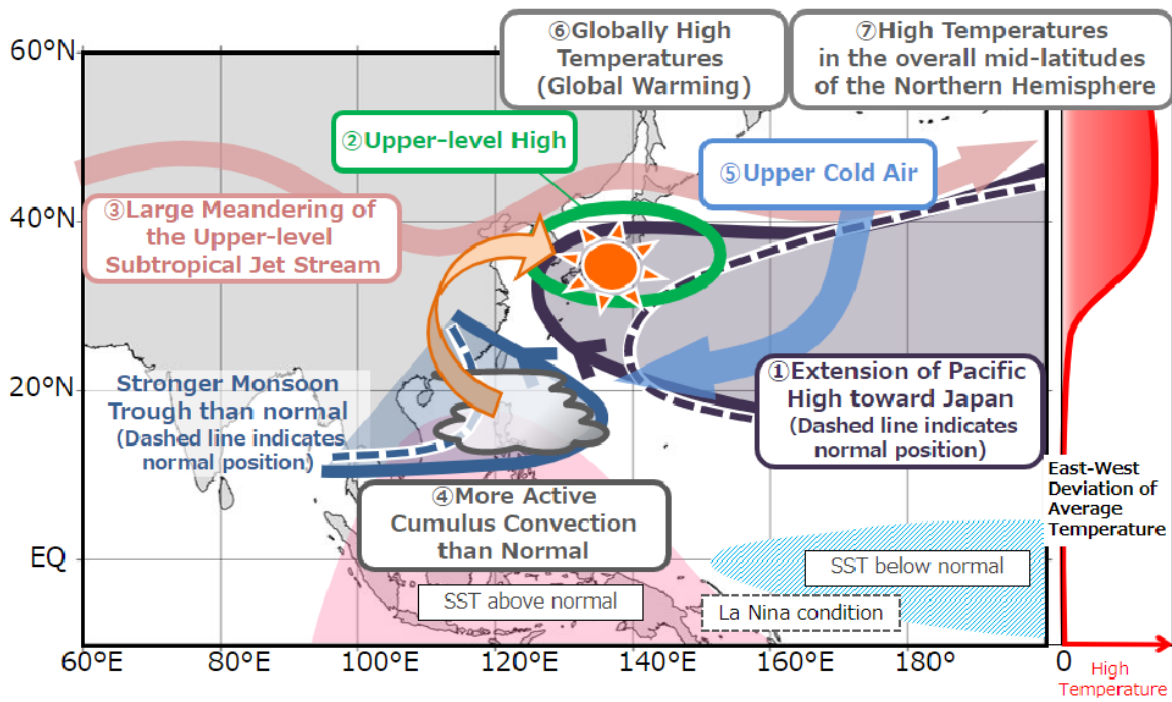


Figure I.4. Characteristics of atmospheric circulation bringing record-breaking high temperatures from late June to early July 2022

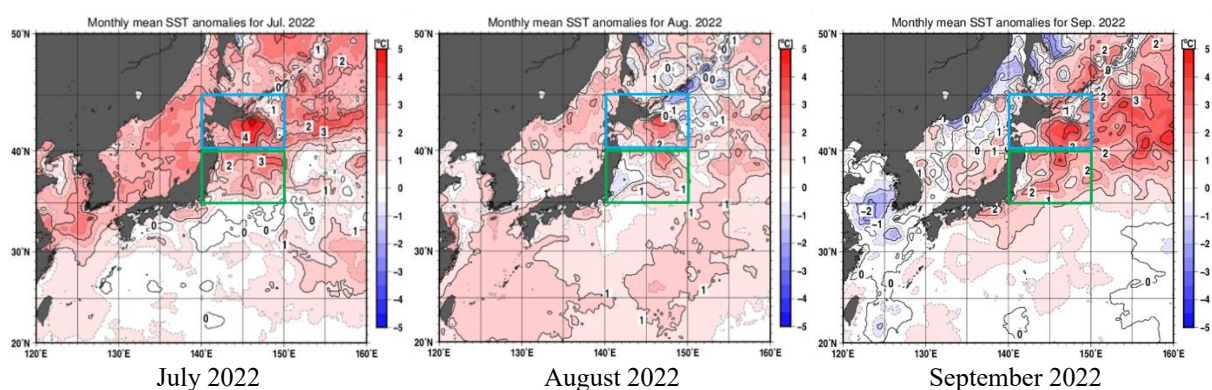
II Record-high sea surface temperatures southeast of Hokkaido and east of Honshu from July 2022

- Sea surface temperatures (SSTs) southeast of Hokkaido and east of Honshu have been above normal since July 2022. Monthly mean SSTs in July, October and November southeast of Hokkaido and in October and November east of Honshu were the highest since 1982.

The Japan Meteorological Agency monitors global SSTs around Japan and elsewhere using observation data from satellites, ships, buoys and other sources. In 2022, SSTs around Japan were above normal from July to December east of Japan (Figure II.1), where the mean value for 1991 – 2020 is used as the normal. Southeast of Hokkaido, SSTs were above normal in late June and around 3°C higher than normal in early July (Fig. II.2). Monthly mean SSTs in July were +2.3°C higher than normal, representing the highest value since 1982. SSTs in August were +0.9°C higher than normal, which was a lower increase than before, while those from September to December were +1.5 to +2.1°C higher than normal. Monthly mean SSTs in October and November were the highest, and those in September and December were the second highest. Time-series plotting of SST anomalies east of Honshu shows a pattern similar to that observed southeast of Hokkaido (Figure II.2). Monthly mean SSTs were the highest in October and November, the second highest in July and September, and the third highest in December.

Factors contributing to the record-high SSTs southeast of Hokkaido and east of Honshu from July 2022 include:

- Warm eddies and warm water from the Kuroshio current, where temperatures even at a depth of 100 m were higher than normal (Fig. II.3)
- Greater-than-normal solar radiation and warm humid air east of Honshu from late June to early July
- Greater-than-normal solar radiation east of Honshu in early and mid-September



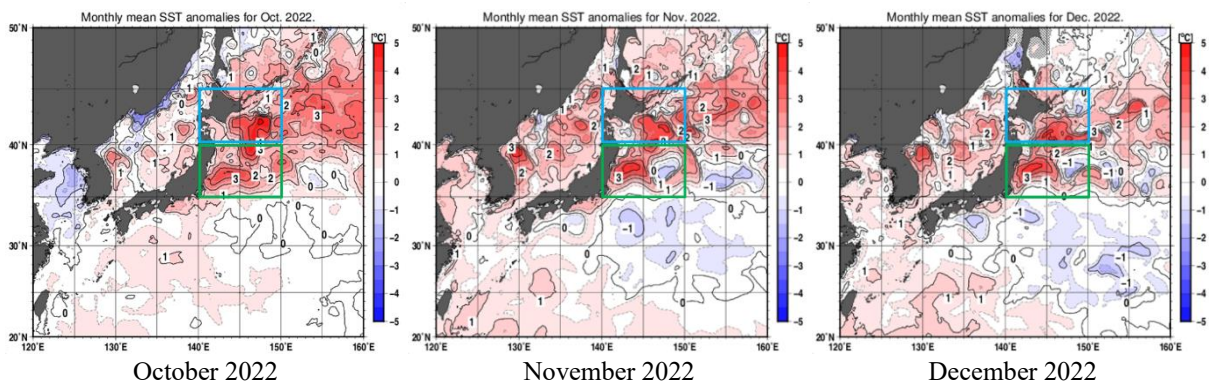


Fig. II.1 Distribution of monthly mean SST anomalies from July to December

The blue and green frames indicate the areas of southeast of Hokkaido and east of Honshu, respectively. Note that SSTs in the October - December period were preliminary values.

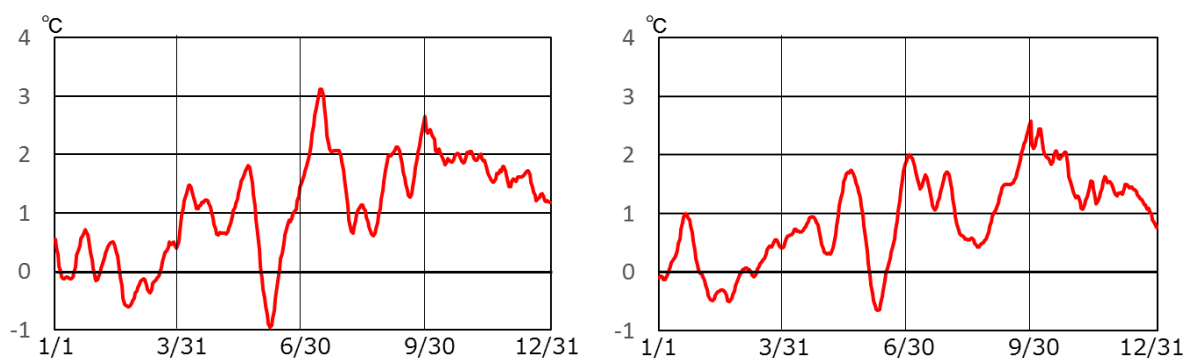


Fig. II.2 Daily SST anomalies for January - December 2022 in the southeast of Hokkaido (left) and east of Honshu (right).

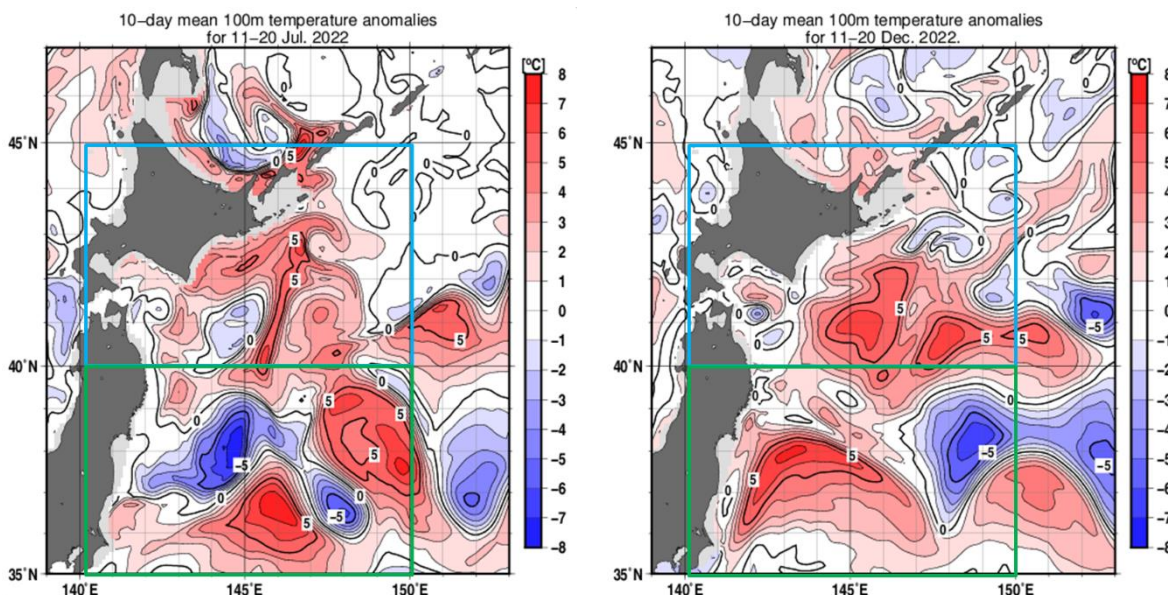


Fig. II.3 Distribution of water temperature anomalies at 100-m depth in mid-July (left) and mid-December (right) of 2022.

The blue and green frames indicate the areas of southeast of Hokkaido and east of Honshu, respectively. Normal values are averages from 1993 to 2017.

III Stratospheric aerosol spread and climatic effects associated with the 2022 Hunga Tonga-Hunga Ha'apai volcanic eruption

- The eruption of Hunga Tonga-Hunga Ha'apai in January 2022 injected 400,000 to 500,000 tons of sulfur dioxide (SO₂) into the stratosphere, which subsequently transformed into sulfate aerosols spreading across the latitudes. However, no related decrease in direct solar radiation had been observed in Japan as of 2022.
- Related climatic effects are likely to be limited because the amount of SO₂ ejected was significantly less than in previous major eruptions, which led to lower surface temperatures due to solar radiation blocking. However, the effects of the large amounts of water vapor injected into the stratosphere remain to be seen.

On 15 January 2022, a massive eruption occurred at Hunga Tonga-Hunga Ha'apai in the South Pacific's Tonga Islands. The volcanic explosivity index (VEI) was approximately 6 (Poli and Shapiro, 2022), which was comparable to that of the June 1991 Mt. Pinatubo eruption in the Philippines. In Japan, atmospheric pressure waves propagating southeast to northwest followed by tidal anomalies were observed in association with the eruption. Part of the volcanic plume observed by the Himawari-8 meteorological satellite (Figure III.1) crossed the stratopause and reached the mesosphere at an altitude of 57 km (based on parallax analysis using multiple satellites observation data) (Proud *et al.*, 2022).

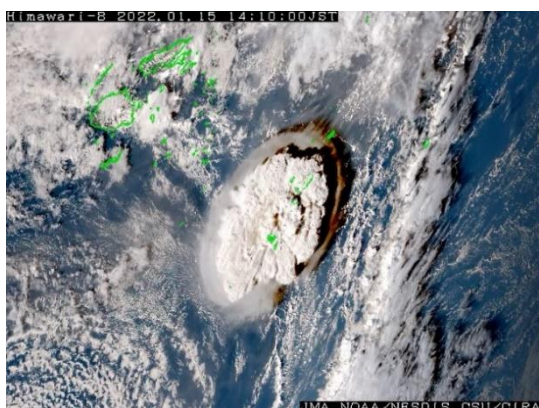


Figure III.1 Massive eruption of Hunga Tonga-Hunga Ha'apai in the Tonga Islands on 15 January 2022

Himawari-8 meteorological satellite True Color Reproduction (TCR) imagery for 14:10 JST on 15 January (JST: Japan Standard Time). TCR imagery is a product of collaboration among the Japan Meteorological Agency (JMA), the National Oceanic and Atmospheric Administration (NOAA)/NESDIS, and Colorado State University (CSU)/CIRA.

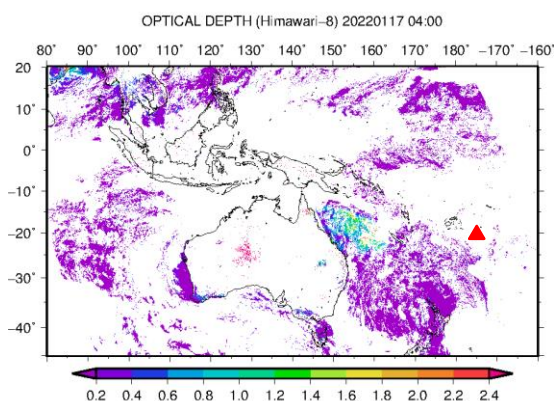


Figure III.2 Aerosol optical depth (AOD) two days after the eruption (17 January 2022, 13:00 JST) derived from Himawari-8 visible and near-infrared observation data

A large AOD area is seen off the northeastern coast of Australia. White areas are regions where calculation was impractical due to cloud, solar reflection or large satellite zenith angles. The red triangle indicates the volcano location.

In large eruptions, sulfur dioxide (SO₂; a major component of volcanic gases) reaches the stratosphere and is converted to sulfate aerosols via oxidation including reaction with water vapor. These aerosols disperse in the stratosphere and cause scattering of solar radiation, leading to lower global surface temperatures. In the 1991 Mt. Pinatubo eruption, approximately 20 million tons (20 Tg) of SO₂ injected into the stratosphere caused global mean surface temperature reductions of around 0.5°C for one year at most (IPCC, 2013). However, the amount of SO₂ injected into the stratosphere by the Hunga Tonga-Hunga Ha'apai eruption is estimated to have been significantly less, at 400,000 to 500,000 tons (0.4 to 0.5 Tg) (Carn *et al.*, 2022).

Sulfate aerosols forming from Hunga Tonga-Hunga Ha'apai SO₂ moved westward through layers around 30 km in altitude in the low-latitudes of the Southern Hemisphere, as observed by several satellites (Sellitto *et al.*, 2022; Legras *et al.*, 2022; Taha *et al.*, 2022). This was also seen in aerosol optical depths derived from Himawari-8 visible and near-infrared observation data (Kitajima *et al.*, 2021; Yoshida *et al.*, 2018) (Figure III.2). These migrating aerosols had circled the earth by late January, with plumes spreading to middle and high latitudes of the Southern Hemisphere by around February and others reaching middle and high latitudes of the Northern Hemisphere by around late March via meridional circulation in the stratosphere (Brewer-Dobson circulation). An aerosol layer near the altitude of 24 km was observed via lidar at JMA's Meteorological Research Institute in Tsukuba at the end of March (Figure III.3), and was also seen at European and Arctic stations from April to June 2022 (Khaykin *et al.*, 2022).

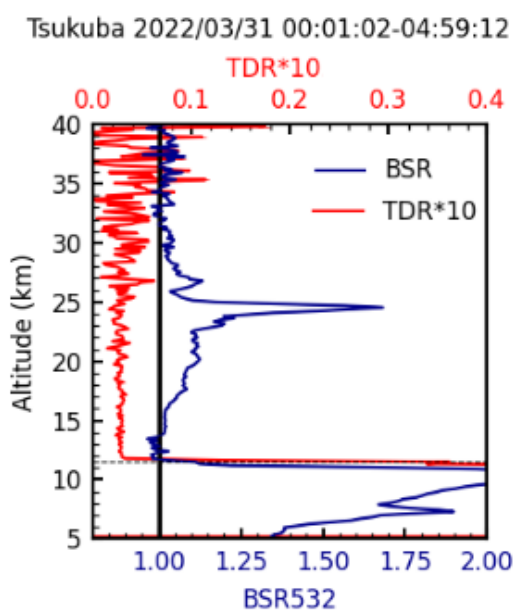


Figure III.3 Peak stratospheric aerosol layer associated with the Hunga Tonga-Hunga Ha'apai eruption as observed via Tsukuba lidar

The peak at an altitude of 24 km on 31 March was the first observation at Tsukuba (times: JST). The blue line (BSR) indicates the backscattering ratio (corresponding to the aerosol mixing ratio), and the red line (TDR) indicates the total depolarization ratio (an index of aerosol asphericity) (both observed at a wavelength of 532 nm). The almost-spherical characteristics of these sulfate aerosols are associated with low depolarization values. The dotted line around 11 km altitude indicates the tropopause, and clouds (mainly cirrus with high asphericity) are associated with altitudes below this.

Previous major volcanic eruptions have resulted in the global spread of aerosols, causing years of high stratospheric turbidity and reduced solar radiation on the ground. Figure III.4 shows long-term variations in background atmospheric turbidity coefficients² based on direct solar radiation³ observations at five stations in Japan (Section 2.2.1). The background values here were calculated from monthly minimum turbidity to minimize the influence of short-term tropospheric constituent fluctuations. Atmospheric turbidity coefficient is higher when direct solar radiation is reduced due to increase of atmospheric turbid substances including aerosols. Historically, large eruptions such as those at Mt. Agung (Indonesia) in 1963, Mt. El Chichón (Mexico) in 1982 and Mt. Pinatubo in 1991 have been followed by stratospheric aerosol-related reduction of direct solar radiation and increased atmospheric turbidity coefficients. However, no turbidity coefficient change was seen in 2022. The amount of SO₂ injected into the stratosphere from this eruption was likely too small to cause any detection of related changes. However, ongoing monitoring remains necessary in light of the fact that these coefficients began to rise during the period around 18 months after past eruptions (Yamauchi, 1995).

² The atmospheric turbidity coefficient indicates the ratio of the atmospheric optical depth affected by aerosols, water vapor and trace gases in the atmosphere to that uninfluenced by constituents other than air molecules such as oxygen and nitrogen in the atmosphere. Larger values indicate greater amounts of turbid matter in the air.

³ Direct solar radiation is the incident solar energy acting on the earth's surface from the sun. The atmospheric turbidity coefficient (also known as the Feussner-Dubois turbidity coefficient) can be calculated from direct solar radiation amounts.

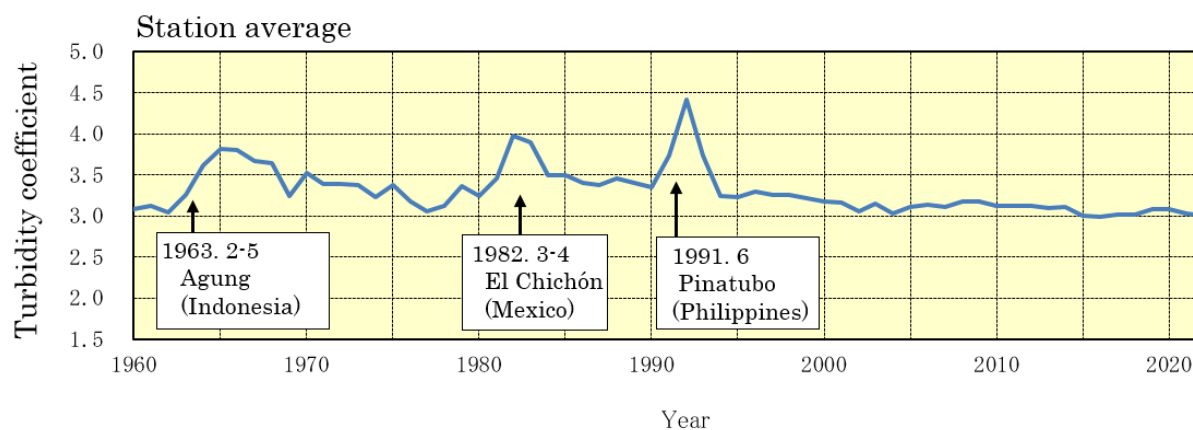


Figure III.4 Annual means in background atmospheric turbidity coefficients (1960 – 2022)

To eliminate the influence of fluctuations in tropospheric constituents such as water vapor, dust and air pollutants, monthly minimum atmospheric turbidity coefficients were used here. Annual means are calculated from monthly minimums averaged over the domestic stations of Abashiri, Tsukuba, Fukuoka, Ishigakijima and Minamitorishima (with observations from Sapporo rather than Abashiri for the period until 2020). Arrows indicate major volcanic eruptions.

As Hunga Tonga-Hunga Ha'apai is a submarine volcano, its 2022 eruption ejected approximately 140 million tons (140 Tg) of water vapor (around 10% of all stratospheric content) into the stratosphere (Millán *et al.*, 2022; Xu *et al.*, 2022). Although the effect of SO₂ reaching the stratosphere alone is considered to be limited (resulting in a temperature drop of up to around 0.1°C over a couple of years) (Zhang *et al.*, 2022; Witze, 2022), this water vapor is thought to have brought about positive radiative forcing (i.e., ground heating), which cancels out negative forcing (i.e., ground cooling) associated with aerosols (Millán *et al.*, 2022; Sellitto *et al.*, 2022). Water vapor also accelerates the conversion of SO₂ to sulfate aerosol with larger particles. This leads to net negative radiative forcing (approximately -0.2 W m^{-2}) despite direct positive radiative forcing caused by water vapor (Zhu *et al.*, 2022). A rapid increase in particle size could also hasten the removal of aerosols from the stratosphere via gravitational settling (Khaykin *et al.*, 2022). These effects are estimated to be smaller than those of cooling caused by the 1991 Mt. Pinatubo eruption (radiative forcing of approximately -2 W m^{-2}) (IPCC, 2021). Although the climatic effects of the 2022 eruption are likely to be limited, the impacts of water vapor on stratospheric chemistry are still unknown. Further observation and research are therefore needed.

IV Largest annual increase in atmospheric methane concentrations since records began

- Based on observation data submitted to the World Data Centre for Greenhouse Gases (WDCGG) of the World Meteorological Organization (WMO), the annual increase in atmospheric methane (CH₄) concentrations from 2020 to 2021 was the largest since records began in 1984. JMA's Ryori and Minamitorishima observation stations also reported their highest-ever annual increases.
- According to WMO (2022), this increase may be attributable to interannual variability along with a long-term increase in emissions. The La Niña phase that began in 2020 may well have contributed to the record increase due to greater methane emissions from tropical wetlands, which are sensitive to shifting temperature and precipitation patterns.

Analysis conducted by the World Data Centre for Greenhouse Gases (WDCGG) of the World Meteorological Organization (WMO), which is operated by the Japan Meteorological Agency (JMA), shows that atmospheric concentrations of the main greenhouse gases (carbon dioxide (CO₂), methane (CH₄) and nitrous oxide (N₂O)) continue to increase, and that globally averaged atmospheric concentrations reached new highs in 2021 (WMO, 2022).

CH₄ is the second most significant greenhouse gas after CO₂, and has a radiative effect around 27.9 times greater than that of CO₂ per unit mass. Its contribution to increased global radiative forcing from the pre-industrial era (around 1750) to 2021 represents around 16% of all long-lived greenhouse gases (WMO, 2022). Around 40% of CH₄ released into the atmosphere is of natural origin (from wetlands, termites and other sources), with the remainder coming from human-related sources (e.g., ruminants, rice paddies, fossil fuels, landfill, biomass combustion) (WMO, 2022). It is primarily removed from the atmosphere via photochemical reaction with reactive and unstable hydroxyl (OH) radicals⁴.

Figure IV.1 shows a time-series representation for global means of atmospheric CH₄ concentrations. Since the mid-1980s, when sufficient data for analysis became available at WDCGG, atmospheric CH₄ concentrations have continued to increase, albeit with seasonal variations and a period of stagnation from 1999 to 2006. IPCC (2021) reported that anthropogenic emissions from the oil and gas sectors declined throughout the 1990s, and that concurrent emission changes from fossil fuels and the agricultural sector may be responsible for the greater concentrations observed since 2007.

⁴ Hydroxyl radicals are highly reactive chemicals generated by the reaction of atomic oxygen, which is derived from UV photolysis of ozone, with airborne water vapor. It is particularly abundant at low latitudes, where UV radiation is strong and water vapor is plentiful.

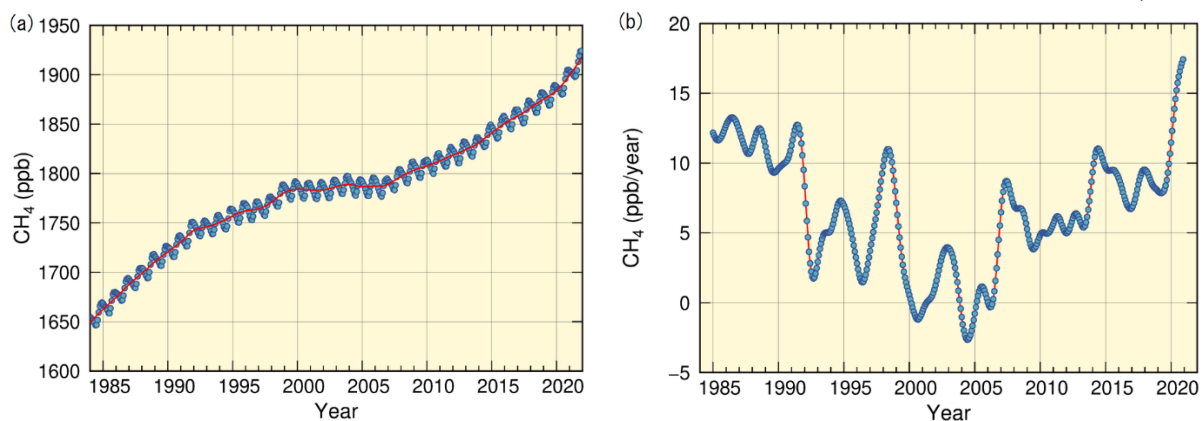


Figure IV.1 Global mean concentrations of atmospheric CH₄ (a) and annual growth rates (b)

In the panel on the left (a) the blue dots are monthly values, and the red line represents the corresponding sequence after removal of seasonal variations. From the latter, the growth rate is derived and shown in the panel on the right (b) (WMO, 2022). Graph content is based on analysis of observation data reported to WDCGG using the method of WMO (2009). Data contributors are listed in WMO (2023).

The global mean surface CH₄ concentration had increased by a factor of around 2.6 from pre-industrial levels (around 729 ppb) to a record high of 1,908 ppb by 2021, and the annual increase in atmospheric concentrations from 2020 to 2021 was the largest (18 ppb) since 1984. Figure IV.2 displays a time-series representation of annual growth rate in the mean concentration of atmospheric CH₄ by latitudinal zone, showing a rapid increase since around 2020. A similar trend is also seen in data from JMA's observation stations at Ryori, Minamitorishima and Yonagunijima. The annual increase from 2020 to 2021 was the largest at Ryori and Minamitorishima (16 and 19 ppb, respectively) and the third largest at Yonagunijima (13 ppb) since records began (see also Figure IV.3).

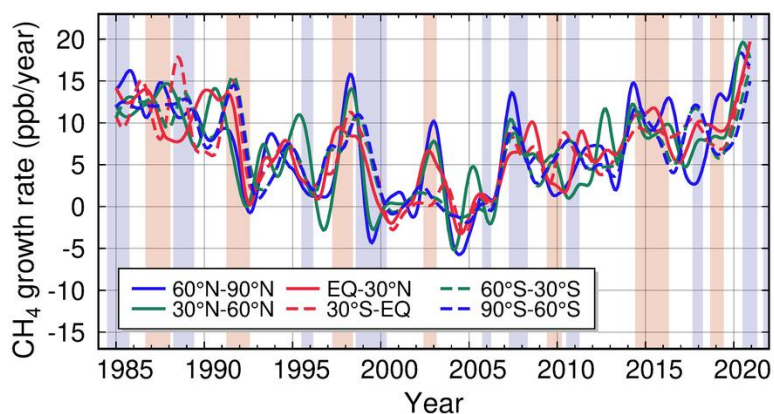


Figure IV.2 Annual growth rates in mean concentrations of atmospheric CH₄ by latitudinal zone

Graph content is based on analysis of observation data reported to WDCGG using the method of WMO (2009). Data contributors are listed in WMO (2023). El Niño and La Niña periods are shaded in light red and blue, respectively.

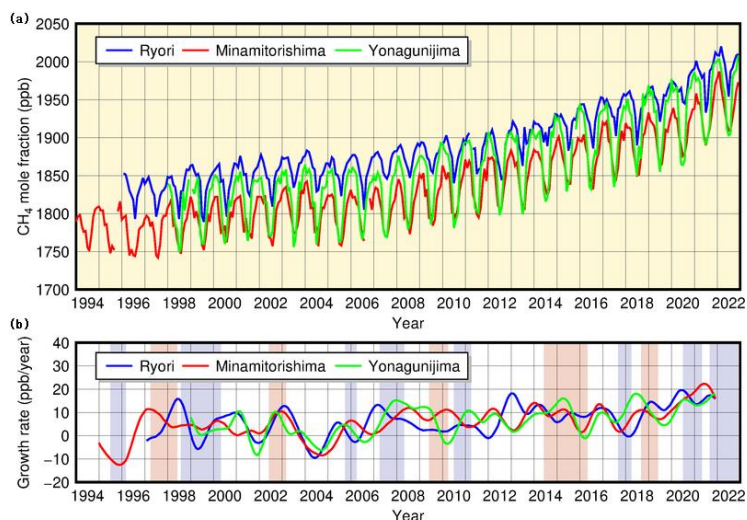


Figure IV.3 Monthly mean concentrations (a) and corresponding growth rates (b) of atmospheric CH₄ observed at Ryori (blue), Minamitorishima (red) and Yonagunijima (green)

The annual growth rate in concentrations is determined by converting monthly increases into annual values after removal of seasonal cycles as per the method described in WMO (2009). El Niño and La Niña periods are shaded in light red and blue, respectively.

The reasons for the record increase in CH₄ concentrations are currently being investigated by the global greenhouse gas science community. According to WMO (2022), the phenomenon may be attributable to interannual variability along with a long-term increase in emissions. The stable carbon isotope signature of CH₄ ($\delta^{13}\text{C}(\text{CH}_4)$) also suggests dominant contributions from microbial CH₄ emissions, and studies based on satellite observations have indicated increased CH₄ emissions from tropical regions (Feng *et al.*, 2022). In combination with analysis of inverse modelling pointing to a tropical origin, this suggests that CH₄ emissions from tropical wetlands may have increased over the past few years. It is also known that microbial CH₄ production in tropical wetlands is sensitive to shifting temperatures and precipitation patterns, and is easily influenced by El Niño-Southern Oscillation (ENSO). It has been suggested that the La Niña phase originating in 2020 may well have contributed to the record increase (Figure IV.2). Meanwhile, significant uncertainties remain in relation to CH₄ emissions from wetlands and biomass combustion driven by ENSO and variations in OH radicals, which contribute to CH₄ destruction (IPCC, 2021).

As CH₄ has a shorter atmospheric lifetime and a greater greenhouse effect per molecule than CO₂, reduction of related emissions is expected to have a rapid effect on global warming mitigation in combination with long-term CO₂ emission reductions. The Global Methane Pledge (an international CH₄ emission reduction initiative launched at the 26th session of the Conference of the Parties (COP26) to the United Nations Framework Convention on Climate Change (UNFCCC) in November 2021) aims to reduce global CH₄ emissions by 30% from 2020 levels by 2030, with over 100 countries and regions including Japan having expressed intent to participate in the initiative. To promote such effective measures against global warming, JMA contributes to the monitoring of greenhouse gas concentrations through international activities such as WDCGG work, greenhouse gas observation and related analysis.

Chapter 1 Climate in 2022

1.1 Global climate summary

- Extremely high temperatures were observed in the mid-latitudes and elsewhere. Record-breaking monthly, seasonal and annual mean temperatures were reported by various countries, and a new national record-high was set in the UK.
- Disaster conditions resulting in extensive fatalities were caused by tropical storms in the Philippines in April and October, heavy rains in and around Pakistan from July to August, and heavy rains in the southeastern part of South Africa in April.

Major extreme climate events⁵ and weather-related disasters occurred in 2022 are shown in Figure 1.1-1 and Table 1.1-1.

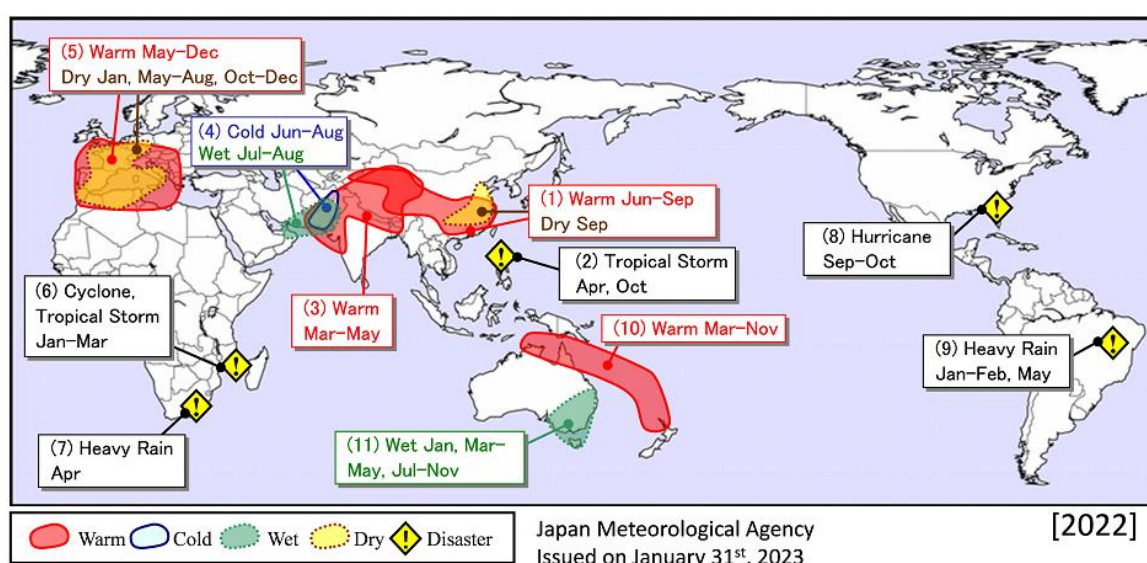


Figure 1.1-1 Major extreme events and weather-related disasters observed in 2022⁶

“Warm,” “Cold,” “Wet” and “Dry” indicate extreme climate events with particularly significant effects. JMA defines extreme events as phenomena likely to occur with a 30-year periodicity. Disaster effects are evaluated from EM-DAT information, United Nations reports and government data.

EM-DAT: The Emergency Events Database - Université Catholique de Louvain (UCL) - CRED, D. Guha-Sapir - www.emdat.be, Brussels, Belgium.

Extremely high temperatures ((1), (3), (5), and (10) in Figure 1.1-1) were observed mainly in the mid-latitudes.

From eastern to northwestern China, extremely high temperatures were observed from June to September as well as extremely low precipitations in September ((1) in Figure 1.1-1). Record-high monthly mean temperatures were reported in China and Hong Kong (sources: China Meteorological Administration and Hong Kong Observatory). From western China to Pakistan, extremely high temperatures were observed from March to May ((3) in Figure 1.1-1), and the monthly mean temperature in China in March was the highest on record since 1961 (source: China Meteorological Administration).

⁵ Extreme climate events are defined by anomalies or ratios to climatological normals. Normals represent mean climate conditions at given sites, and are currently based on a 30-year mean covering the period from 1991-2020.

⁶ Information on major extreme climatic events and weather-related disasters since 2008 is provided on JMA’s website at <https://www.data.jma.go.jp/tcc/tcc/products/climate/annual/index.html>

In and around Pakistan, extremely low temperatures and extremely high precipitations were observed from June to August and from July to August, respectively ((4) in Figure 1.1-1).

From central Europe to the northwestern part of Northern Africa, extremely high temperatures were observed from May to December as well as extremely low precipitations in January, May to August, and October to December ((5) in Figure 1.1-1). Record-high monthly, seasonal, and annual mean temperatures were reported in various countries in Europe (sources: UK Met Office; Meteo France; Deutscher Wetterdienst; The State Meteorological Agency, Spain; and The Portuguese Institute for Sea and Atmosphere). In the eastern UK 40.3 degrees Celsius was recorded at Coningsby on 19 July, which is a new national maximum temperature record in the UK (source: UK Met Office).

From northern Australia to northern New Zealand, extremely high temperatures were observed from March to November ((10) in Figure 1.1-1), and record-high monthly, seasonal, and annual mean temperatures were reported in New Zealand (source: National Institute of Water and Atmospheric Research, New Zealand).

In southeastern Australia, extremely high precipitations were observed in January, March to May, and July to November ((11) in Figure 1.1-1).

Climate extremes including heavy rains ((4), (7), and (9) in Figure 1.1-1) and tropical cyclones ((2), (6), and (8) in Figure 1.1-1) caused immense damage worldwide.

Tropical Storms MEGI in April and NALGAE in October ((2) in Figure 1.1-1) caused totally more than 440 fatalities in the Philippines (source: government of the Philippines; EM-DAT). Heavy rains from May to September ((4) in Figure 1.1-1) caused more than 4,510 fatalities in and around South Asia, including more than 1,730 fatalities in Pakistan (source: EM-DAT). Tropical Storm ANA in January, Cyclones BATSIRAI, EMNATI, and Tropical Storm DUMAKO in February, and Cyclone GOMBE in March ((6) in Figure 1.1-1) caused totally more than 390 fatalities from Madagascar to Malawi (source: EM-DAT). Heavy rains in April ((7) in Figure 1.1-1) caused more than 540 fatalities in the southeastern part of South Africa (source: EM-DAT). Hurricane IAN from September to October ((8) in Figure 1.1-1) caused more than 150 fatalities and economic losses estimated at US\$112.9 billion from the southeastern to eastern USA (source: National Oceanic and Atmospheric Administration, the USA). Heavy rains from January to February and May ((9) in Figure 1.1-1) caused totally more than 430 fatalities from northeastern to southeastern Brazil (source: EM-DAT).

Annual mean temperatures were above normal mainly in the mid-latitudes, and very high from East Asia to Central Asia, from northwestern Europe to the northern part of Northern Africa, and from northern Australia to New Zealand (Figure 1.1-2).

Annual precipitation amounts were above normal from the Nansei Islands of Japan to Southeast Asia, from northwestern India to southern Pakistan, and from southeastern Australia to New Zealand, and below normal from southern Europe to the northwestern part of Northern Africa, and in the western part of South America (Figure 1.1-3).

Table 1.1-1 Major extreme climatic events and weather-related disasters worldwide in 2022

No.	Type	Period	Area
(1)	Warm, Dry	June-September (for Warm), September (for Dry)	From eastern to northwestern China
(2)	Tropical Storm	April, October	The Philippines
(3)	Warm	March-May	From western China to Pakistan
(4)	Cold, Wet	June-August (for Cold), July-August (for Wet)	In and around Pakistan
(5)	Warm, Dry	May-December (for Warm), January, May-August, October-December (for Dry)	From central Europe to the northwestern part of Northern Africa
(6)	Cyclone, Tropical Storm	January-March	From Madagascar to Malawi
(7)	Heavy Rain	April	The southeastern part of South Africa
(8)	Hurricane	September-October	From the southeastern to eastern USA
(9)	Heavy Rain	January-February, May	From northeastern to southeastern Brazil
(10)	Warm	March-November	From northern Australia to northern New Zealand
(11)	Wet	January, March-May, July- November	Southeastern Australia

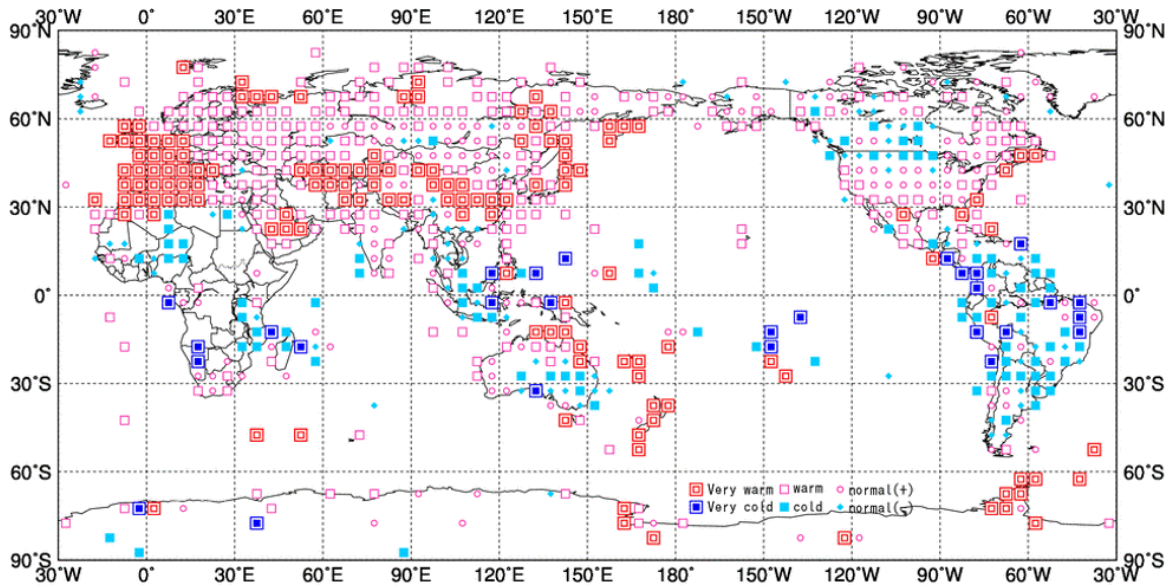


Figure 1.1-2 Normalized annual mean temperature anomalies for 2022⁷

Categories are defined by the annual mean temperature anomaly against the normal divided by its standard deviation and averaged in $5^\circ \times 5^\circ$ grid boxes. Red/blue marks indicate values above/below the normal calculated for the period from 1991 to 2020. The thresholds of each category are -1.28 , -0.44 , 0 , $+0.44$ and $+1.28$ ⁸. Land areas without graphics represent regions for which the observation data sample is insufficient or normal data are unavailable.

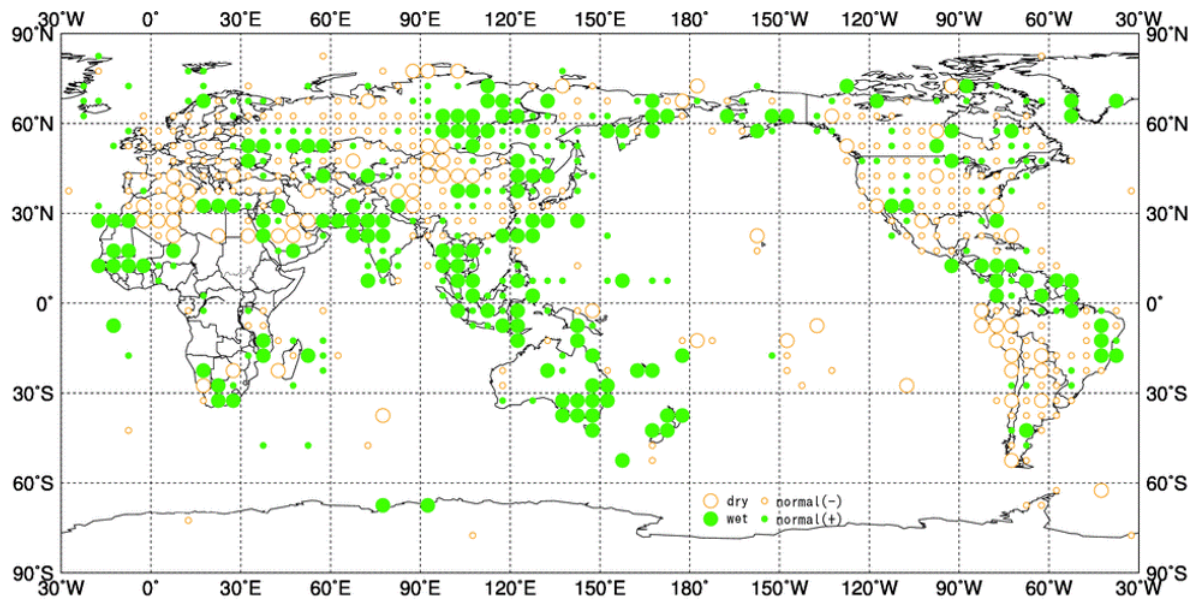


Figure 1.1-3 Annual total precipitation amount ratios for 2022³

Categories are defined by the annual precipitation ratio to the normal averaged in $5^\circ \times 5^\circ$ grid boxes. Green/yellow marks indicate values above/below the thresholds. The thresholds of each category are 70, 100 and 120% of the normal calculated for the period from 1991 to 2020. Land areas without graphics represent regions for which the observation data sample is insufficient or normal data are unavailable.

⁷ Normalized annual mean temperature anomalies and annual total precipitation amount ratios since 2008 are provided on JMA's website at <https://www.data.jma.go.jp/tcc/tcc/products/climate/annual/index.html>

⁸ In normal distribution, values of 1.28 and 0.44 correspond to occurrence probabilities of less than 10 and 33.3%, respectively.

1.2 Climate in Japan⁹

- Temperatures were above normal from spring to autumn except for a few short cooler-than-normal spells, resulting in annual temperatures above normal nationwide and significantly above normal in northern Japan.
- In winter (Dec. 2021 – Feb. 2022), an active northwest monsoon brought cold conditions in eastern and western Japan and heavy snowfall in some places on the Sea of Japan side of these regions.
- In August, anomalous precipitation amounts were observed in northern Japan and on the Sea of Japan side of eastern Japan. Due to the prolonged rain, the official end dates of the Baiu rainy season were undetermined for some areas.

1.2.1 Annual characteristics

The annual climate anomaly/ratio for Japan in 2021 is shown in Figure 1.2-1.

- Annual mean temperatures were above normal nationwide and significantly above normal in northern Japan.
- Annual precipitation amounts were significantly above normal in Okinawa/Amami and above normal in northern Japan. Values were significantly below normal on the Sea of Japan side of western Japan and below normal on the Pacific side of western Japan.
- Annual sunshine durations were significantly above normal on the Sea of Japan side of northern and western Japan, and above normal on the Pacific side of these regions and in eastern Japan. Values were significantly below normal in Okinawa/Amami.

⁹ The term significantly above normal is used for cases in which observed mean temperatures or precipitation amounts exceed the 90th percentile for the base period (1991 – 2020), and significantly below normal is used when the corresponding figures fall below the 10th percentile.

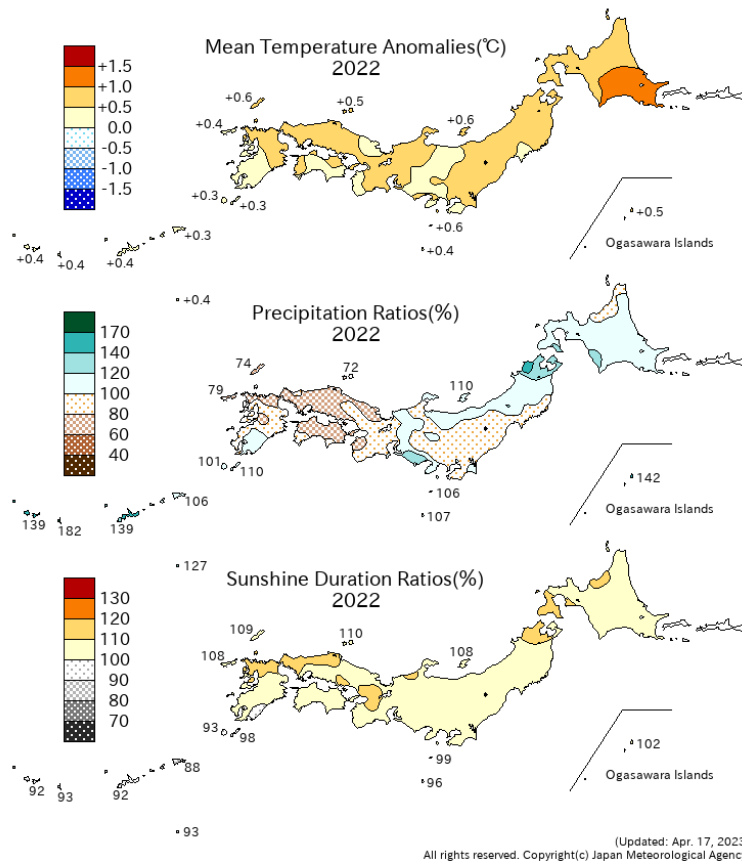
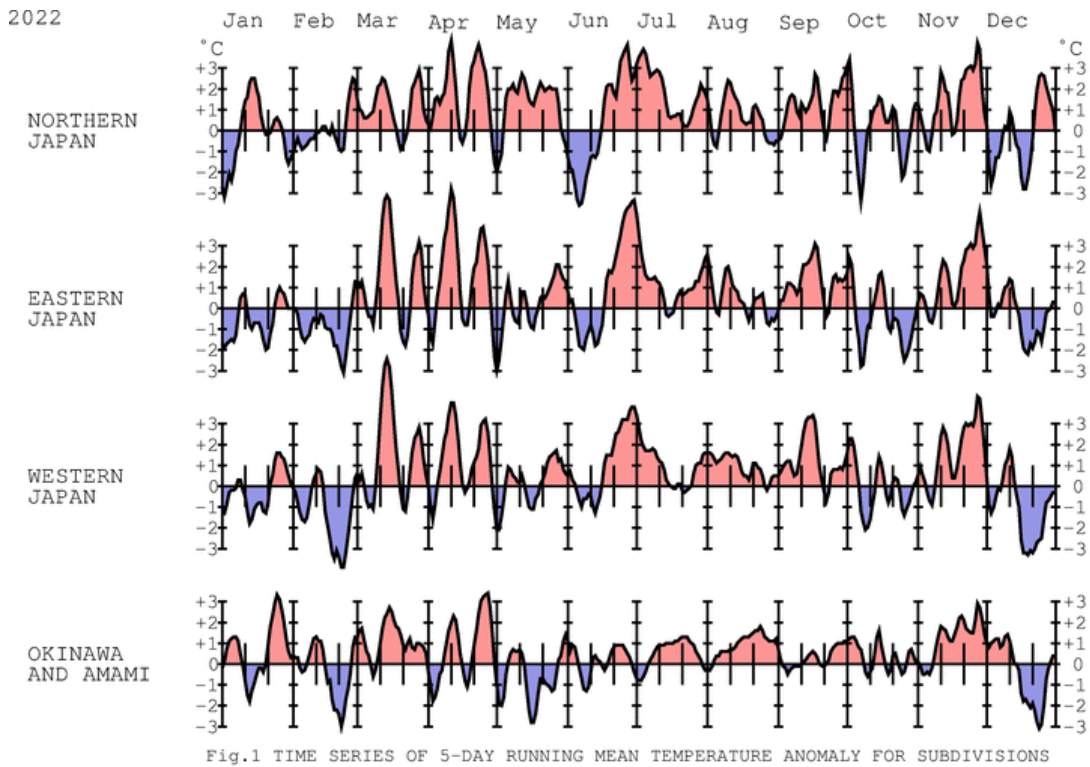


Figure 1.2-1 Annual climate anomaly/ratio for Japan in 2022

The base period for the normal is 1991 – 2020.



Last Data:2023/ 1/ 2

Figure 1.2-2 Five-day running mean temperature anomaly for divisions (January – December 2022)

The base period for the normal is 1991 – 2020.

1.2.2 Seasonal characteristics

Five-day running mean temperature anomalies for different divisions (January – December 2022) are shown in Figure 1.2-2, and seasonal anomalies/ratios for Japan in 2022 are shown in Figure 1.2-3. Numbers of observatories reporting record monthly and annual mean temperatures, precipitation amounts and sunshine durations (2022) are shown in Table 1.2-1.

(1) Winter (December 2021 – February 2022)

- Seasonal mean temperatures were below normal in eastern and western Japan.
- Seasonal precipitation amounts were significantly above normal on the Sea of Japan side of northern Japan and above normal in Okinawa/Amami. Values were significantly below normal in western Japan.
- Seasonal sunshine durations were above normal in northern and western Japan and on the Pacific side of eastern Japan, and below normal in Okinawa/Amami.

An intense winter monsoon brought below-normal seasonal mean temperatures in eastern and western Japan, and heavy snowfall was observed in some places on the Sea of Japan side of these regions. Seasonal precipitation amounts were significantly above normal on the Sea of Japan side of northern Japan due to the active northwest winter monsoon and extratropical cyclones. Western Japan was less affected by extratropical cyclones throughout the season, resulting in significantly below-normal seasonal precipitation amounts. In Okinawa/Amami, which was repeatedly affected by low-pressure systems and fronts in January and February, seasonal precipitation amounts were above normal and sunshine durations were below normal

(2) Spring (March – May 2022)

- Seasonal mean temperatures were significantly above normal in northern and western Japan and above normal in eastern Japan and Okinawa/Amami.
- Seasonal precipitation amounts were significantly above normal in Okinawa/Amami and above normal on the Pacific side of eastern Japan. Values were below normal in northern Japan and on the Sea of Japan side of eastern and western Japan.
- Seasonal sunshine durations were significantly above normal in northern Japan and on the Sea of Japan side of eastern Japan, and above normal on the Sea of Japan side of western Japan. Values were below normal in Okinawa/Amami.

Seasonal mean temperatures were above normal nationwide, generally due to warm-air advection. Seasonal sunshine durations were significantly above normal in northern Japan and on the Sea of Japan side of eastern Japan, which were repeatedly influenced by anticyclones. Meanwhile, Okinawa/Amami was affected by moist-air inflow with an active Baiu front in May, resulting in significantly above-normal seasonal precipitation amounts.

(3) Summer (June – August 2022)

- Seasonal mean temperatures were significantly above normal in eastern and western Japan and Okinawa/Amami, and above normal in northern Japan.
- Seasonal precipitation amounts were significantly above normal in northern Japan and above normal in eastern Japan. Values were below normal in western Japan.
- Seasonal sunshine durations were above normal on the Pacific side of western Japan and in Okinawa/Amami, and below normal on the Pacific side of northern Japan.

Seasonal mean temperatures were significantly above normal in eastern/western Japan and Okinawa/Amami due to anomalous warm-air masses throughout summer. The regional average of seasonal mean temperature anomalies in western Japan tied with 2013 and 2018 as the highest on record since 1946. Seasonal precipitation amounts were significantly above normal in northern Japan, which was repeatedly affected by low-pressure systems and fronts. Due to prolonged rain in August, the official end dates of the Baiu rainy season were undetermined for some areas in northern Japan and on the Sea of Japan side of eastern Japan.

(4) Autumn (September – November 2022)

- Seasonal mean temperatures were significantly above normal nationwide.
- Seasonal precipitation amounts were significantly above normal in Okinawa/Amami. Values were significantly below normal on the Pacific side of northern Japan and below normal on the Sea of Japan side of northern and eastern Japan.
- Seasonal sunshine durations were significantly above normal on the Sea of Japan side of northern, eastern and western Japan, and above normal on the Pacific side of these regions. Values were significantly below normal in Okinawa/Amami.

Seasonal mean temperatures were significantly above normal nationwide due to warm-air masses in September and weaker-than-normal cold-air inflow in November. The delayed onset of the northwestern monsoon and the influence of anticyclones resulted in significantly above-normal seasonal sunshine durations on the Sea of Japan side of northern, eastern and western Japan. In contrast, Okinawa/Amami was repeatedly affected by tropical cyclones and moist air inflow, resulting in significantly above-normal seasonal precipitation amounts and significantly below-normal seasonal sunshine durations.

(5) Early Winter (December 2022)

An active northwestern winter monsoon led to significantly above-normal monthly precipitation amounts on the Sea of Japan side of northern and eastern Japan. This brought significantly above-normal monthly snowfall amounts on the Sea of Japan side of eastern Japan, while monthly mean temperatures were below normal in eastern and western Japan due to strong cold-air inflow. Monthly precipitation amounts were significantly above normal in Okinawa/Amami, which was affected by extratropical cyclones, fronts and cold-air inflow.

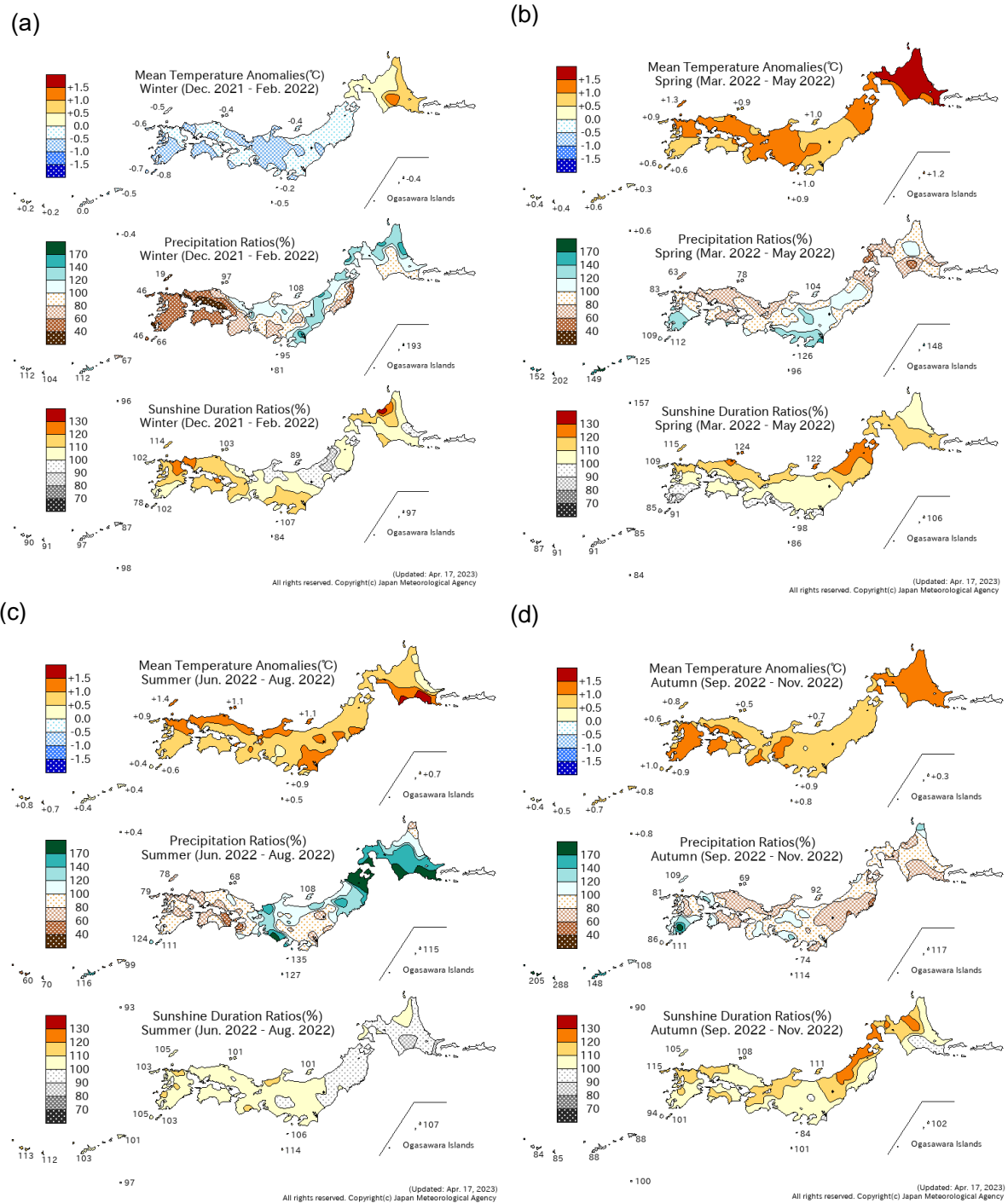


Table 1.2-1 Number of observatories reporting record(include tie record) monthly and annual mean temperatures, precipitation amounts and sunshine durations (2022)

From 153 surface meteorological stations across Japan.

	Temperature		Precipitation amount		Sunshine duration	
	Highest	Lowest	Heaviest	Lightest	Longest	Shortest
January				1	2	
February				9		
March						1
April	6		3	7	3	
May			6	4		3
June	13		2			
July	8		1			
August	6		6	1	1	
September	1				1	
October						
November	38		2		14	
December			1			1
year	72	0	21	22	21	5

1.3 Atmospheric circulation and oceanographic conditions¹⁰

- The La Niña event that began in boreal autumn 2021 persisted during 2022, with ongoing influences.
- The negative phase of an Indian Ocean Dipole (IOD) event was observed from summer to autumn 2022. Convective activity over the Asian summer monsoon region also exhibited significant intra-seasonal variability.

Monitoring of atmospheric and oceanographic conditions (e.g., upper air flow, tropical convective activity, sea surface temperatures (SSTs) and the Asian monsoon) is key to understanding the causes of extreme weather events¹¹. This section briefly outlines the characteristics of atmospheric circulation and oceanographic conditions seen in 2022.

1.3.1 Characteristics of individual seasons¹²

(1) Winter (December 2021 – February 2022)

Negative SST anomalies were observed east of 170°E, particularly in the eastern part of the equatorial Pacific (Figure 1.3-1 (a)) in association with the persistent La Niña conditions observed from boreal autumn 2021 onward.

Tropical convection was enhanced from the Philippines to the seas north of New Guinea Island, and was suppressed from the area near the date line to the eastern part of the equatorial Pacific (Figure 1.3-1 (b)). In the upper troposphere, cyclonic circulation anomalies straddling the equator were seen over the central to eastern tropical Pacific in association with the suppressed convection, suggesting an influence from La Niña (Figures 1.3-1 (c) and (d)).

In the 500-hPa height field, the polar vortex in the Northern Hemisphere split, with positive anomalies over Eastern Siberia. One part of the polar vortex moved southward toward north of Japan (Figure 1.3-1 (e)). Wavy patterns in height anomalies were seen from the central part of the North Pacific to Canada and from Europe to southern Eurasia. The subtropical jet stream significantly meandered from northern Africa to Eurasia, and shifted southward to the east of Japan (Figure 1.3-1 (c)). In the sea level pressure field, the Aleutian Low was stronger than normal over its southwestern part (Figure 1.3-1 (f)). Temperatures at 850 hPa were above normal over a wide area of Siberia and from the Okhotsk Sea to the seas south of Alaska, and were below normal over East Asia (Figure 1.3-1 (g)). The southward-shifted subtropical jet stream to the east of Japan was likely influenced by its northward meandering to the west of Japan due to La Niña-related enhanced convection from the Philippines to the seas north of New Guinea Island.

¹⁰ See the Glossary for terms relating to sea surface temperature variations and monsoon.

¹¹ The main charts used for monitoring of atmospheric circulation and oceanographic conditions are: sea surface temperature (SST) maps representing SST distribution for monitoring of oceanographic variability elements such as El Niño/La Niña phenomena; outgoing longwave radiation (OLR) maps representing the strength of longwave radiation from the earth's surface under clear sky conditions into space or from the top of clouds under cloudy conditions into space for monitoring of convective activity; 850-hPa stream function maps representing air flow in the lower troposphere for monitoring of atmospheric circulation variability elements such as the Pacific High and the monsoon trough associated with the Asian summer monsoon; 500-hPa height maps representing air flow at a height of approximately 5,500 meters for monitoring of atmospheric circulation variability elements such as westerly jet streams and the Arctic Oscillation; sea level pressure maps representing air flow and pressure systems on the earth's surface for monitoring of the Pacific High, the Siberian High, the Arctic Oscillation and other phenomena; 850-hPa temperature maps representing air temperature at a height of approximately 1,500 meters; and temperature calculated from thickness in the troposphere for monitoring of mean temperature of the troposphere.

¹² JMA publishes Monthly Highlights on the Climate System including information on the characteristics of climatic anomalies and extreme events around the world, atmospheric circulation and oceanographic conditions. It can be found at <https://www.data.jma.go.jp/tcc/tcc/products/clisys/highlights/index.html>.

(2) Spring (March – May 2022)

In the equatorial Pacific, positive SST anomalies were observed west of 150°E, and remarkably negative anomalies were observed in central to eastern parts in association with the persistent La Niña event (Figure 1.3-2 (a)).

Tropical convection was enhanced from southwestern India to the area near the Philippines, and was suppressed over western to central parts of the equatorial Pacific (Figure 1.3-2 (b)). In the upper troposphere, anti-cyclonic circulation anomalies were seen from the Middle East to southern East Asia, and cyclonic circulation anomalies straddling the equator were seen near the date line in the tropical Pacific (Figure 1.3-2 (c)). In the lower troposphere, anti-cyclonic circulation anomalies straddling the equator were seen near the date line in the tropical Pacific, and cyclonic circulation anomalies straddling the equator were seen over the Indian Ocean (Figure 1.3-2 (d)). These anomalies correspond to the tropical ones described above, suggesting an influence from the persistent La Niña event.

In the 500-hPa height field, a wavy pattern of anomalies was seen from the North Atlantic to central Eurasia, with positive anomalies over western to central Europe and to the north of India. Positive anomalies were also seen over the eastern part of eastern Siberia and from Japan to the east (Figure 1.3-2 (e)). The subtropical jet stream shifted northward from Eurasia to the seas east of Japan (Figure 1.3-2 (c)), possibly due to enhanced convection from southwestern India to the area near the Philippines. In the sea level pressure field, positive anomalies were seen over Europe and from the area near Japan to the seas west of North America, and negative anomalies were seen over a wide area from central to eastern Eurasia (Figure 1.3-2 (f)). Temperatures at 850 hPa were above normal in the latitude band of 30°N from central Eurasia to the North Atlantic, and were below normal near eastern Europe (Figure 1.3-2 (g)).

In association with the above normal temperatures in the latitude band of 30°N over central Eurasia, the monthly average temperature in China was the highest on record for March since 1961 (China Meteorological Administration, Section 1.1).

(3) Summer (June – August 2022)

In the equatorial Pacific, positive SST anomalies were observed west of 150°E, and remarkably negative anomalies were observed in the central part in association with the persistent La Niña event. In the tropical Indian Ocean, positive and negative anomalies were seen in eastern and western parts, respectively, indicating the negative phase of the Indian Ocean Dipole (IOD) event (Figure 1.3-3 (a)).

Tropical convection was enhanced from the northern Arabian Sea to the area near Pakistan and from the southeastern part of the tropical Indian Ocean to southern Indonesia, and was suppressed in the western equatorial Pacific (Figure 1.3-3 (b)). In the upper troposphere, anti-cyclonic circulation anomalies were seen over northern China accompanied by a wavy pattern of anomalies from the region toward the northeast. Cyclonic circulation anomalies straddling the equator were seen over the western-to-central tropical Pacific (Figure 1.3-3 (c)). In the lower troposphere of the tropical region, anti-cyclonic circulation anomalies straddling the equator were seen over the western-to-central Pacific (Figure 1.3-3 (d)). These anomalies over the tropical Pacific corresponded to suppressed convection over the western equatorial Pacific, suggesting an influence from the persistent La Niña event.

In the 500-hPa height field, a wavy pattern of anomalies was seen over northern Eurasia, with positive values over western Russia and the southern part of Eastern Siberia and negatives over central Siberia. Positive height anomalies were also seen over Europe (Figure 1.3-3 (e)). The subtropical jet stream over Eurasia shifted northward from its normal position (Figure 1.3-3 (c)). In the sea level pressure field, positive anomalies were

seen from the northern part of the North Atlantic to western Russia, and negative anomalies were observed near central Siberia. The Pacific High extended farther west of its normal position to the seas south of Japan (Figure 1.3-3 (f)). Temperatures at 850 hPa were above normal over Europe, western Russia, the area near the western part of eastern Siberia, and over a wide area of East Asia, and were below normal near southern central Siberia (Figure 1.3-3 (g)).

Record-breaking hot conditions were observed over eastern and western Japan from late June to early July in association with the intensified Pacific High extension toward Japan (News I). In association with above-normal temperatures over a wide area of East Asia, monthly average temperatures in China and Hong Kong were the highest on record for summer (China Meteorological Administration and Hong Kong Observatory; Section 1.1)

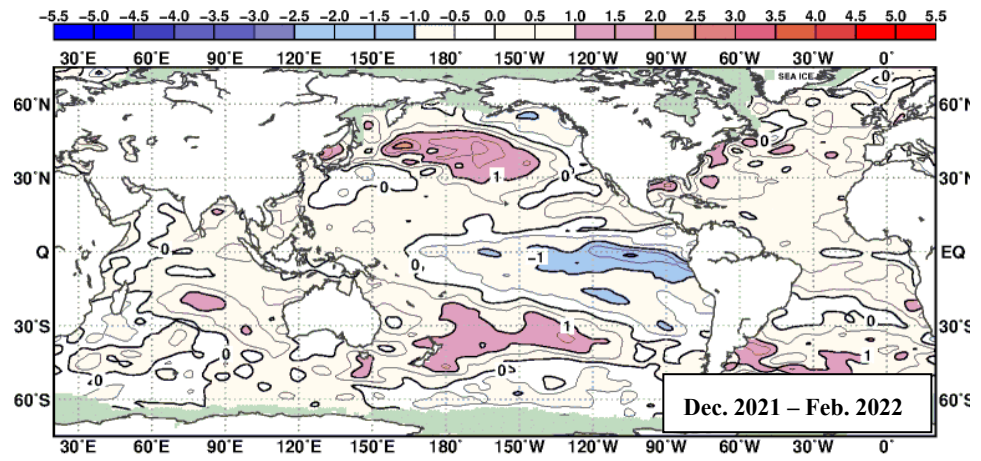
(4) Autumn (September – November 2022)

In the equatorial Pacific, remarkably positive SST anomalies were observed west of 150°E, and remarkably negative anomalies were observed in central and eastern parts in association with the persistent La Niña event. In the tropical Indian Ocean, positive anomalies were seen in the eastern part, corresponding to the persistent negative phase of the Indian Ocean Dipole (IOD) event (Figure 1.3-4 (a)).

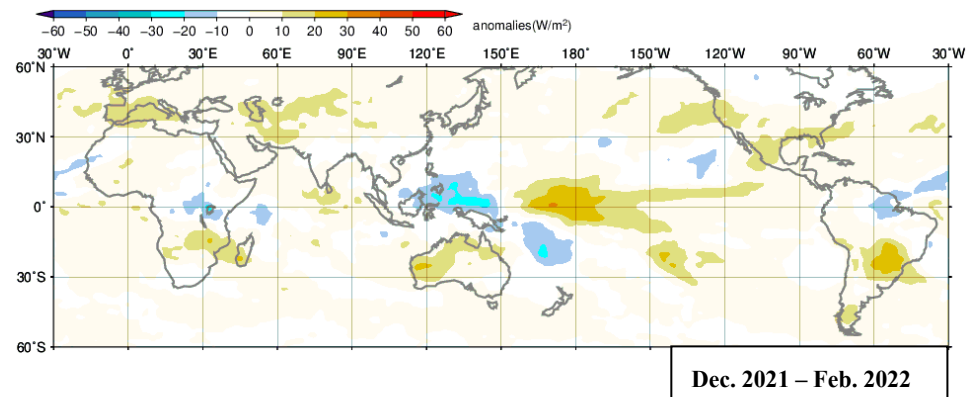
Tropical convection was enhanced in the area near Indonesia and suppressed over the western-to-central equatorial Indian Ocean and the western-to-central equatorial Pacific (Figure 1.3-4 (b)). In the upper troposphere, anti-cyclonic circulation anomalies were seen from the southeastern tropical Indian Ocean to northern Australia, and cyclonic circulation anomalies straddling the equator were seen over the western tropical Indian Ocean and the central tropical Pacific (Figure 1.3-4 (c)). In the lower troposphere, anti-cyclonic circulation anomalies straddling the equator were seen over the western-to-central tropical Pacific, and cyclonic circulation anomalies straddling the equator were seen from the eastern tropical Indian Ocean to the area near Indonesia (Figure 1.3-4 (d)). Circulation anomalies from the Indian Ocean to the tropical Pacific corresponded to enhanced convection near Indonesia and suppressed convection over the western equatorial Pacific, suggesting influences from the persistent negative phase of the IOD and the La Niña event.

In the 500-hPa height field, positive anomalies were seen over the northern part of the North Pacific, to the north of Europe, and over a wide area of the Northern Hemisphere mid-latitudes. Negative anomalies were seen to the west of the United Kingdom, over central-to-eastern Siberia, and to the east of Japan (Figure 1.3-4 (e)). The westerly jet stream was stronger than normal over the North Atlantic, and shifted northward over the area from eastern Eurasia to the seas east of Japan (Figure 1.3-4 (c)). In the sea level pressure field, positive anomalies were seen over the northern part of the North Pacific and northern Europe, and negative anomalies were seen to the west of the United Kingdom and over central to eastern Siberia (Figure 1.3-4 (f)). Temperatures at 850-hPa were above normal to the east of Greenland and over a wide area of the Northern Hemisphere mid-latitudes (Figure 1.3-4 (g)).

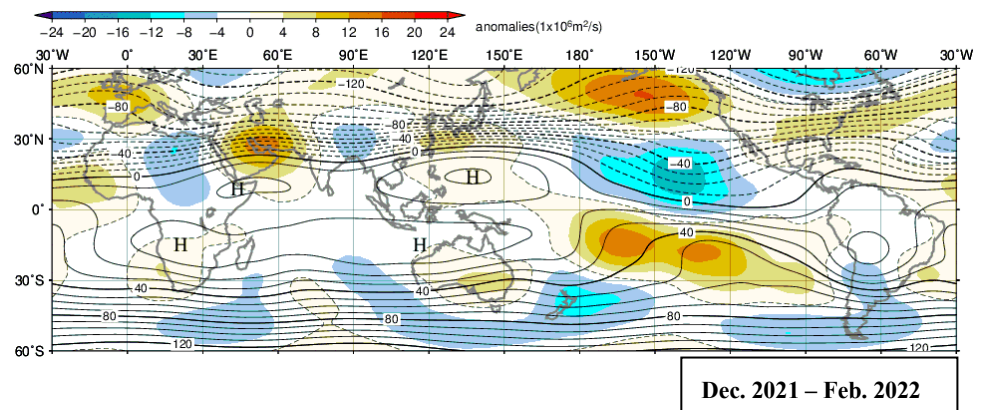
(a) SST anomaly



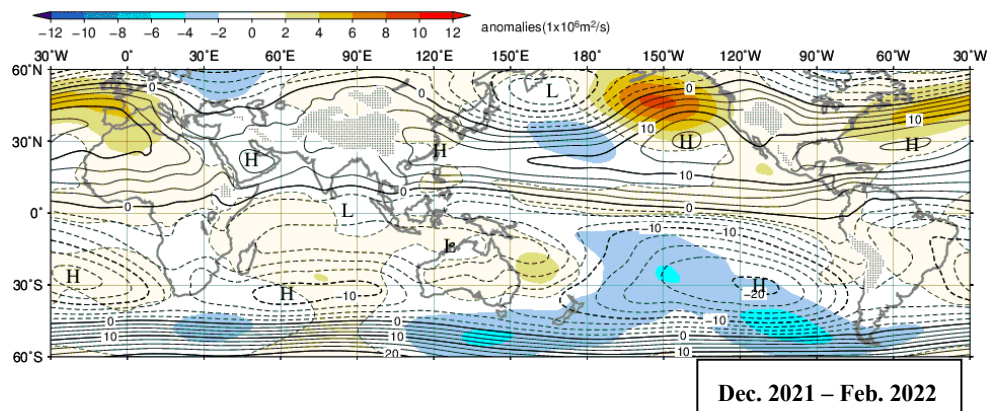
(b) OLR anomaly

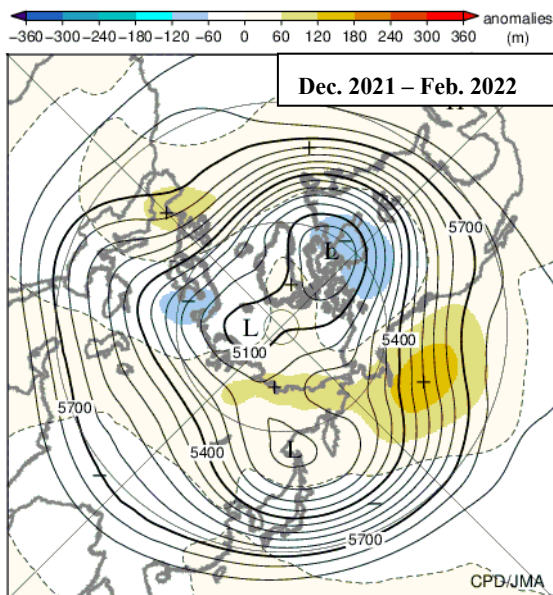


(c) 200-hPa stream function and anomaly

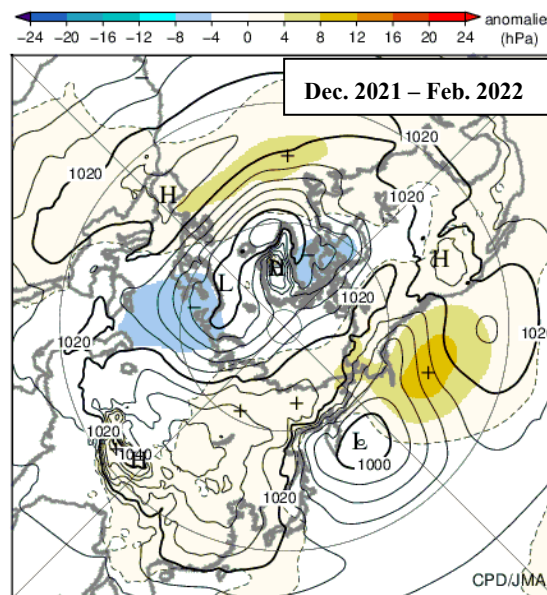


(d) 850-hPa stream function and anomaly

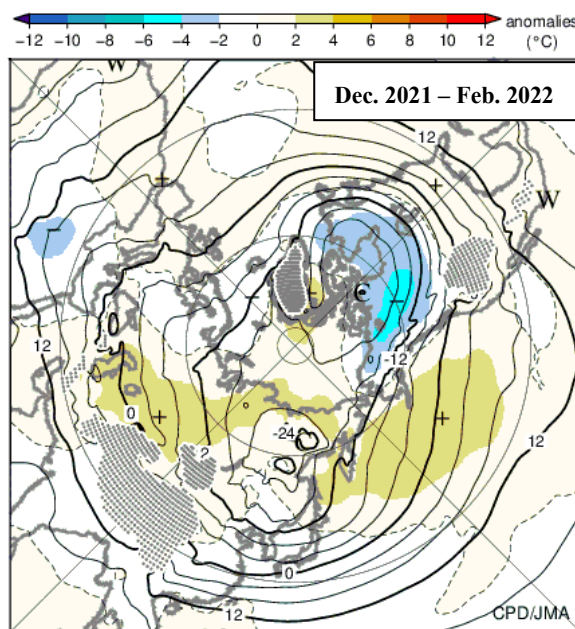




(e) 500-hPa height and anomaly



(f) SLP and anomaly

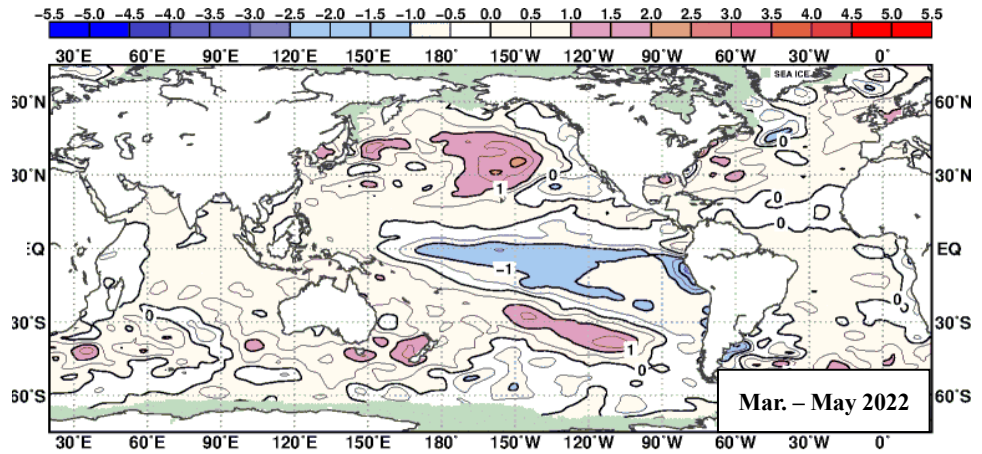


(g) 850-hPa temperature and anomaly

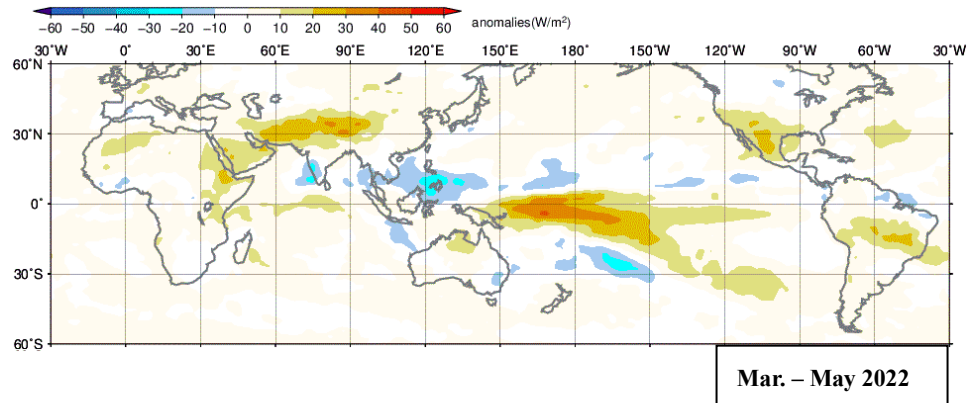
Figure 1.3-1 Three-month mean (a) sea surface temperature (SST) anomaly, (b) outgoing longwave radiation (OLR) anomaly, (c) 200-hPa stream function and anomaly, (d) 850-hPa stream function and anomaly, (e) 500-hPa height and anomaly in the Northern Hemisphere (NH), (f) sea level pressure (SLP) and anomaly in NH, and (g) 850-hPa temperature and anomaly in NH (December 2021 – February 2022)

The base period for the normal is 1991 – 2020. (a) The contour interval is 0.5°C. Sea ice coverage areas are shaded in gray. (b) Negative (cold color) and positive (warm color) OLR anomalies show enhanced and suppressed convection, respectively, compared to the normal. Original data provided by NOAA. The contour intervals are (c) $10 \times 10^6 \text{ m}^2/\text{s}$ and (d) $2.5 \times 10^6 \text{ m}^2/\text{s}$. “H” and “L” denote high- and low-pressure systems, respectively. (e) Contours show 500-hPa height at intervals of 60 m, and shading indicates height anomalies. “H” and “L” denote high- and low-pressure systems, respectively. (f) Contours show sea level pressure at intervals of 4 hPa, and shading indicates sea level pressure anomalies. “H” and “L” denote high- and low-pressure systems, respectively. (g) Contours show temperature at intervals of 4 degree C, and shading indicates temperature anomalies. “W” and “C” denote warm and cold conditions, respectively.

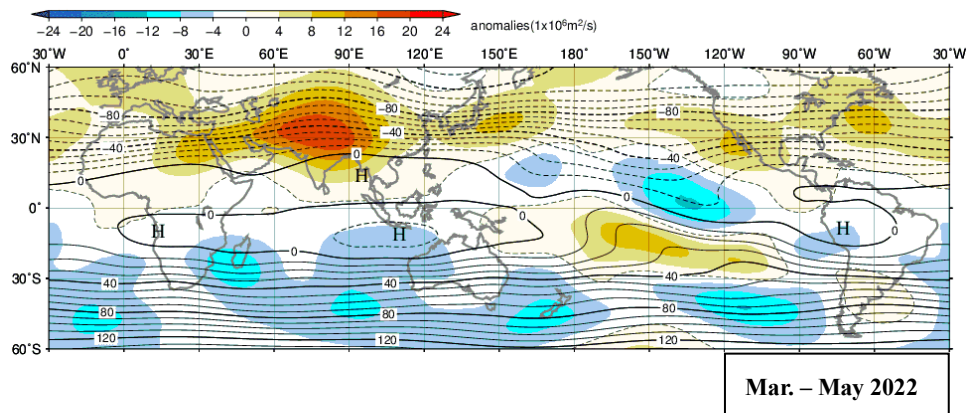
(a) SST anomaly



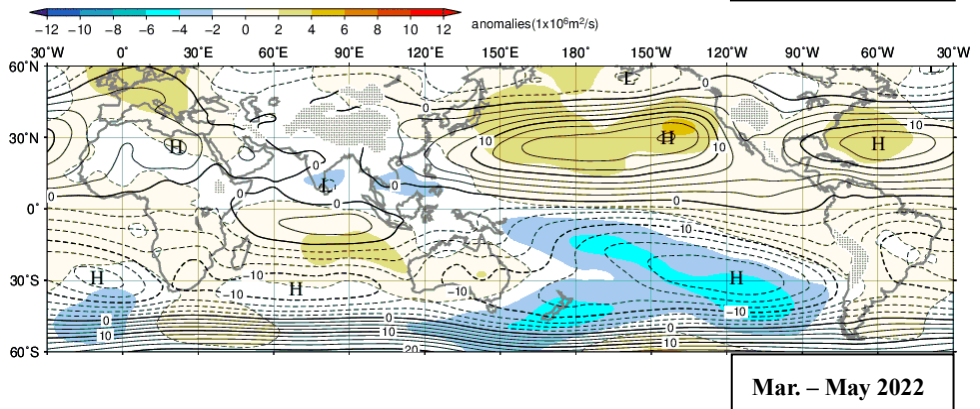
(b) OLR anomaly

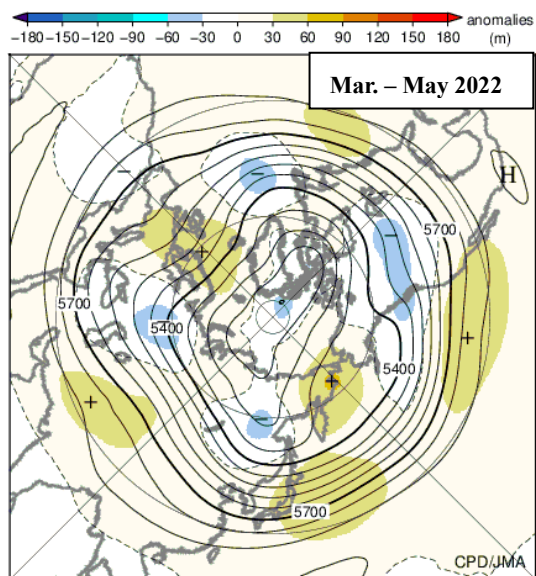


(c) 200-hPa stream function and anomaly

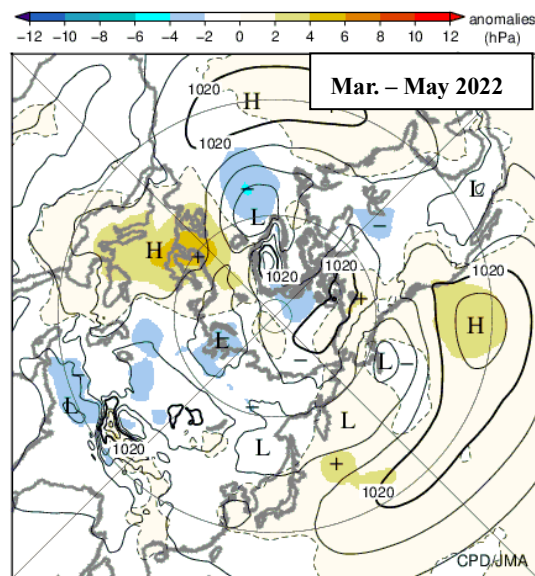


(d) 850-hPa stream function and anomaly

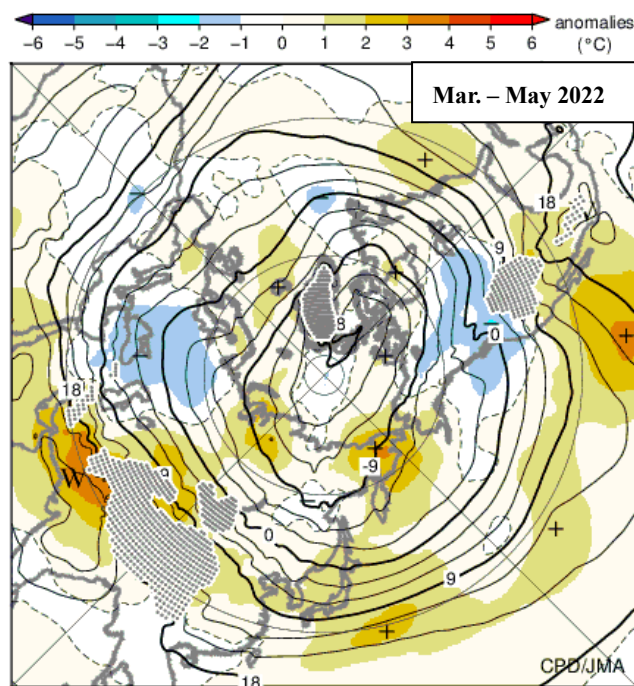




(e) 500-hPa height and anomaly



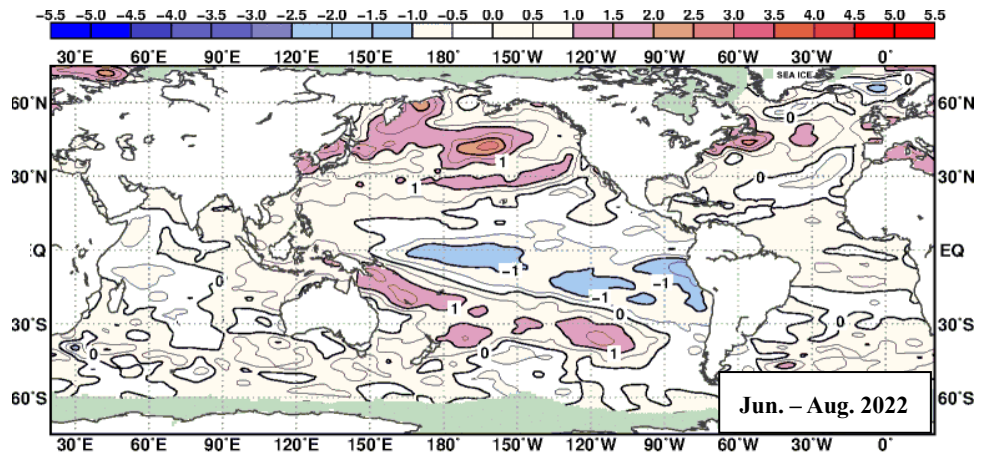
(f) SLP and anomaly



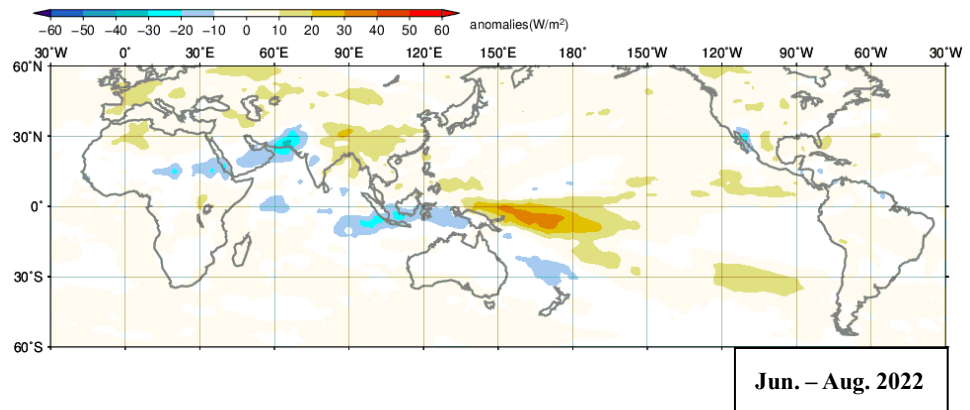
(g) 850-hPa temperature and anomaly

Figure 1.3-2 As per Figure 1.3-1, but for March – May 2022
In (g), contour interval is 3 degree C.

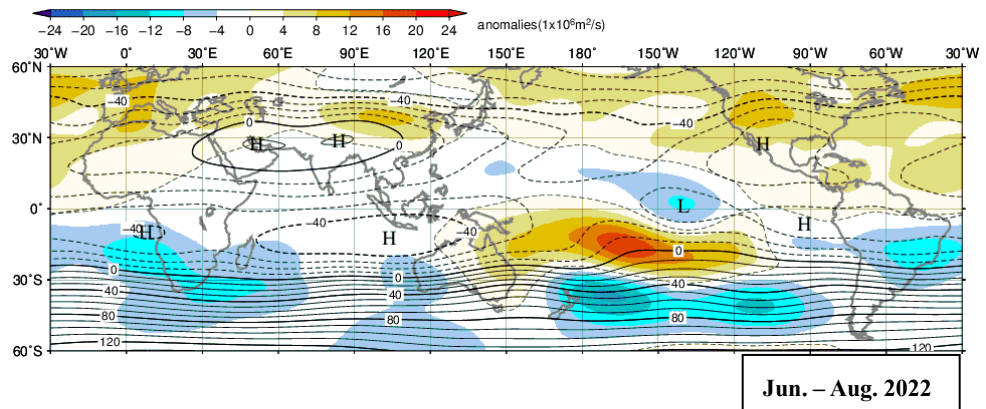
(a) SST anomaly



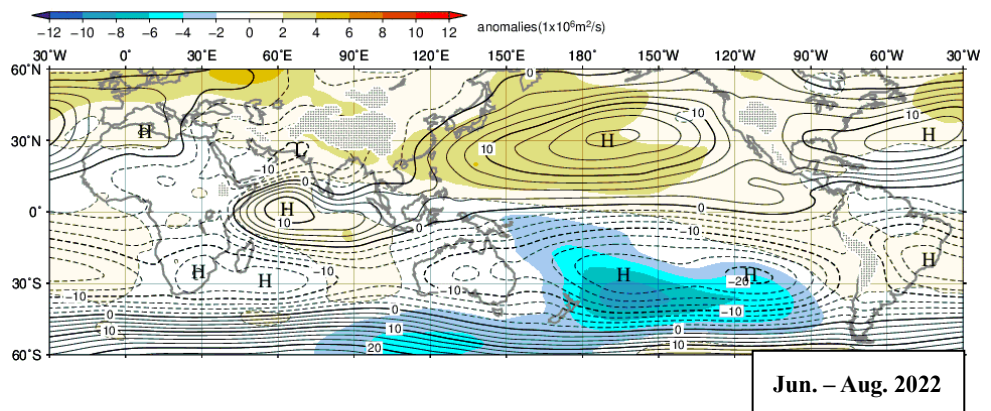
(b) OLR anomaly

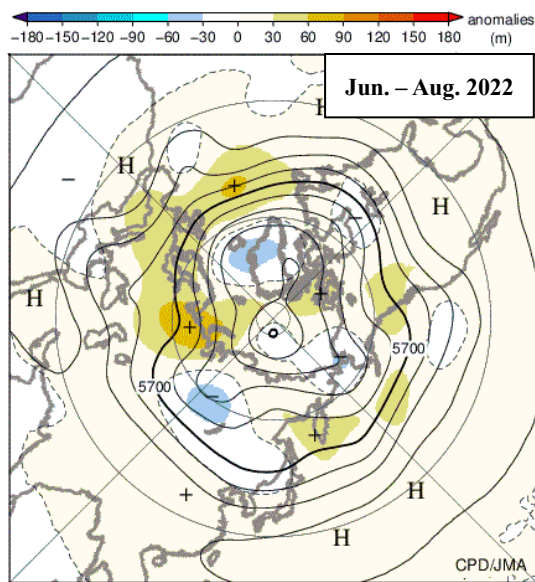


(c) 200-hPa stream function and anomaly

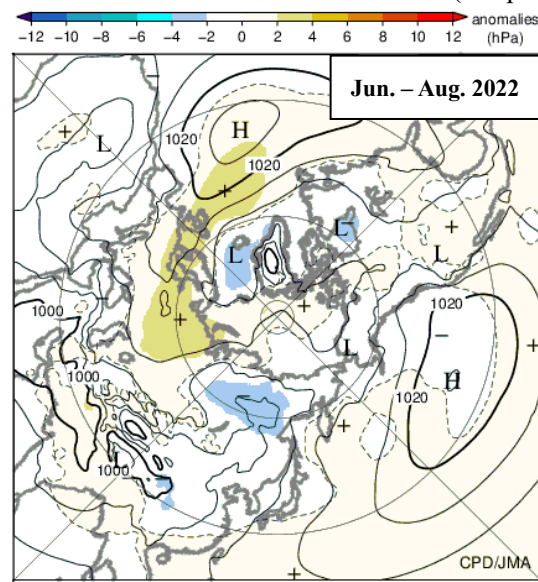


(d) 850-hPa stream function and anomaly

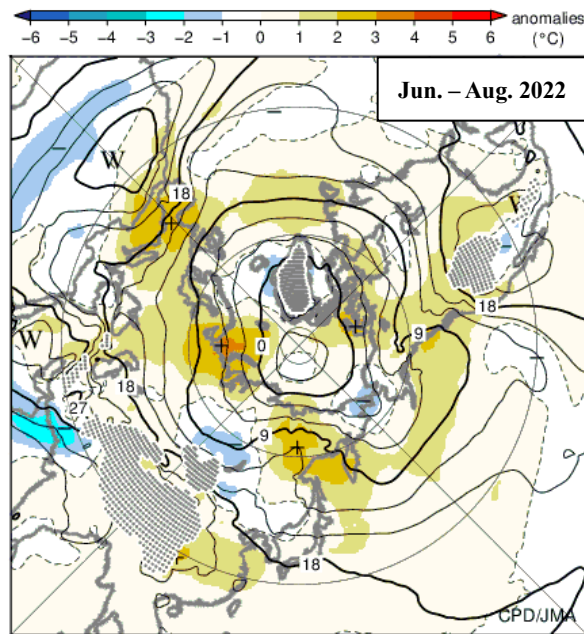




(e) 500-hPa height and anomaly



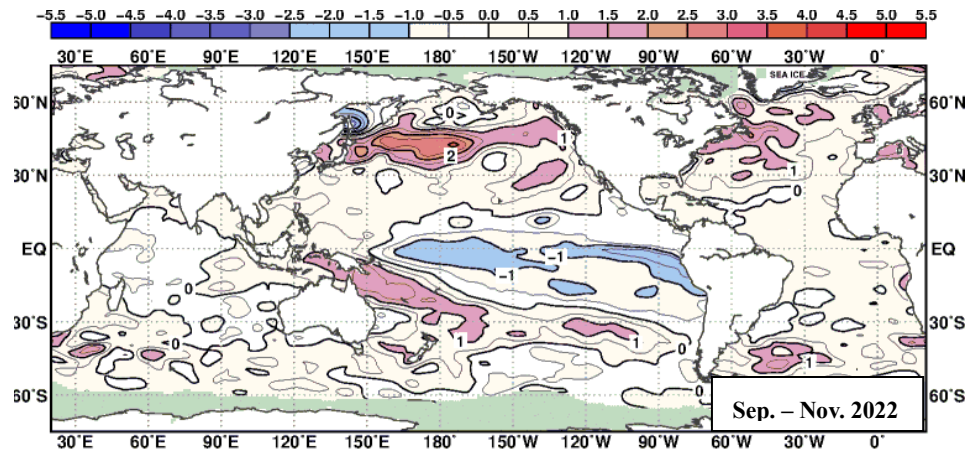
(f) SLP and anomaly



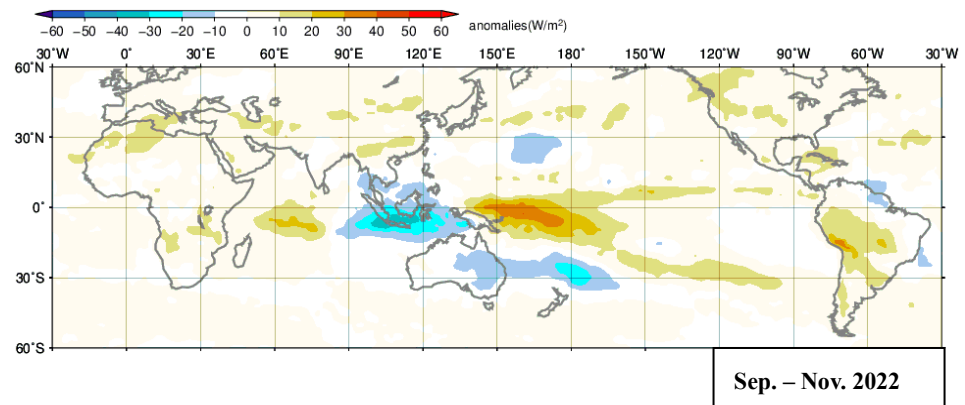
(g) 850-hPa temperature and anomaly

Figure 1.3-3 As per Figure 1.3-1, but for June – August 2022
In (g), contour interval is 3 degree C.

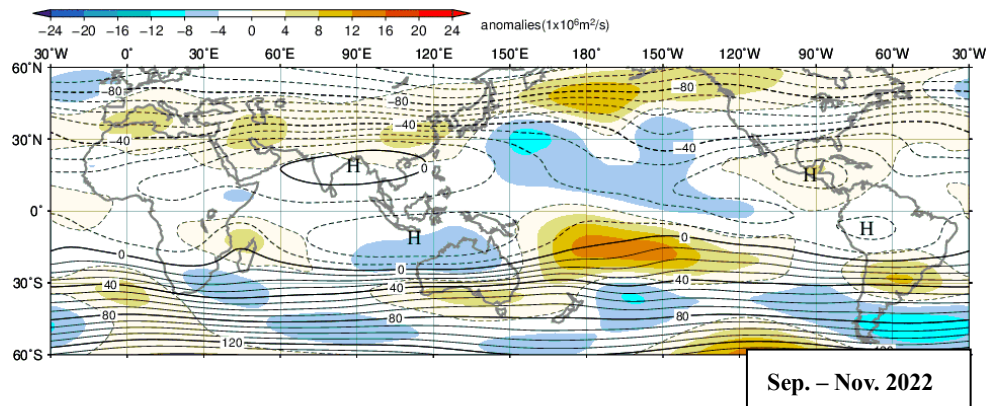
(a) SST anomaly



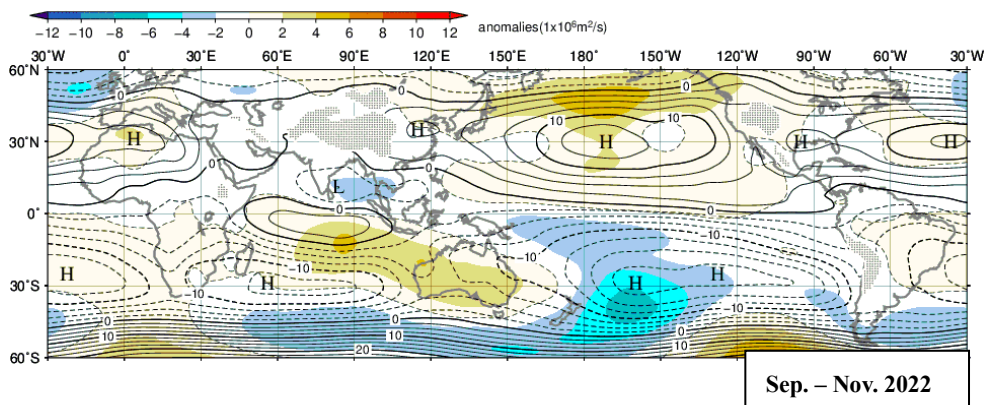
(b) OLR anomaly

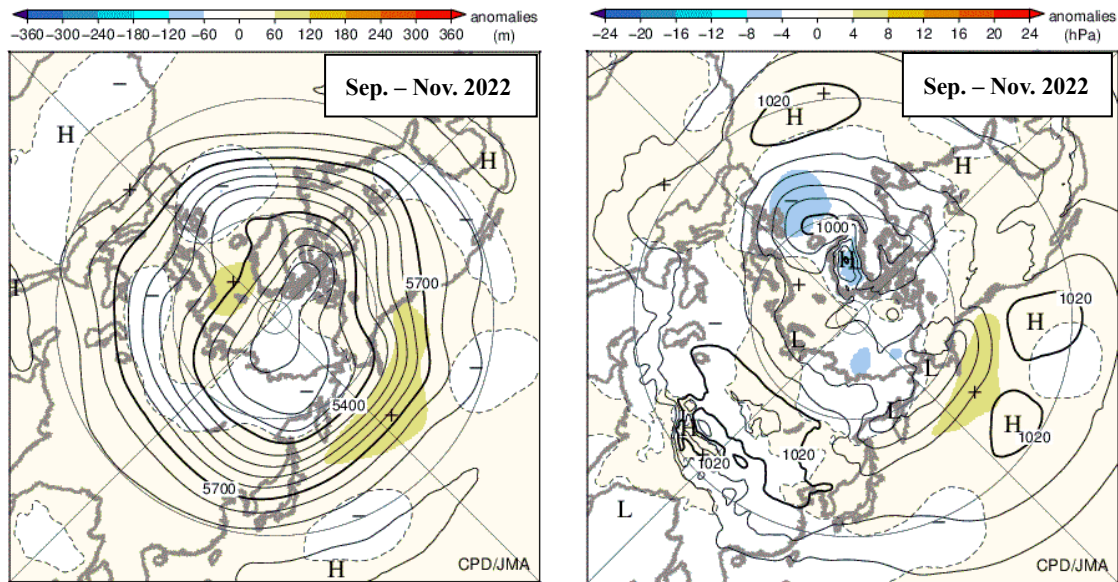


(c) 200-hPa stream function and anomaly



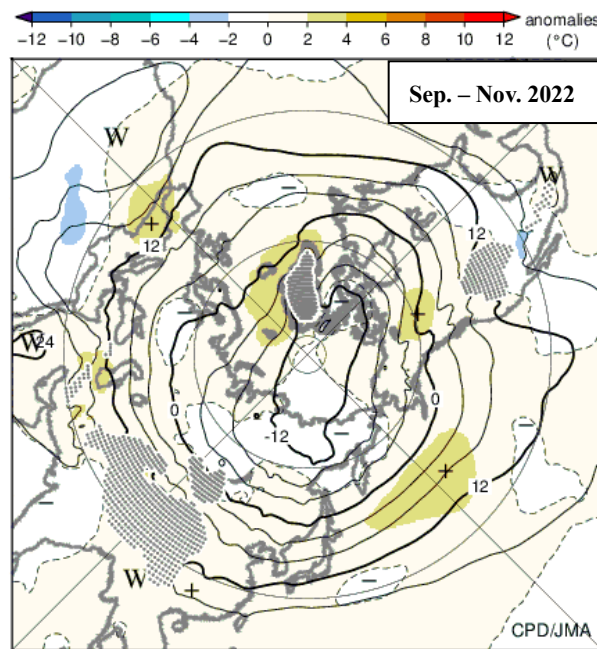
(d) 850-hPa stream function and anomaly





(e) 500-hPa height and anomaly

(f) SLP and anomaly



(g) 850-hPa temperature and anomaly

Figure 1.3-4 As per Figure 1.3-1, but for September – November 2022

1.3.2 Global average temperature in the troposphere

The global average temperature in the troposphere (Figure 1.3-5) remained higher than normal since summer 2021. The temperature anomaly of +0.5°C in July 2022 was the highest on record for the month since 1958. The monthly average zonal mean temperature during this period was higher than the normal for the whole troposphere (Figure 1.3-6).

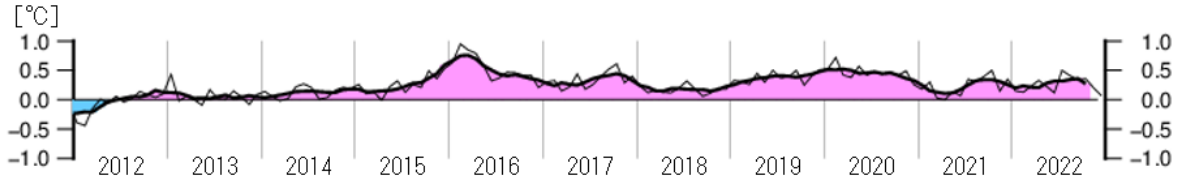


Figure 1.3-5 Time-series representation of global average temperature anomalies calculated from thickness in the troposphere (2012 to 2022)

The thin and thick lines show monthly mean and five-month running mean values, respectively. The base period for the normal is 1991 – 2020.

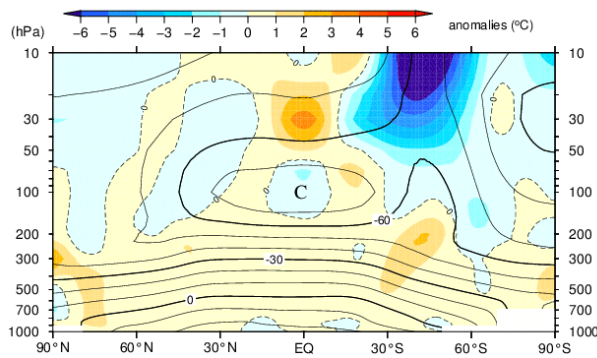


Figure 1.3-6 Latitude-height cross section of zonal mean temperature and anomaly (July 2022)

Contours show zonal mean temperature at intervals of 10 degree C, and shading indicates temperature anomalies. The base period for the normal is 1991 – 2020. “W” and “C” denote warm and cold conditions, respectively.

1.3.3 Asian summer monsoon

Convection during the 2022 Asian summer monsoon season (June – September) showed significant variability with a periodicity of around a month, particularly in the first half of the season, as indicated by the OLR index (SAMOI (A))¹³, JMA, 1997; Figure 1.3-7). Convection was enhanced from late June to early July and early August, and suppressed in mid-June and late July.

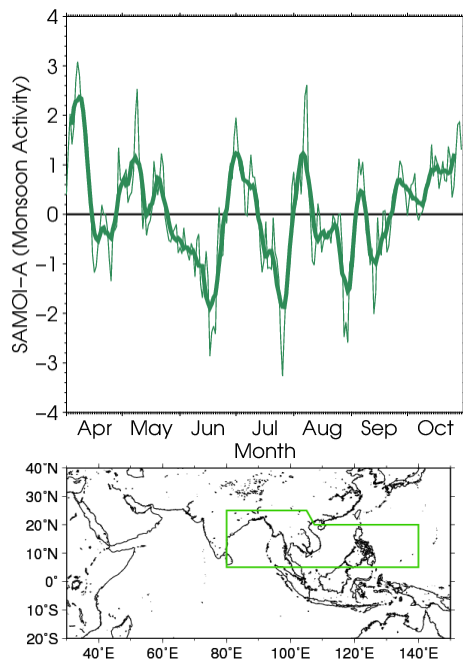


Figure 1.3-7 Time-series representation of the Asian summer monsoon OLR index (SAMOI (A)) (April – October 2022)

The thin and thick green lines indicate daily and seven-day running mean values, respectively. SAMOI (A) indicates the overall activity of the Asian summer monsoon, and positive and negative values indicate enhanced and suppressed convective activity, respectively, compared to the normal. The base period for the normal is 1991 – 2020. Original OLR data provided by NOAA.

¹³ SAMOI (A) is defined as reversed-sign area-averaged OLR anomalies normalized by its standard deviation. The area for average is enclosed by green line in the map of Figure 1.3-7.

1.3.4 Tropical cyclones over the western North Pacific and the South China Sea

In 2022, 25 tropical cyclones (TCs) with maximum wind speeds of ≥ 34 kt formed over the western North Pacific and the South China Sea (Figure 1.3-8, Table 1.3-1), which was similar to the normal of 25.1 (1991 – 2020 average). In the period up to July, a total of 6 TCs (normal 7.8) formed, while 19 TCs (normal 17.3) were formed since August.

A total of 11 TCs, which was similar to the normal of 11.7, came within 300 km of the Japanese archipelago. A total of 3 TCs, Tropical Storm Aere, Tropical Storm Meari and Typhoon Nanmadol made landfall on Japan, which was similar to the normal of 3.0.

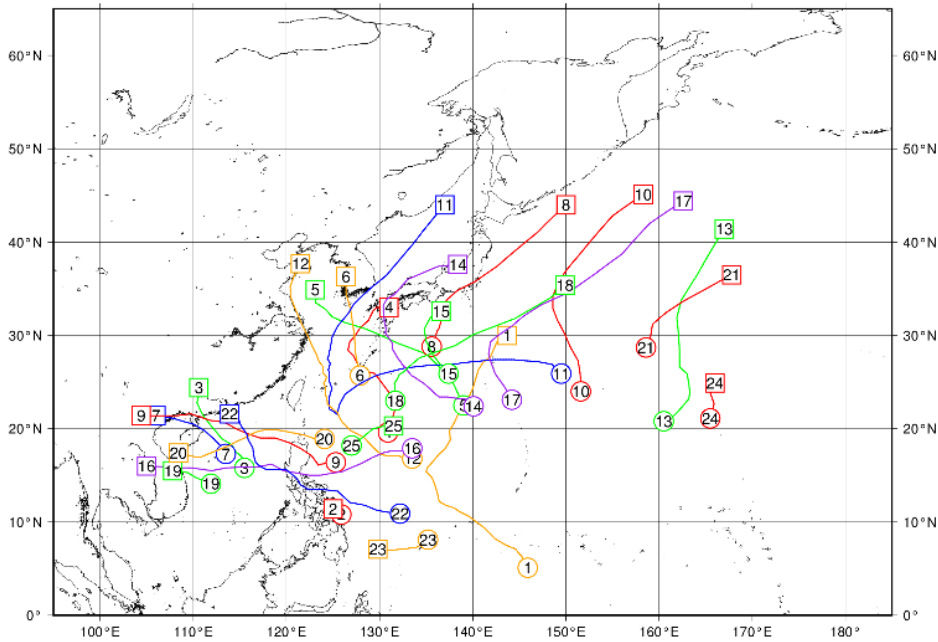


Figure 1.3-8 Tracks of TCs with maximum wind speeds of ≥ 34 kt in 2022

Numbered circles indicate positions of the TC formed (maximum wind speeds of ≥ 34 kt), and numbered squares indicate positions of the TC dissipated (maximum wind speeds lower than 34 kt). Source: RSMC Tokyo-Typhoon Center data.

Table 1.3-1 TCs with maximum wind speeds of ≥ 34 kt in 2022 (Source: RSMC Tokyo-Typhoon Center data)

Number ID	Tropical Cyclone	Duration (UTC)	Maximum Wind ¹⁾ (kt)	Number ID	Tropical Cyclone	Duration (UTC)	Maximum Wind ¹⁾ (kt)
2201	MALAKAS	0000, 08 Apr - 1200, 15 Apr	90	2214	NANMADOL	1800, 13 Sep - 1800, 19 Sep	105
2202	MEGI	1800, 09 Apr - 0000, 11 Apr	40	2215	TALAS	0000, 22 Sep - 1200, 23 Sep	35
2203	CHABA	0000, 30 Jun - 0600, 03 Jul	70	2216	NORU	1800, 22 Sep - 1200, 28 Sep	95
2204	AERE	1800, 30 Jun - 0000, 05 Jul	45	2217	KULAP	0000, 26 Sep - 1200, 29 Sep	60
2205	SONGDA	1200, 28 Jul - 1800, 31 Jul	40	2218	ROKE	1200, 28 Sep - 1800, 01 Oct	70
2206	TRASES	0000, 31 Jul - 1200, 01 Aug	35	2219	SONCA	0000, 14 Oct - 0000, 15 Oct	35
2207	MULAN	0600, 09 Aug - 0000, 11 Aug	35	2220	NESAT	0600, 15 Oct - 0000, 20 Oct	75
2208	MEARI	1200, 11 Aug - 1200, 14 Aug	40	2221	HAITANG	0000, 18 Oct - 1200, 19 Oct	35
2209	MA-ON	1800, 21 Aug - 0000, 26 Aug	55	2222	NALGAE	0000, 27 Oct - 1800, 02 Nov	60
2210	TOKAGE	0000, 22 Aug - 1800, 25 Aug	75	2223	BANYAN	1800, 30 Oct - 0000, 01 Nov	40
2211	HINNAMNOR	0600, 28 Aug - 1200, 06 Sep	105	2224	YAMANeko	1200, 12 Nov - 0600, 14 Nov	35
2212	MUIFA	1800, 07 Sep - 0000, 16 Sep	85	2225	PAKHAR	1200, 11 Dec - 1200, 12 Dec	40
2213	MERBOK	1200, 11 Sep - 0600, 15 Sep	70				

1) Estimated maximum 10-minute mean wind speed

Chapter 2 Climate Change

2.1 Greenhouse gases^{14,15}

- Atmospheric concentrations of carbon dioxide are increasing.
- Atmospheric concentrations of methane have shown an ongoing increase (with the exception of a stationary phase from 1999 to 2006).
- Atmospheric concentrations of nitrous oxide are increasing.
- Among halocarbons, atmospheric concentrations of chlorofluorocarbons are decreasing, while those of hydrofluorocarbons are increasing.

JMA operates the World Data Centre for Greenhouse Gases (WDCGG)¹⁶ to collect, maintain and provide data on greenhouse gases for related monitoring on a global scale under the Global Atmosphere Watch (GAW) Programme of the World Meteorological Organization (WMO). Analysis of data reported to WDCGG shows that the global mean concentration of long-lived greenhouse gases with strong effects on global warming (in particular, carbon dioxide (CO₂), methane (CH₄) and nitrous oxide (N₂O)) continues to increase (Table 2.1-1).

In Japan, JMA monitors surface-air concentrations of greenhouse gases via three observation stations at Ryori in Ofunato, Minamitorishima in the Ogasawara Islands and Yonagunijima in the Nansei Islands. JMA research vessels are used to observe oceanic and atmospheric CO₂ in sea areas near Japan and in the western North Pacific. In addition, sampling of greenhouse gases in upper-air areas using cargo aircraft was commenced in 2011 (Figure 2.1-1).

Table 2.1-1 Atmospheric concentrations of major long-lived greenhouse gases (2021)¹⁷

	Atmospheric mole fraction			Absolute increase from 2020	Relative increase from 2020	Lifetime
	Pre-industrial level around 1750	Global mean in 2021	Relative increase from Pre-industrial level			
Carbon dioxide	About 278 ppm	415.7 ppm	+ 49 %	+2.5 ppm	+0.61 %	-
Methane	About 729 ppb	1,908 ppb	+162 %	+18 ppb	+0.95 %	11.8 years
Nitrous oxide	About 270 ppb	334.5 ppb	+ 24 %	+1.3 ppb	+0.39 %	109 years

¹⁴ Part of this section shows observational outcomes for the period until 2021, as greenhouse gas observation data for 2022 were not yet fully available at the time of publication.

¹⁵ Information on greenhouse gas monitoring is published on JMA's website.

https://www.data.jma.go.jp/ghg/info_ghg_e.html (Atmospheric greenhouse gases)

¹⁶ See the WDCGG website for more information.

<https://gaw.kishou.go.jp/>

¹⁷ Data on the annual mean mole fraction in 2021 and its absolute and relative differences from the previous year are from WMO (2022), while data on pre-industrial levels and lifetime are from IPCC (2021). The lifetime of gas as referred to here describes the time scale over which a local instantaneous increment of gas decays. The increase from pre-industrial levels is calculated from mole fractions for the pre-industrial era and 2021.

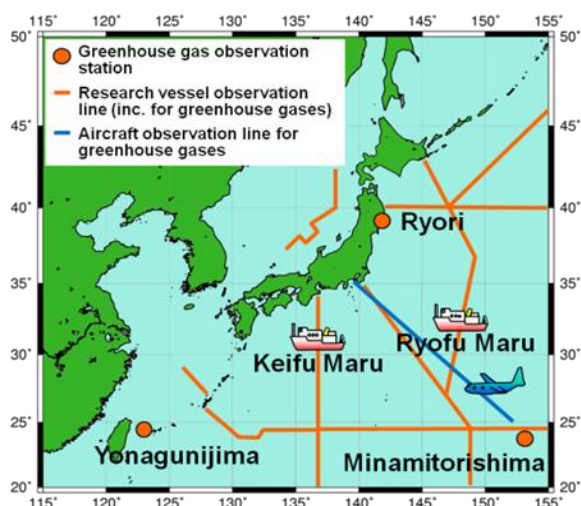


Figure 2.1-1 JMA's greenhouse gas observation network

Observation stations at Ryori, Minamitorishima and Yonagunijima and regular monitoring routes of research vessel and cargo aircraft

2.1.1 Concentration of carbon dioxide

(1) Concentration of global atmospheric carbon dioxide

The global mean concentration of atmospheric CO₂ shows a trend of increase with seasonal variations (Figure 2.1-2 (a)), primarily due to influences associated with human activity such as fossil fuel combustion and land-use changes (e.g., deforestation) (IPCC, 2021). Some anthropogenic CO₂ is absorbed by the terrestrial biosphere and the oceans, while the rest remains in the atmosphere. As most major sources of CO₂ are located in the Northern Hemisphere, concentrations tend to be higher in the mid- and high latitudes there and lower in the Southern Hemisphere (Figure 2.1-3).

The seasonal variability of CO₂ concentration is generally attributable to terrestrial biosphere activity. In summer, active plant photosynthesis consumes masses of CO₂, while emissions from plant respiration and organic-matter decomposition become dominant in winter (IPCC, 2021). As a result, the annual maximum concentration is observed from March to April in the Northern Hemisphere and from September to October in the Southern Hemisphere. Seasonal variations exhibit larger amplitudes in the mid- and high latitudes of the Northern Hemisphere than in the ocean-rich Southern Hemisphere (Figure 2.1-3). Accordingly, global mean CO₂ concentrations usually peak around April, reflecting strong seasonal variations in the Northern Hemisphere.

WDCGG analysis shows that global mean surface CO₂ concentration increased by 2.5 ppm from 2020 to 2021, reaching as much as 415.7 ppm (Table 2.1-1). The most recent 10-year average annual growth rate is 2.5 ppm/year, as opposed to the corresponding value of 1.5 ppm/year for the 1990s.

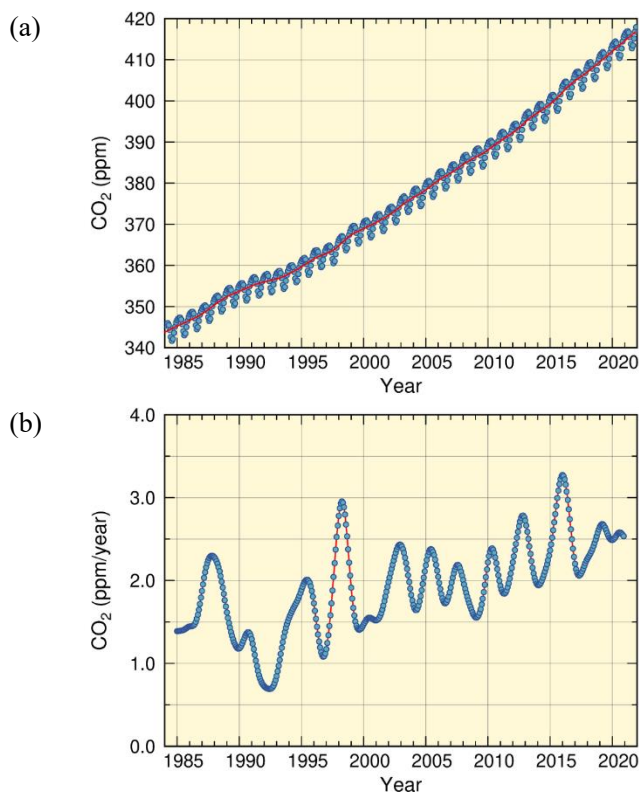


Figure 2.1-2 Global mean concentration of atmospheric CO₂ (a) and annual growth rate (b)
 In the upper panel the blue dots are monthly values, and the red line represents the corresponding sequence after removal of seasonal variations. From the latter, the growth rate is derived and shown in the lower panel. Graph content is based on analysis of observation data reported to WDCGG using the method of WMO (2009). Data contributors are listed in WMO (2023).

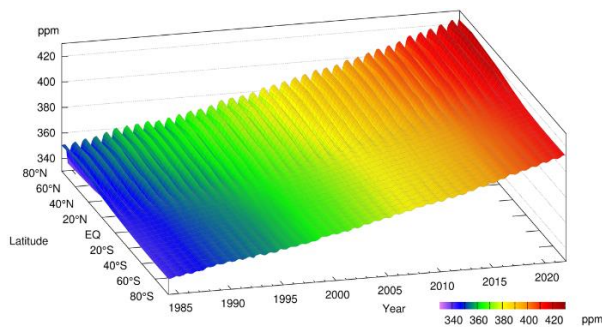


Figure 2.1-3 Latitudinal distribution of atmospheric CO₂ concentrations
 The data set and analysis method are as per Figure 2.1-2.

The growth rate of CO₂ concentration exhibits significant interannual variations (Figure 2.1-2 (b)). Major increases in concentration often coincide with El Niño events, largely because the terrestrial biosphere emits more CO₂ than usual under such conditions. In particular, El Niño events bring about high temperatures and droughts in tropical areas and elsewhere, thereby promoting plant respiration and organic-matter decomposition in soil and hindering plant photosynthesis (Keeling *et al.*, 1995; Dettinger and Ghil, 1998).

Figure 2.1-4 illustrates net CO₂ uptake by the terrestrial biosphere as estimated using the method of Le Quéré *et al.* (2016). Here, CO₂ uptake is defined as the amount of anthropogenic emissions minus the increment of atmospheric concentration and the amount of uptake by oceans. The low uptake by the terrestrial biosphere in 2015 and 2016 is generally attributed to the 2014 – 2016 El Niño event (WMO, 2018b). The annual net CO₂ uptakes in 2015 and 2016 were both lower than the 10-year average of 2.7 ± 1.2 GtC/year for the period 2011 – 2020. Similar suppression of net CO₂ uptake was observed in association with the El Niño events of 1997/1998 and 2002/2003. An exception was observed from 1991 to 1992, when net CO₂ uptake by the terrestrial biosphere was large despite the presence of an El Niño event. This is attributable to the eruption of Mt. Pinatubo in June 1991, which triggered worldwide low temperatures and inhibited CO₂ emissions from organic-matter decomposition in soil (Keeling *et al.*, 1996; Rayner *et al.*, 1999).

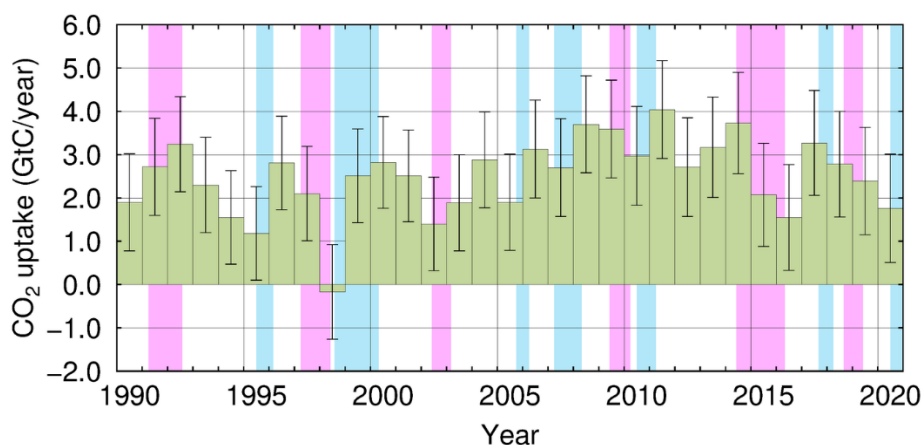


Figure 2.1-4 Annual net CO₂ uptake by the terrestrial biosphere

In this analysis, the net CO₂ uptake is estimated by subtracting the annual increment of atmospheric CO₂ and the amount of uptake by oceans from the amount of anthropogenic emissions. The amount of anthropogenic emissions stemming from fossil fuel combustion, cement production (including cement carbonation sinks) and land-use change is based on Friedlingstein *et al.* (2022). The annual increment of atmospheric CO₂ is the annual mean of the monthly means shown in Figure 2.1-2 (b). Oceanic uptake is based on Iida *et al.* (2021; see also Section 2.12.1 (2)), and incorporates emissions associated with the natural carbon cycle, corresponding to 0.6 GtC/year (IPCC, 2021). Error bars indicate 68% confidence levels. El Niño and La Niña periods are shaded in red and blue, respectively. A negative CO₂ uptake equates to an emission.

(2) Concentration of atmospheric carbon dioxide in Japan

Concentrations of atmospheric CO₂ at all three of Japan's observation stations have shown a continuous increase along with seasonal variations (Figure 2.1-5 (a)). The amplitude of these variations is greater at Ryori than at the other stations because it tends to be larger in higher latitudes of the Northern Hemisphere in association with significant seasonal variations in terrestrial biosphere activity in the mid- and high latitudes (see Figure 2.1-1). Although Yonagunijima and Minamitorishima have similar latitudes, the former tends to observe higher concentrations and seasonal variations with larger amplitudes because of its greater proximity to the Asian continent, which is characterized by major anthropogenic emissions and an extensive biosphere. The annual mean CO₂ concentration in 2022 was 421.8 ppm at Ryori, 419.7 ppm at Minamitorishima and 421.8 ppm at Yonagunijima (based on preliminary estimations). The increase from the previous year was 2.0 to 2.6 ppm/year, which is comparable to the mean annual absolute increase over the last 10 years. It should be noted that the analysis values here have been corrected by +0.10 to +0.25 ppm due to an update of the international observation standard for CO₂ under the National Oceanic and Atmospheric Administration (NOAA). It has been reported that fossil fuel-related emissions of carbon dioxide in 2020 decreased by about 5.2% from 2019 onward due to COVID-19 restrictions, while those for 2021 returned to 2019 levels. In 2022, values were expected to increase by around 1.0% from the previous year (Friedlingstein *et al.*, 2022). Concentrations of atmospheric CO₂ also continue to increase.

Figure 2.1-5 (b) shows growth rates of CO₂ concentrations observed at the three observation stations. High rates have been observed in most cases during the periods of El Niño events. As a recent example, a sharp increase in CO₂ concentration was observed in association with the event that ran from summer 2014 to spring 2016.

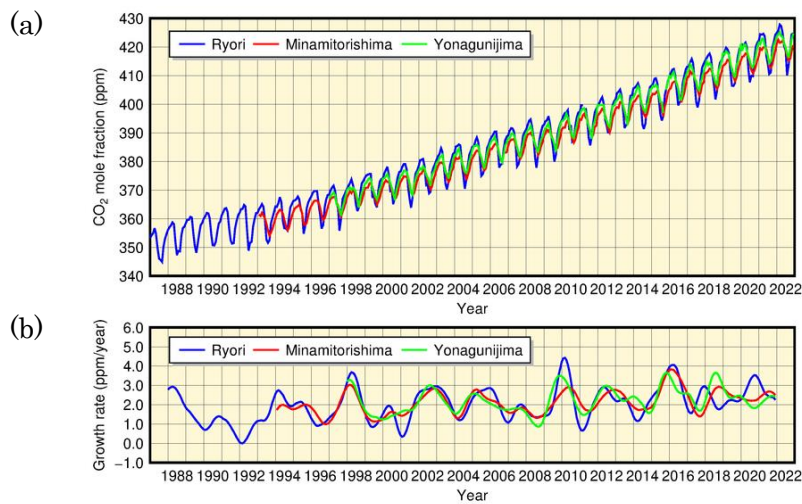


Figure 2.1-5 Monthly mean concentrations (a) and corresponding growth rates (b) of atmospheric CO₂ observed at Ryori (blue), Minamitorishima (red) and Yonagunijima (green)
The method used to calculate the growth rate is described in WMO (2009).

(3) Concentration of carbon dioxide in the upper air

Since 2011, JMA has monitored upper-air CO₂ concentrations using cargo aircraft with support from Japan Ministry of Defense, with air samples taken along the route from Atsugi Air Base (35.45°N, 139.45°E) to Minamitorishima Island (24.29°N, 153.98°E) during level flight at an altitude of approximately 6 km and during descent¹⁸ to the island once a month (Tsuboi *et al.*, 2013; Niwa *et al.*, 2014).

Figure 2.1-6 shows measured and averaged concentrations for samples collected during level flight in black and blue dots, respectively. Monthly mean concentrations at the ground-based station on the island are also shown in red. The dashed curves in blue and red represent components after removal of seasonal cycles for aircraft and Minamitorishima, respectively. Concentrations exhibit a gradual increase over time in the upper air as well as on the surface, although values tend to be lower in the former.

Figure 2.1-7 shows the vertical dependence of average seasonal cycles based on air samples collected during descent in addition to level-flight data and ground-based data. To allow direct comparison, these monthly values are calculated by averaging concentrations after removal of long-term trends in surface observation data. At each level, the information shows similar seasonal variations with higher values from winter to spring and lower values from summer to fall, while significant vertical dependence with lower values toward higher altitudes is observed from winter to spring. Consequently, the amplitude of seasonal cycles is smaller in the upper air.

Figure 2.1-8 shows concentrations for samples taken during descent minus the daily mean value recorded at the ground-based station on the flight date for February (left) and August (right). While concentrations are lower toward higher altitudes in February, there is no clear vertical dependence in August.

The above results suggest that parts of surface air affected by the terrestrial biosphere in continental regions are transported to the ground and upper levels of the island, and that air transport behavior varies with seasons and altitudes. The characteristic of strong vertical dependence from winter to spring and weak dependence from summer to fall is also identified in data from other aircraft observations around North America and Asia (Sweeney *et al.*, 2015; Umezawa *et al.*, 2018).

¹⁸ Although some air samples are taken during ascent flights from Minamitorishima Island, all vertical samplings are referred to here as descent samplings.

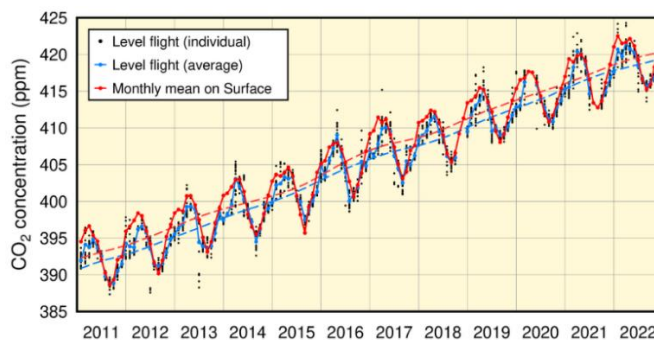


Figure 2.1-6 Measured and single-cruise average CO₂ concentrations for air samples collected during level flight (height: approx. 6 km) of cargo aircraft from Atsugi Air Base to Minamitorishima (black and blue dots, respectively) and monthly mean concentrations at the Minamitorishima ground station (red dots).

Blue and red dashed lines represent components after the removal of seasonal cycles from the series of blue and red dots, respectively. The analysis is based on WMO (2009).

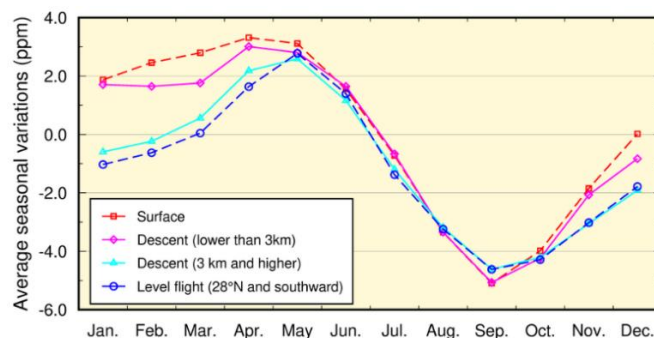


Figure 2.1-7 Vertical dependence of average seasonal cycles around Minamitorishima for monthly mean concentrations on the surface (red), concentrations for air samples taken during level flight at latitudes of 28°N and southward (blue), and values recorded during descent with altitudes less than 3 km (magenta) and otherwise (cyan) based on data covering the period from February 2011 to December 2022.

Monthly values are calculated by averaging concentrations after removal of long-term trends (components without seasonal cycles) for surface observation data (the red dashed line in Figure 2.1-6).

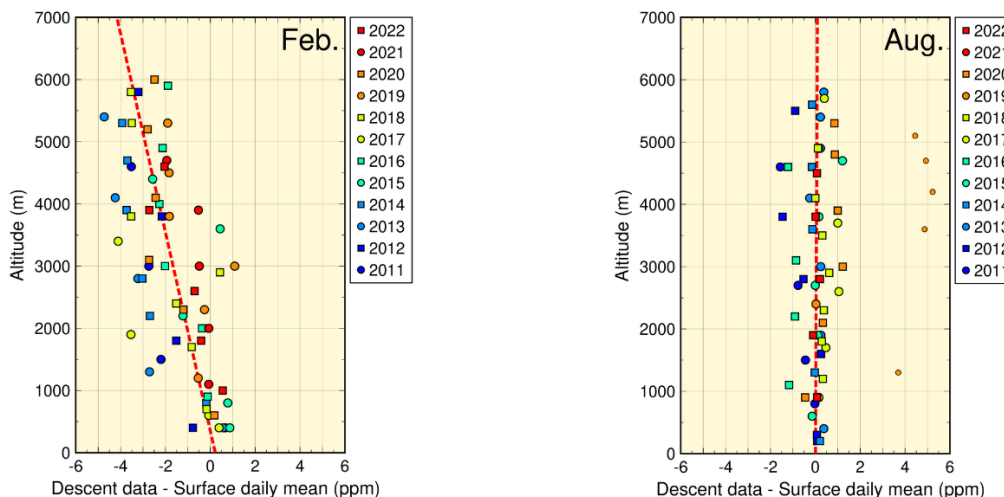


Figure 2.1-8 Vertical variations of CO₂ concentrations over Minamitorishima

Circles and squares show concentrations of air samples taken during descent to the island minus the daily mean value recorded at the ground-based station on the flight date. Symbol colors and shapes represent observation years. Dashed red lines show the vertical gradient of the symbols as determined using the least squares method. To determine representative characteristics for the observation area, outlier data (small symbols) beyond the 3 sigma of the residual standard deviation from the fitted line are excluded from calculation for the vertical gradient. On the flight date in August 2019, daily mean concentration on the surface was 4 – 5 ppm lower than that during descent because continental air masses with low CO₂ concentrations were transported to areas near the ground around Minamitorishima. It should be noted that observations for August 2021 were missing.

2.1.2 Concentration of methane

(1) Concentration of global atmospheric methane

The global mean concentration of atmospheric CH₄ has been increasing since at least the mid-1980s when worldwide monitoring began, except for a stationary phase from 1999 to 2006 (Figure 2.1-9). IPCC (2021) reported that anthropogenic emissions from the oil and gas sectors declined through the 1990s, and that concurrent emission changes from fossil fuels and the agricultural sector may be responsible for the greater concentrations observed since 2007. Meanwhile, large uncertainties still remain in relation to CH₄ emissions from wetlands and biomass combustion driven by El Niño Southern Oscillation and variations in hydroxyl radicals, which contribute to CH₄ destruction.

WDCGG analysis shows that the global mean concentration of CH₄ in 2021 was 1,908 ppb, which is the highest since records began. The annual increase from 2020 to 2021 was 18 ppb, which was the largest since 1984 (Table 2.1-1) (News IV).

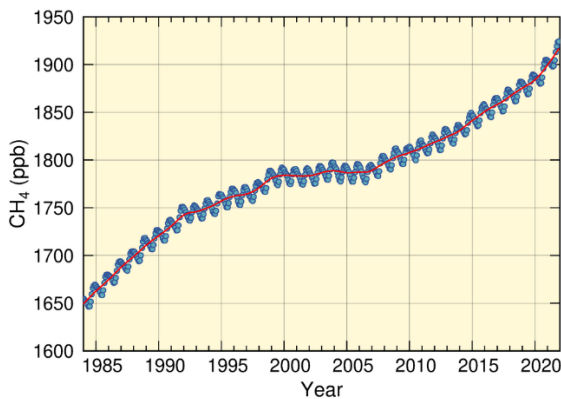


Figure 2.1-9 Global mean concentration of atmospheric CH₄

The blue dots are monthly values, and the red line represents the corresponding sequence after the removal of seasonal variations. Graph content is based on analysis of observation data reported to WDCGG based on the method of WMO (2009). Data contributors are listed in WMO (2023).

Figure 2.1-10 shows the latitudinal dependence of CH₄ concentrations. Values are lower in the tropics than in the high and mid-latitudes of the Northern Hemisphere because CH₄ is mostly emitted from land areas in the Northern Hemisphere, and disappears due to reaction with hydroxyl radicals over tropical oceans during transportation to the Southern Hemisphere. In summer, more CH₄ is destroyed because more hydroxyl radicals are produced as a result of enhanced ultraviolet radiation and water vapor. This reaction contributes to seasonal variations of CH₄ concentrations in both hemispheres, with lower values in summer and higher values in winter (Figures 2.1-9 and 2.1-10).

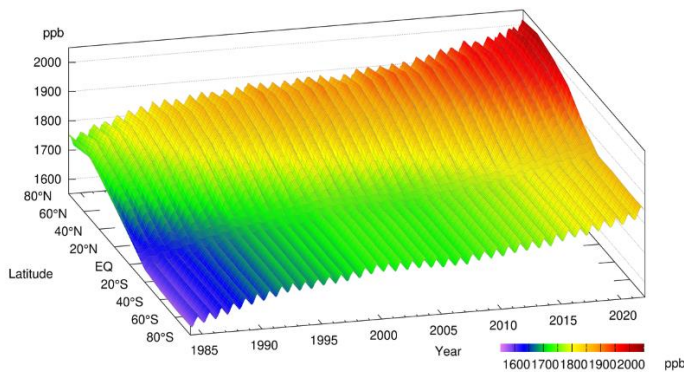


Figure 2.1-10 Latitudinal distribution of atmospheric CH₄ concentrations

The data set and analysis method are as per Figure 2.1-9.

The remarkable increase observed in global mean atmospheric concentrations of CH₄ since the industrial era (+162%) has been much more rapid than that of CO₂ (+49%) (Table 2.1-1). This is partly because around 40% of CH₄ released into the atmosphere is of natural origin (wetlands, termites, etc.) and around 60% is from

human-related activity sources (ruminants, rice paddies, fossil fuel mining, landfill, biomass burning, etc.), and anthropogenic emissions of CH₄ exceed natural emissions. The long-term trend of CH₄ concentration depends on various factors of uncertainty, including anthropogenic/natural emissions and chemical reactions. Accordingly, further development of the global CH₄ observation network is required.

(2) Concentration of atmospheric methane in Japan

Atmospheric CH₄ concentrations at all of Japan's three observation stations exhibit a trend of increase with seasonal variations in the same way as the global mean concentration (Figure 2.1-11 (a)). Ryori usually observes the highest concentration among the three stations because it is located in the northern part of Japan, where CH₄ sources in the Asian continent are more influential and reaction with hydroxyl radicals is less marked. Although Yonagunijima and Minamitorishima are located at similar latitudes, the former tends to record higher concentrations in winter because CH₄ sources on the Asian continent have a stronger impact there in winter as a result of continental air mass expansion. In summer, meanwhile, a hydroxyl radical-rich maritime air mass covers both stations, and similarly low concentrations are observed. Since 2010, Yonagunijima has occasionally observed concentrations as high as those of Ryori in winter. The annual mean CH₄ concentration in 2022 was 1,997 ppb at Ryori, 1,947 ppb at Minamitorishima and 1,967 ppb at Yonagunijima, all of which are the highest on record (based on preliminary estimations). The annual increase from 2020 to 2021 was the largest at Ryori and Minamitorishima (16 and 19 ppb, respectively) and the third largest at Yonagunijima (13 ppb) since records began (News IV).

The growth rate of atmospheric CH₄ concentration exhibits interannual variations that differ significantly from station to station (Figure 2.1-11 (b)).

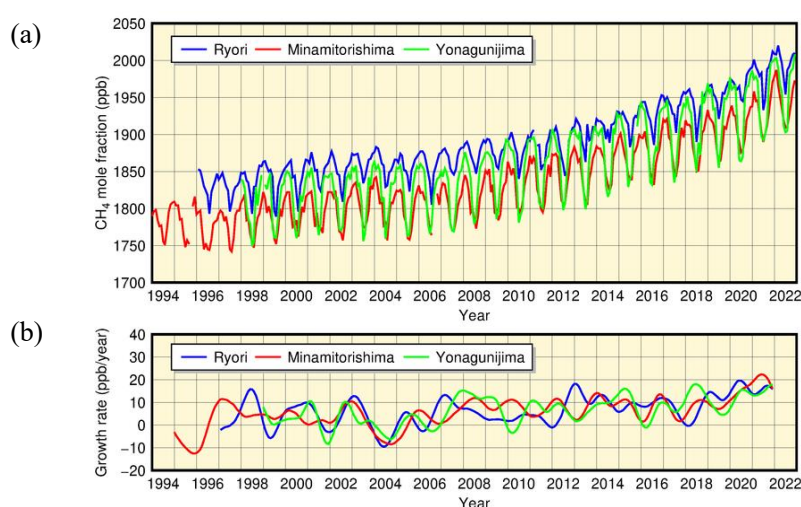


Figure 2.1-11 Monthly mean concentrations (a) and corresponding growth rates (b) of atmospheric CH₄ observed at Ryori (blue), Minamitorishima (red) and Yonagunijima (green)
The method for calculating the growth rate is described in WMO (2009).

2.1.3 Concentration of nitrous oxide

Figure 2.1-12 shows that the global mean concentration of atmospheric N₂O has been continuously increasing. The annual mean concentration in 2021 was 334.5 ppb, which was 24% above the pre-industrial level of 270 ppb (Table 2.1-1). Around 57% of N₂O released into the atmosphere is of natural origin (oceans, soil, etc.), and around 43% is from human activity-related sources (biomass burning, nitrate fertilizers, various industrial processes, etc.). Seasonal variations of N₂O concentrations were lower than those of CH₄ because N₂O has a longer lifetime (109 years). The hemispheric mean concentration is approximately 1 ppb higher in the Northern Hemisphere than in the Southern Hemisphere (Figure 2.1-13) because there are more sources of anthropogenic emissions in the former. This inter-hemispheric difference is, however, much smaller than those observed with

CH₄ due to the long atmospheric lifetime of N₂O.

The atmospheric N₂O concentration at Ryori exhibits characteristics similar to those of the global mean (Figure 2.1-14). The annual mean concentration in 2022 at Ryori was 338.2 ppb (based on preliminary estimations).

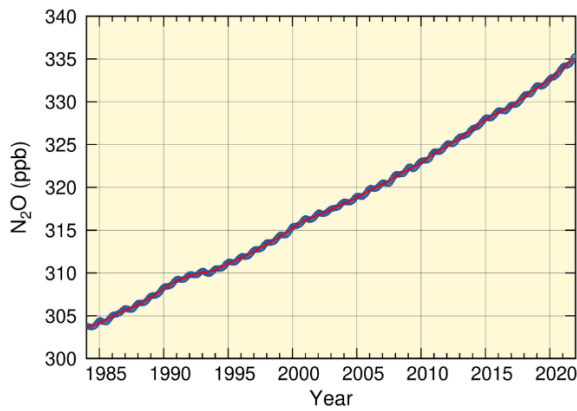


Figure 2.1-12 Global mean concentration of atmospheric N₂O

The blue dots are monthly values, and the red line represents the corresponding sequence after the removal of seasonal variations. Graph content is based on analysis of observation data reported to WDCGG based on the method of WMO (2009). Data contributors are listed in WMO (2023).

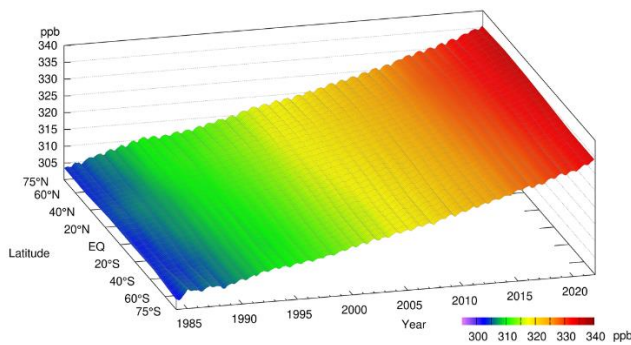


Figure 2.1-13 Latitudinal distribution of atmospheric N₂O concentrations

The data set and analysis method are as per Figure 2.1-12.

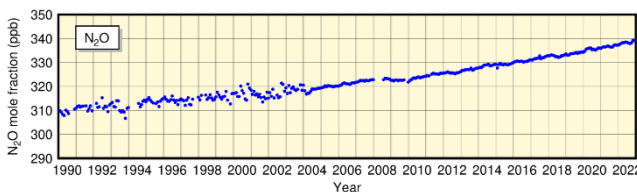


Figure 2.1-14 Monthly mean concentrations of atmospheric N₂O at Ryori

Improvement of observation equipment in 2004 resulted in improved stability of measurements.

2.1.4 Concentration of halocarbons

Halocarbons are generally carbon compounds containing halogens such as chlorine and bromine, many of which are powerful greenhouse gases whose atmospheric concentrations have increased rapidly since the second half of the 20th century due to artificial production. Although their atmospheric concentrations are only around a millionth those of CO₂, their greenhouse effect per unit mass is several thousand times greater.

Chlorofluorocarbons (CFCs: CFC-11, CFC-12 and CFC-113 among others), which are compounds of carbon, fluorine and chlorine, and other halogenated gases are ozone-depleting substances (ODSs). They are regulated under the 1987 Montreal Protocol on Substances that Deplete the Ozone Layer and its Amendments and Adjustments.

Hydrofluorocarbons (a halocarbon variety consisting of carbon compounds containing fluorine and hydrogen, referred to here as HFCs) have no effects on stratospheric ozone depletion and have been used as substitutes for CFCs. However, the Kigali Amendment of 2016 added HFCs to the list of substances subject to regulation under the Montreal Protocol (effective as of 2019) due to their significant greenhouse effects.

(1) Global concentration of halocarbons

Global concentrations of atmospheric CFCs increased rapidly until the 1980s before entering a decreasing trend in the 1990s (Figure 2.1-15). The concentration of CFC-11 peaked in 1992 – 1994, and has since shown a decreasing tendency. The concentration of CFC-12 increased until around 2003, and has also since shown a decreasing tendency. The concentration of CFC-113 reached its maximum in around 1993 in the Northern Hemisphere and around 1996 in the Southern Hemisphere. Differences in the concentrations of these gases between the Northern Hemisphere, where most emissions sources are located, and the Southern Hemisphere, which has significantly fewer sources, have decreased since the 1990s in contrast to the situation of the 1980s. These observations indicate that the CFC emission controls under the Montreal Protocol have been effective.

However, a slowdown in the decline of CFC-11 concentrations has been observed since 2012, with a rate of decrease approximately two thirds of that seen from 2002 to 2012. Results from numerical model calculation suggest that this is attributable to increased global CFC-11 emissions with main sources probably located in eastern Asia (WMO, 2018a; WMO, 2018b; Montzka *et al.*, 2018; Rigby *et al.*, 2019). Since 2018, ground-based observations and numerical model calculation results have suggested a resumed trend of decline in CFC-11 emissions from East Asia (Park *et al.*, 2021), and global ground-based observations have also shown an accelerated decrease in the growth rate of atmospheric CFC-11 concentrations since 2019 (Montzka *et al.*, 2021).

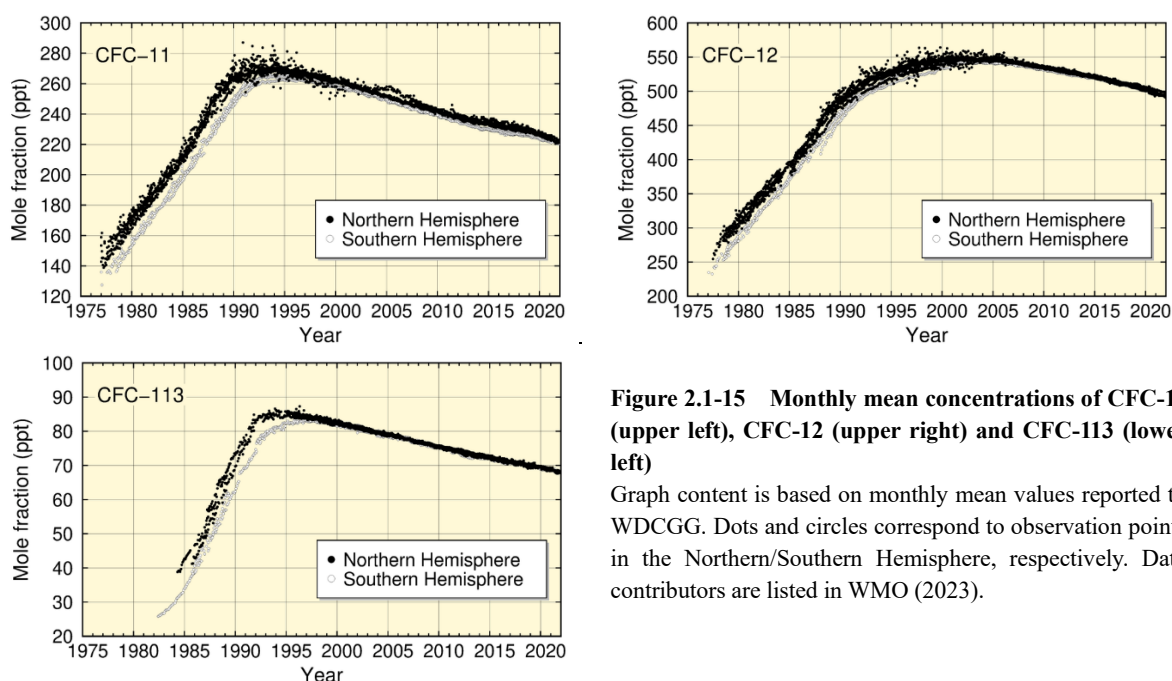


Figure 2.1-15 Monthly mean concentrations of CFC-11 (upper left), CFC-12 (upper right) and CFC-113 (lower left)

Graph content is based on monthly mean values reported to WDCGG. Dots and circles correspond to observation points in the Northern/Southern Hemisphere, respectively. Data contributors are listed in WMO (2023).

As with CFCs, atmospheric concentrations of HFCs are higher in the Northern Hemisphere, where there are more emissions sources than in the Southern Hemisphere (Figure 2.1-16). Atmospheric concentrations of HFC-134a continue to increase, while those of HFC-152a have levelled off in recent years. The difference of atmospheric concentrations of HFC-152a between the Northern Hemisphere and the Southern Hemisphere is large due to its short atmospheric lifetime and atmospheric concentrations of HFC-152a show remarkable seasonal variations.

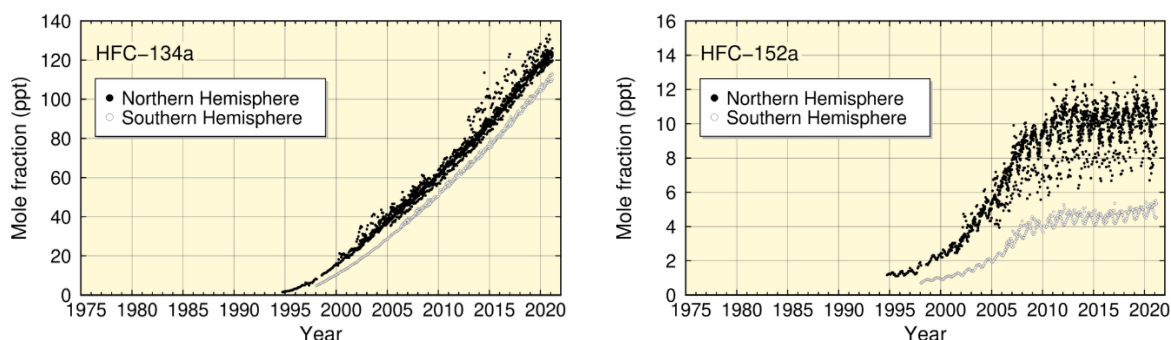


Figure 2.1-16 Monthly mean concentrations of HFC-134a (left) and HFC-152a (right)
The dataset and analysis method are as per Figure 2.1-15.

(2) Concentrations of halocarbons in Japan

Concentrations of CFC-11, CFC-12 and CFC-113 at Ryori have shown decreasing tendencies since reaching maxima in various years (Figure 2.1-17). The concentration of CFC-11 peaked at about 270 ppt in 1993 – 1994, and has since decreased. The distinct peak of concentration observed in 2011 is considered attributable to emissions from polyurethane foam insulation materials released by the Great East Japan Earthquake and the subsequent hugely destructive tsunami of 11 March 2011 (Saito *et al.*, 2015). The rate of increase in CFC-12 concentration slowed around 1995, and a gradual decrease has been seen since 2005. There was no clear tendency of increase or decrease in the concentration of CFC-113 until 2001, but a decreasing tendency has been seen since then.

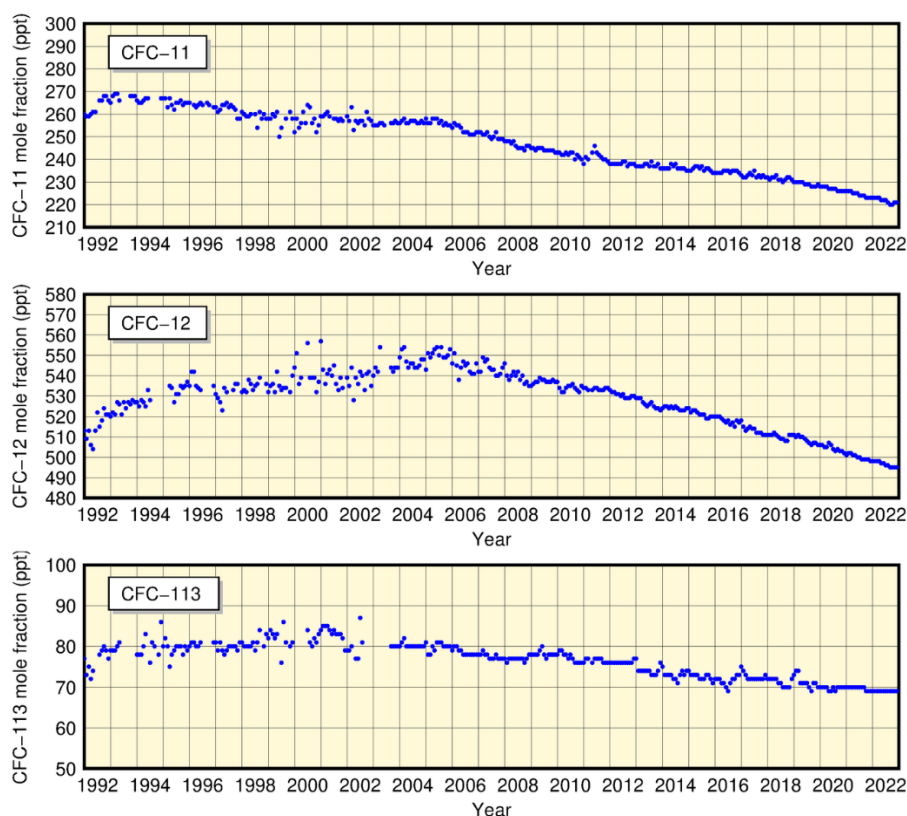


Figure 2.1-17 Monthly mean atmospheric concentrations of CFC-11 (top), CFC-12 (middle) and CFC-113 (bottom) at Ryori

Improvement of observation equipment in September 2003 resulted in improved stability of measurements.

The Japan Meteorological Agency began observing atmospheric HFC concentrations at Minamitorishima in April 2020. The results show that values for HFC-134a and HFC-152a are similar to those at other observation sites in the Northern Hemisphere in the context of global observation (Figure 2.1-18). In particular, atmospheric concentrations of HFC-152a show remarkable seasonal variations with higher concentrations from winter to spring and lower concentrations from summer to fall. Against this background, ongoing long-term monitoring is considered important.

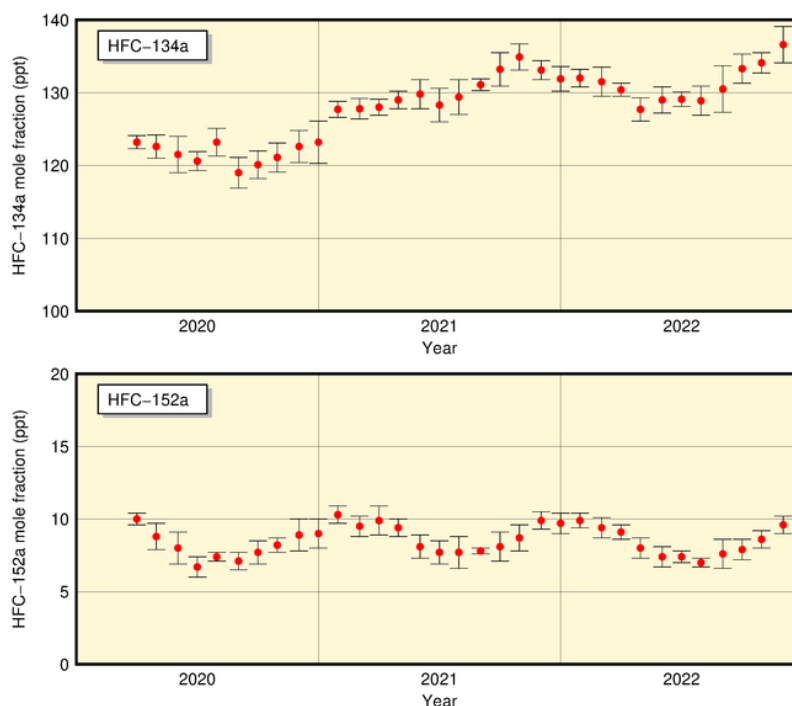


Figure 2.1-18 Monthly mean atmospheric concentrations of HFC-134a (top) and HFC-152a (bottom) at Minamitorishima

Observation of atmospheric HFC concentrations was started in April 2020 at Minamitorishima.

2.2 Aerosols and surface radiation¹⁹

- Background atmospheric turbidity coefficients (which depend on concentrations of aerosols, water vapor and other variables) in Japan from 1960 onward show several local maxima up to the early 1990s due to aerosol-related high turbidity in the stratosphere from large-scale volcanic eruptions. The January 2022 eruption of Hunga Tonga-Hunga Ha'apai have not shown a significant impact on these values so far.
- The number of days when any meteorological station in Japan observed Kosa was 8 in 2022, and the total number of stations reporting its occurrence during the year was 11.

2.2.1 Aerosols

Interannual variations in atmospheric turbidity coefficients from 1960 onward, as calculated from direct solar radiation measurements taken at five stations in Japan excluding the fluctuation component of the troposphere, show clear impacts of stratospheric aerosols resulting from volcanic eruptions (Figure 2.2-1). The increased turbidity coefficients observed for several years after 1963 and during the periods of 1982 – 1983 and 1991 – 1993 were caused by the eruptions of Mt. Agung (Indonesia) in 1963, Mt. El Chichón (Mexico) in 1982 and Mt. Pinatubo (Philippines) in 1991, respectively. The increased turbidity stems from the persistent presence of sulfate aerosol in the stratosphere resulting from huge amounts of sulfur dioxide (SO₂) released by the volcanic eruptions. The turbidity coefficient has now returned to approximately the same level as that observed before the eruption of Mt. Agung because no large-scale eruptions have occurred since that of Mt. Pinatubo. The impact of the large-scale eruption at Hunga Tonga-Hunga Ha'apai (Tonga) in January 2022 on background atmospheric turbidity coefficients in Japan remained relatively small during the same year, possibly because less sulfur dioxide was injected into the stratosphere than with the Pinatubo eruption. However, influence from the eruption may be observed from 2023 onward (News III).

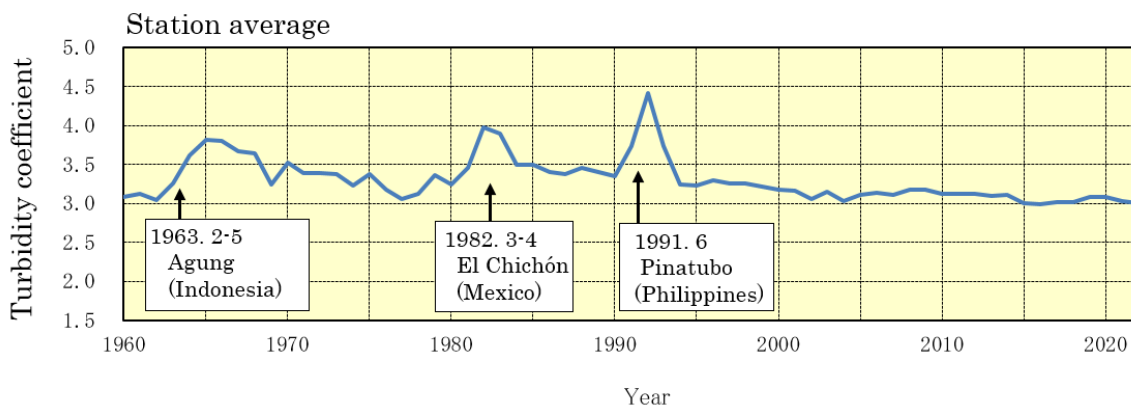


Figure 2.2-1 Time-series representation of annual mean atmospheric turbidity coefficients (1960 – 2022)

To eliminate the influence of variations in tropospheric constituents such as water vapor, dust and air pollutants, the annual mean atmospheric turbidity coefficient is calculated using the minimum turbidity coefficient for each month. Arrows indicate significant volcanic eruptions.

¹⁹ See the Glossary for terms relating to aerosols. Information on surface radiation and Kosa is published on JMA's website. <https://www.data.jma.go.jp/env/kosahp/en/kosa.html> (Aeolian Dust (Kosa))
https://www.data.jma.go.jp/env/radiation/en/info_rad_e.html (Solar and Infrared Radiation)

2.2.2 Kosa (Aeolian dust)

Kosa (Aeolian dust) is a kind of aerosol blown up from semi-arid areas of the Asian continent and transported by westerly winds to Japan. A total of 11 JMA meteorological stations (as of 31 December 2022) perform Kosa monitoring. The phenomenon is recorded when visually observed by station staff. The number of days when any meteorological station in Japan observed Kosa was 8 in 2022 (Figure 2.2-2), and the total number of stations reporting its occurrence during the year was 11 (Figure 2.2-3).

Neither the number of days on which Kosa was observed nor the annual total number of stations reporting observation show any discernible trend between 1967 and 2022. As the phenomenon shows significant interannual variability, ongoing data collection is necessary to clarify related trends.

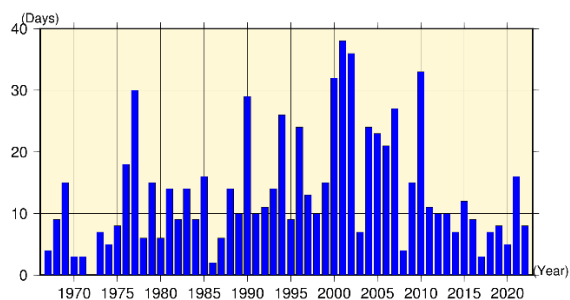


Figure 2.2-2 Number of days when any station in Japan observed Kosa (1967 – 2022) based on the 11 stations that were active for the whole period

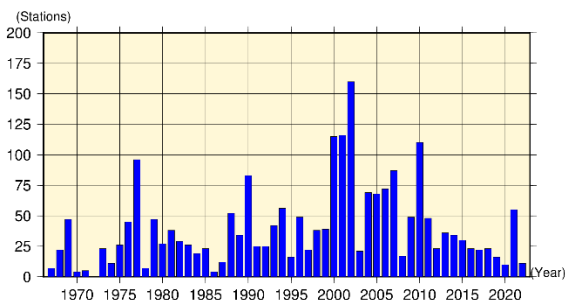


Figure 2.2-3 Annual total number of stations observing Kosa in Japan (1967 – 2022) based on the 11 stations that were active for the whole period

2.2.3 Solar radiation and downward infrared radiation

The earth's radiation budget is a source of energy for climate change, and monitoring of its variations is important. To this end, JMA conducts measurements of direct solar radiation, diffuse solar radiation and downward infrared radiation²⁰ at five stations in Japan (Abashiri, Tsukuba, Fukuoka, Ishigakijima and Minamitorishima) (Figure 2.2-4).

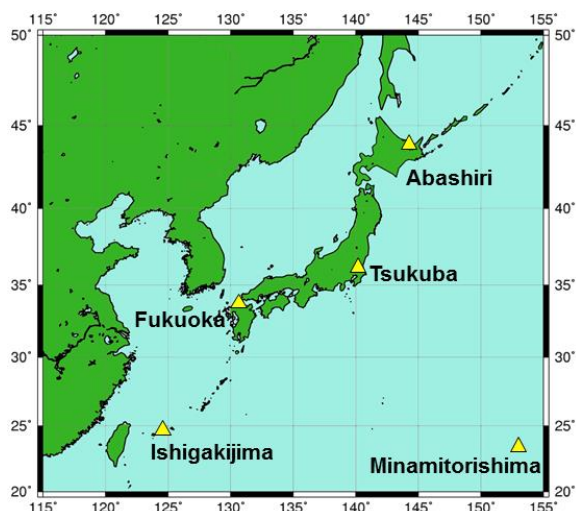


Figure 2.2-4 JMA's solar radiation and infrared radiation observation network

JMA conducts observation of direct solar, diffuse solar and downward infrared radiation at five stations (Abashiri, Tsukuba, Fukuoka, Ishigakijima and Minamitorishima).

²⁰ Downward infrared radiation is the incident infrared radiation acting on the earth's surface from all directions in the sky. It is emitted from clouds and atmospheric constituents such as water vapor and carbon dioxide in proportion to the fourth power of their temperature, and can be used as an index of global warming.

(1) Global solar radiation

Reports indicate that global solar radiation²¹ decreased from around 1960 to the late 1980s before increasing rapidly from the late 1980s to around 2000, and no obvious changes have been observed in most regions of the world (Ohmura, 2009). In Japan, global solar radiation declined from the late 1970s to around 1990 before increasing from around 1990 to the early 2000s. Since then, data from measurements at the five observation stations show no obvious changes. These long-term variations are consistent with those reported globally (Figure 2.2-5).

Variations are considered to stem mainly from changes in anthropogenic aerosols in the atmosphere, and to be partly attributed to changes in cloud cover and cloud characteristics (Wild, 2009). Norris and Wild (2009) quantitatively estimated the cause of the increase in global solar radiation observed in Japan from around 1990 to the beginning of the 2000s. According to their estimates, two thirds of the increase was due to reduced anthropogenic aerosols in the atmosphere and the other third was due to reduced cloud cover. These results imply that the presence of anthropogenic aerosols has a profound effect on solar radiation variations. Results produced by Kudo et al. (2012) indicated that the solar radiation increase was mainly caused by changes in the optical characteristics of aerosols due to changes in the aerosol composition of the atmosphere.

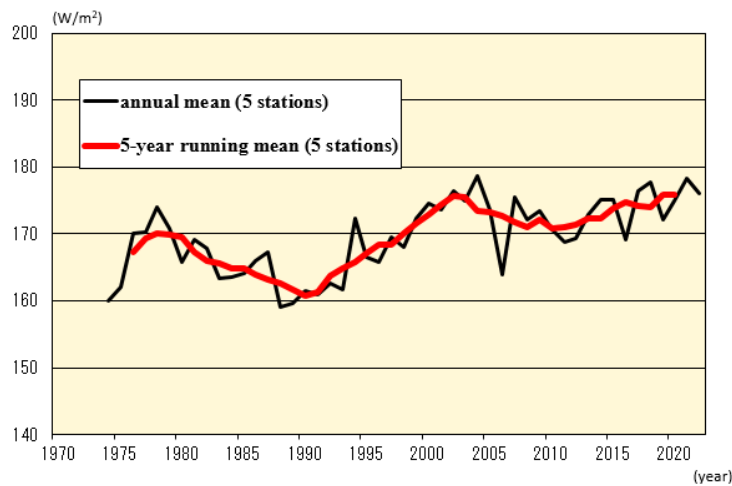


Figure 2.2-5 Time-series representations of annual (black line) and five-year-running (red line) means of global solar radiation at five stations in Japan (Abashiri, Tsukuba, Fukuoka, Ishigakijima and Minamitorishima)

Annual means are based only on monthly mean calculation from more 20 daily datasets. Before March 2010 (before February 2021 at Abashiri and before December 1987 at Tsukuba), observation was global pyranometer-based, while values have since been derived from the sum of direct and diffused pyranometer observations.

(2) Downward infrared radiation

Atmospheric concentrations of carbon dioxide and other greenhouse gases, which cause global warming, show increasing yearly trends. Observation of downward infrared radiation is effective for the evaluation of global warming because signals of global warming due to increased greenhouse gases are seen more clearly from increased downward infrared radiation than from increased surface temperatures. While general circulation

²¹ Global solar radiation is the total incident solar energy arriving on a horizontal plane from all directions in the sky, and is the sum of direct solar radiation and diffuse solar radiation (the incident solar energy, except from the direction of the sun, acting on the earth's surface after being scattered by the atmosphere and clouds from all directions in the sky). It is observed either with a pyranometer or as the sum of direct and diffused pyranometer observation results. Data from the latter method are used as much as possible in Figure 2-2.5.

model experiments suggest that two decades of downward infrared radiation monitoring are necessary to detect statistically significant increases with a confidence level of 95%, analysis of in situ observation data covering about a decade has shown an overall increase (Wild and Ohmura, 2004).

In Japan, downward infrared radiation has been monitored since the early 1990s at Tsukuba. Analysis of the data obtained shows an increasing trend at a rate of about 0.3 W/m^2 per year during the period from 1993 to 2022 (Figure 2.2-6). This is consistent with the trend seen in the results of analysis using data from 20 BSRN²² stations worldwide ($+0.3 \text{ W/m}^2$ per year during the period from 1992 to 2009) (WCRP, 2010).

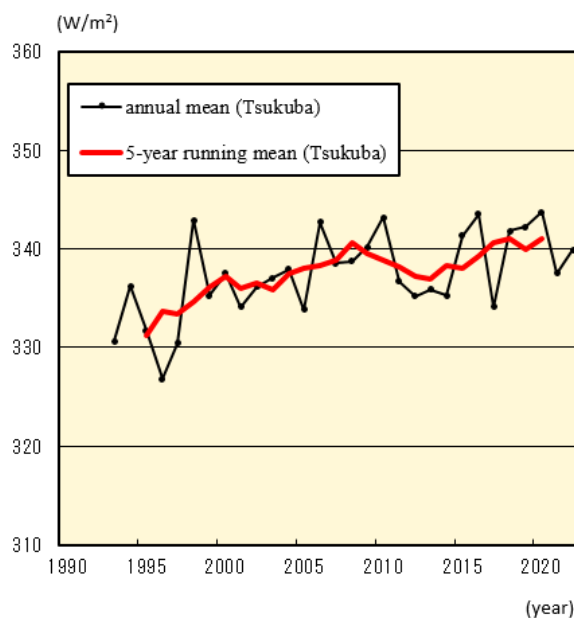


Figure 2.2-6 Time-series representations of annual (black line) and five-year-running (red line) means of downward infrared radiation at Tsukuba

²² The BSRN (Baseline Surface Radiation Network) is a global observation network for measuring high-precision surface radiation balance on an ongoing basis. JMA operates five BSRN stations in Japan (Abashiri, Tsukuba, Fukuoka, Ishigakijima and Minamitorishima) and one in Antarctica (Syowa Station).

2.3 Temperature²³

- The annual anomaly of the global average surface temperature in 2022 was +0.24°C, the 6th highest since 1891. On a longer time scale, it is virtually certain that the annual global average surface temperature has risen at a rate of 0.74°C per century.
- The annual anomaly of the average temperature over Japan was +0.60°C, the 4th highest since 1898. On a longer time scale, it is virtually certain that the annual average temperature over Japan has risen at a rate of 1.30°C per century.
- It is virtually certain that the annual number of days with maximum temperatures of 35 °C or higher ($T_{\max} \geq 35^{\circ}\text{C}$) and that with minimum temperatures of 25°C or higher ($T_{\min} \geq 25^{\circ}\text{C}$) have increased, while the annual number of days with minimum temperatures below 0°C ($T_{\min} < 0^{\circ}\text{C}$) has decreased.

2.3.1 Global surface temperature

The annual anomaly of the global average surface temperature in 2022 (i.e., the combined average of the near-surface air temperature over land and the SST) was +0.24°C above the 1991 – 2020 average. This was the 6th highest since 1891 (Figure 2.3-1). The years from 2014 to 2022 were the top-nine warmest on record in terms of global temperature. The global average temperature fluctuates on different time scales ranging from years to decades. On a longer time scale, it is virtually certain that the global average surface temperature has risen at a rate of 0.74°C per century²⁴ (statistically significant at a confidence level of 99%²⁵).

The surface temperature anomalies over the Northern Hemisphere and the Southern Hemisphere were +0.35°C (the 5th highest) and +0.11°C (the 7th highest) above the 1991 –2020 average, respectively (Figure 2.3-2). It is virtually certain that average surface temperatures over the Northern Hemisphere and the Southern Hemisphere have risen at rates of 0.78°C and 0.68°C per century, respectively (both statistically significant at a confidence level of 99%).

Linear temperature trends for 5° × 5° latitude/longitude grid boxes indicate that most areas of the world, especially in the high latitudes of the Northern Hemisphere, have experienced long-term warming (Figure 2.3-3). These long-term trends in annual average temperatures can be largely attributed to global warming caused by increased concentrations of greenhouse gases such as CO₂. On a shorter time scale, temperatures fluctuate due to the influence of natural climate dynamics over different time scales ranging from years to decades.

²³ Monthly, seasonal and annual estimates of mean temperatures averaged over the globe and Japan are published on JMA's website.

<https://www.data.jma.go.jp/cpdinfo/temp/index.html> (Japanese)

<https://www.data.jma.go.jp/tcc/tcc/products/gwp/gwp.html> (English)

²⁴IPCC AR6 (IPCC, 2021) reported that the global surface temperature from 2001 to 2020 was 0.99°C (with a very likely assessment range of 90 – 100%, or a 90% interval, of 0.84 – 1.10°C) higher than the period from 1850 to 1900. IPCC AR6 values and those in this report show no remarkable difference in rise on a long-term time scale but have been higher since the mid-1990s. Exact correspondence is not observed due to calculation differences and the statistical period examined.

²⁵ For evaluation and clarification of the significance statistics used here, see “Explanatory note on detection of statistical significance in long-term trends” at the end of the report.

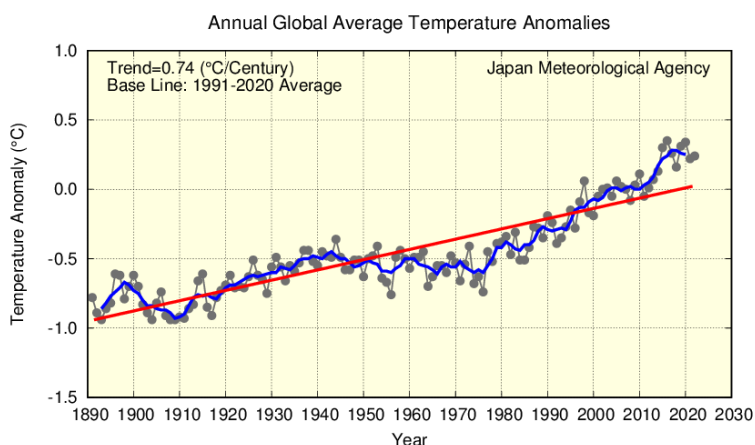


Figure 2.3-1 Annual anomalies in the global surface temperature (i.e., the combined average of the near-surface air temperature over land and the SST) from 1891 to 2022.

Anomalies are deviations from the baseline (i.e., the 1991 – 2020 average). The black dots indicate annual surface temperature anomalies, the blue line indicates the five-year running mean, and the red line indicates the long-term linear trend.

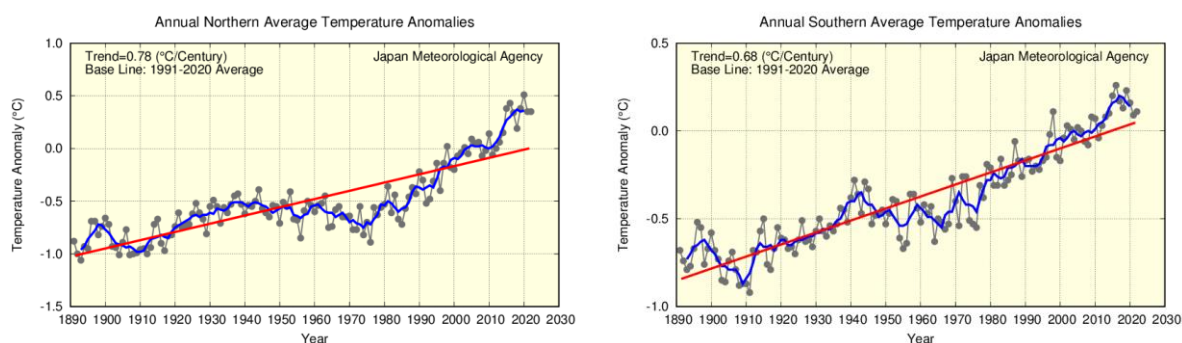


Figure 2.3-2 Annual anomalies in surface temperature (i.e., the combined average of the near-surface air temperature over land and the SST) from 1891 to 2022 for the Northern Hemisphere (left) and for the Southern Hemisphere (right).

Anomalies are deviations from the baseline (i.e., the 1991 – 2020 average). The thin black line with dots indicates surface temperature anomaly for each year. The blue line indicates the five-year running mean, and the red line indicates the long-term linear trend.

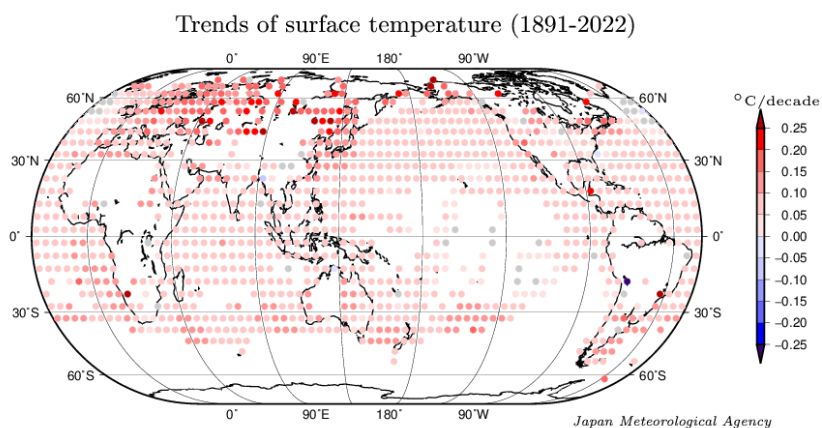


Figure 2.3-3 Linear temperature trends for 5° × 5° latitude/longitude grid boxes for the period of 1891 to 2022.

The grid boxes with gray circles have no statistically significant trend (not statistically significant at a confidence level of 90%). Blank areas indicate those with insufficient data to analyze long-term trends.

2.3.2 Surface temperature over Japan

Long-term changes in the surface temperature over Japan are analyzed using observational records dating back to 1898. Table 2.3-1 lists the meteorological stations whose data are used to derive annual mean surface temperatures.

Table 2.3-1 Observation stations whose data are used to calculate surface temperature anomalies over Japan.

Miyazaki and Iida were relocated in May 2000 and May 2002, respectively, and their temperatures have been adjusted to eliminate the influence of the relocation.

Element	Observation stations
Temperature (15 stations)	Abashiri, Nemuro, Suttsu, Yamagata, Ishinomaki, Fushiki, Iida, Choshi, Sakai, Hamada, Hikone, Tadotsu, Miyazaki, Naze, Ishigakijima

The mean surface temperature in Japan for 2022 is estimated to have been + 0.60°C above the 1991 – 2020 average, which is the 4th highest since 1898 (Figure 2.3-4). The surface temperature fluctuates on different time scales ranging from years to decades. On a longer time scale, it is virtually certain that the annual mean surface temperature over Japan has risen at a rate of 1.30°C per century (statistically significant at a confidence level of 99%). Similarly, it is virtually certain that the seasonal mean temperatures for winter, spring, summer and autumn have risen at rates of about 1.19, 1.56, 1.19 and 1.31°C per century, respectively (all statistically significant at a confidence level of 99%).

It is noticeable from Figure 2.3-4 that the annual mean temperature remained relatively low before the 1940s, started to rise and reached a local peak around 1960, entered a cooler era through to the mid-1980s and then began to show a rapid warming trend in the late 1980s. The warmest years on record have all been observed since the 1990s.

The high temperatures seen in recent years have been influenced by natural variability over time scales ranging from years to decades, as well as by global warming resulting from human factors such as increased concentrations of CO₂ and other greenhouse gases.

Relatively high monthly average temperatures were also observed in 2022 due to northward shifting of the westerly jet stream from its normal position between spring and autumn and a stronger-than-normal North Pacific Subtropical High over the seas south of Japan in summer (Chapter 1).

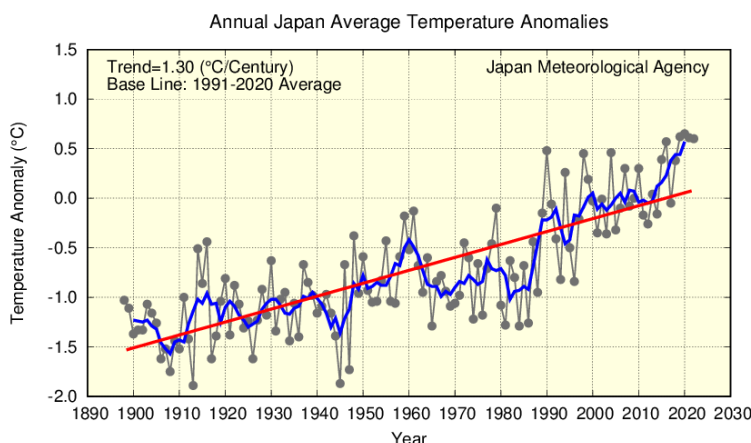


Figure 2.3-4 Annual surface temperature anomalies from 1898 to 2022 in Japan.

Anomalies are deviations from the baseline (i.e., the 1991 – 2020 average). The thin black line indicates the surface temperature anomaly for each year. The blue line indicates the five-year running mean, and the red line indicates the long-term linear trend.

2.3.3 Long-term trends of extreme temperature events in Japan

This section describes long-term trends of extremely high/low-temperature events in Japan, as derived from analysis of temperature records from the 15 observation stations. Though monthly mean temperatures of the stations in Miyazaki and Iida have been adjusted to eliminate the influence of their relocation, records from these two stations are not used for analysis of daily temperatures due to the difficulty of adjustment in regard to the relocation.

(1) Long-term trends of monthly extreme temperatures

It is virtually certain that the frequency of extremely high monthly temperatures has increased during the period from 1901 to 2022, while that of extremely low monthly temperatures has decreased (Figure 2.3-5). The frequency of extremely high monthly temperatures has largely increased since about 1990.

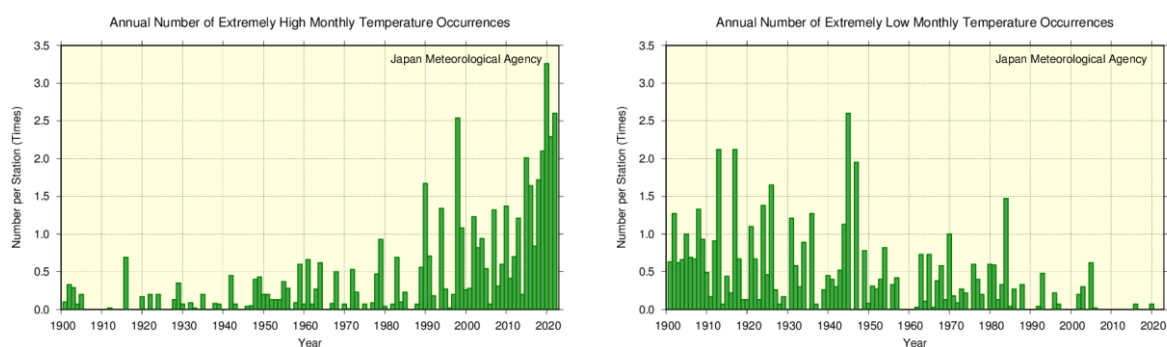


Figure 2.3-5 Annual number of extremely high/low monthly mean temperature occurrences from 1901 to 2022.

The graphs show the annual number of occurrences of the highest/lowest first-to-forth values for each month. The green bars indicate annual occurrences of extremely high/low monthly mean temperatures divided by the total number of monthly observation data sets available for the year (i.e., the average occurrence per station).

(2) Annual number of days with maximum temperatures of $\geq 30^{\circ}\text{C}$ and $\geq 35^{\circ}\text{C}$

The annual number of days with maximum temperatures (T_{\max}) of $\geq 30^{\circ}\text{C}$ and $T_{\max} \geq 35^{\circ}\text{C}$ is virtually certain to have increased during the period from 1910 to 2022 (both statistically significant at a confidence level of 99%) (Figure 2.3-6). Especially, the annual number of days with $T_{\max} \geq 35^{\circ}\text{C}$ has largely increased since about mid-1990s.

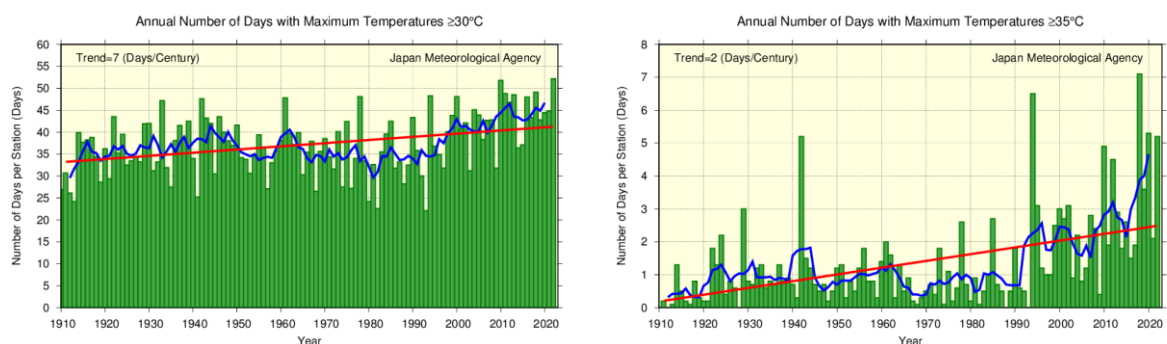


Figure 2.3-6 Annual number of days with maximum temperatures of $\geq 30^{\circ}\text{C}$ and $\geq 35^{\circ}\text{C}$ from 1910 to 2022

The green bars indicate the annual number of days per station for each year. The blue line indicates the five-year running mean, and the straight red line indicates the long-term linear trend.

(3) Annual number of days with minimum temperatures of $< 0^{\circ}\text{C}$ and $\geq 25^{\circ}\text{C}$

It is virtually certain that the annual number of days with minimum temperatures²⁶ (T_{\min}) of $< 0^{\circ}\text{C}$ has decreased, while the annual number of days with $T_{\min} \geq 25^{\circ}\text{C}$ has increased during the period from 1910 to 2022 (both statistically significant at a confidence level of 99%) (Figure 2.3-7).

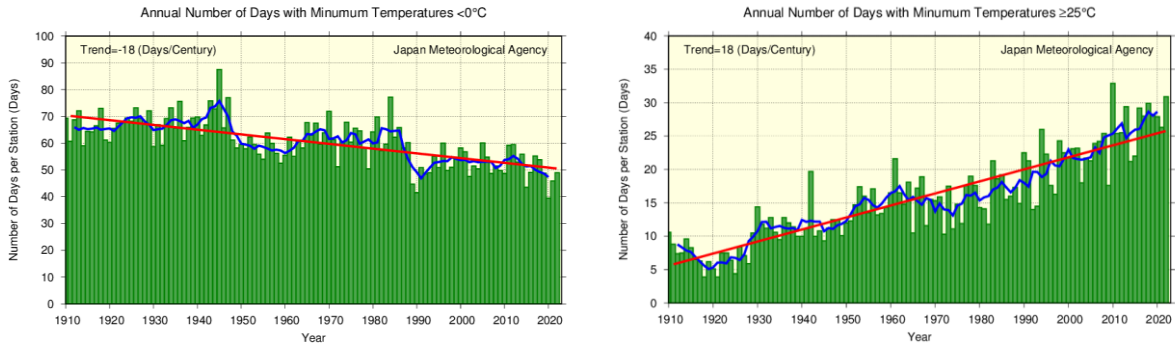


Figure 2.3-7 Annual number of days with minimum temperatures of $< 0^{\circ}\text{C}$ and $\geq 25^{\circ}\text{C}$ from 1910 to 2022
As per Figure 2.3-6.

2.3.4 *Urban heat island effect at urban stations in Japan*

The long-term trends of annual average temperatures are more pronounced for urban observation stations whose data are homogeneous over a long period (Sapporo, Sendai, Tokyo, Yokohama, Niigata, Nagoya, Kyoto, Osaka, Hiroshima, Fukuoka, Kagoshima) than for the average of the 15 rural observation stations (Table 2.3-2 and Figure 2.3-8). Although values varied by location, the rates of increase in annual mean temperatures at urban stations (by way of example) were around $0.4\text{--}1.7^{\circ}\text{C}$ per century higher than the 15 station averages.

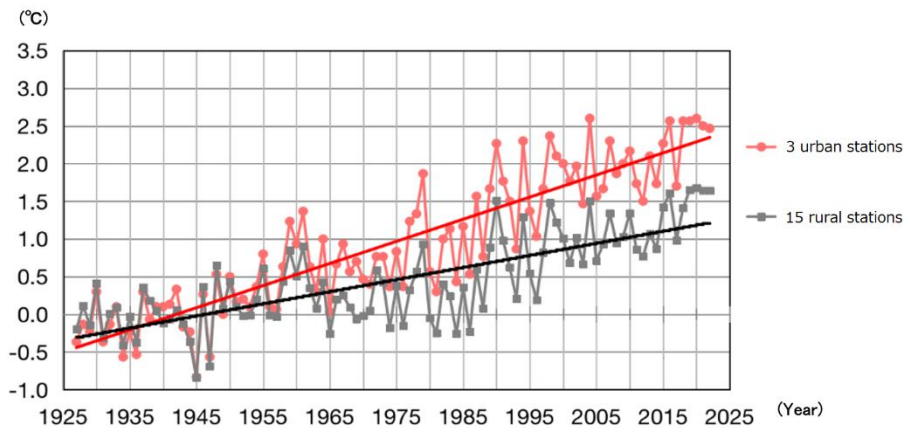


Figure 2.3-8 Annual temperature anomalies averaged over 3 urban stations (Tokyo, Nagoya and Osaka) and 15 rural stations in Japan from 1927 to 2022.

Anomalies are deviations from the baseline (i.e., the 1927 – 1956 average). Values averaged between 1927 and 1956 for respective stations all equal zero.

²⁶ In JMA statistics, daily maximum and minimum temperatures were observed at the daily boundary of 9:00 for the period 1953 – 1963. Systematic differences caused by a change in the daily boundary time are discussed in Fujibe (1999) and elsewhere. Estimation from monthly differences in daily minimum temperatures between the 9:00 and 24:00 daily boundaries based on observation for the period 2009 – 2020 indicates that the daily minimum temperature can be expected to be about 0.4 to 0.6°C higher than current values depending on the location and month. The number of days with $T_{\min} < 0^{\circ}\text{C}$ is estimated to be about 4.6 higher and that with $T_{\min} \geq 25^{\circ}\text{C}$ about 0.5 lower than the values for each year in the graph (the average number of days for each of 13 locations nationwide) during the period 1953 – 1963.

Table 2.3-2 Long-term trends of annual and seasonal average temperatures at urban stations in Japan.

These figures are based on data from 1927 to 2022. The trend of the 15 rural station averages (Table 2.3-1) is also listed. Values shown in italics are not statistically significant at a confidence level of 90%. For stations with asterisks (5 urban stations, and Iida and Miyazaki among the 15 rural stations), trends are calculated after adjustment to eliminate the influence of relocation.

Station	Long-term temperature trend (°C/century)														
	Average					Daily maximum					Daily minimum				
	Ann	Win	Spr	Sum	Aut	Ann	Win	Spr	Sum	Aut	Ann	Win	Spr	Sum	Aut
Sapporo	2.7	3.2	3.1	1.9	2.6	1.2	1.5	1.9	0.7	0.7	4.4	5.4	4.8	3.4	4.2
Sendai	2.5	2.9	3.0	1.6	2.6	1.5	1.7	2.0	1.1	1.1	3.2	3.6	3.8	2.1	3.3
Tokyo*	3.3	4.2	3.4	2.2	3.4	1.9	2.2	2.3	1.5	1.9	4.4	5.8	4.6	3.0	4.4
Yokohama	2.8	3.5	3.2	1.9	2.8	2.6	2.8	3.1	2.0	2.5	3.5	4.5	3.8	2.3	3.5
Niigata*	2.1	2.3	2.7	1.4	2.0	2.1	2.7	2.9	1.0	1.9	2.2	2.3	2.7	1.9	2.0
Nagoya	2.9	3.0	3.2	2.3	3.2	1.5	1.6	1.9	1.1	1.5	3.9	3.8	4.4	3.2	4.3
Kyoto	2.7	2.6	3.1	2.3	2.8	1.3	1.0	1.9	1.2	1.1	3.8	3.7	4.1	3.3	4.0
Osaka*	2.6	2.6	2.8	2.0	3.0	2.2	2.2	2.5	2.0	2.2	3.4	3.1	3.5	3.2	3.9
Hiroshima*	2.0	1.7	2.4	1.5	2.5	1.1	0.8	1.8	1.1	0.7	3.1	2.8	3.4	2.6	3.9
Fukuoka	3.1	2.9	3.5	2.3	3.8	1.9	1.8	2.3	1.5	1.8	4.9	4.3	5.8	3.7	6.0
Kagoshima*	2.5	2.6	2.9	2.0	2.9	1.4	1.3	1.8	1.1	1.5	3.9	3.6	4.4	3.2	4.6
15 station averages*	1.6	1.6	2.0	1.2	1.6	1.3	1.3	1.8	0.9	1.0	1.9	1.9	2.2	1.7	1.9

As it can be assumed that the long-term trends averaged over the 15 rural stations reflect large-scale climate change, the differences in the long-term trends of urban stations from the average of the 15 stations largely represent the influence of urbanization.

Detailed observation reveals that the long-term trends²⁷ are more significant in winter, spring and autumn than in summer and more pronounced for minimum temperatures than for maximum temperatures at every urban observation station.

Records from urban stations whose data are not affected by relocation are used to determine long-term trends for the annual number of days with minimum temperatures of $< 0^{\circ}\text{C}$ and $\geq 25^{\circ}\text{C}$ and maximum temperatures of $\geq 30^{\circ}\text{C}$ and $\geq 35^{\circ}\text{C}$. The number of days with $T_{\min} < 0^{\circ}\text{C}$ is very likely to have decreased with statistical significance at all urban stations, and the number with $T_{\min} \geq 25^{\circ}\text{C}$, $T_{\max} \geq 30^{\circ}\text{C}$ and $T_{\max} \geq 35^{\circ}\text{C}$ is very likely to have increased with statistical significance at most stations except Sapporo (Table 2.3-3).

²⁷The effect of the change in the daily boundary time for the period 1953 – 1963 (discussed in the previous footnote) is estimated to be negligible in the long-term trend of daily mean minimum temperatures at the 15 sites, as an example.

Table 2.3-3 Long-term trends for the annual number of days with minimum temperatures of $< 0^{\circ}\text{C}$ and $\geq 25^{\circ}\text{C}$ and maximum temperatures of $\geq 30^{\circ}\text{C}$ and $\geq 35^{\circ}\text{C}$.

These figures are based on data from 1927 to 2022. The trend of the 13 rural station averages (Table 2.3-1 excluding Iida and Miyazaki) is also listed. Values shown in italics are not statistically significant at a confidence level of 90%.

Station	Annual number of days			
	Trend (days/century)			
	$T_{\min} < 0^{\circ}\text{C}$	$T_{\min} \geq 25^{\circ}\text{C}$	$T_{\max} \geq 30^{\circ}\text{C}$	$T_{\max} \geq 35^{\circ}\text{C}$
Sapporo	-46	<i>0</i>	<i>3</i>	<i>0</i>
Sendai	-58	5	11	1
Yokohama	-58	31	22	3
Nagoya	-67	38	14	10
Kyoto	-70	37	15	14
Fukuoka	-47	48	14	12
13 station averages	-21	18	7	2

2.4 Precipitation²⁸

- The annual anomaly of global precipitation (for land areas only) in 2022 was +47 mm.
- The annual anomaly of precipitation in 2022 was –71.5 mm in Japan. Annual precipitation over Japan shows no discernible long-term trend.
- The annual number of days with daily and hourly extreme precipitation has increased in Japan, while that with wet days has decreased.

2.4.1 Global precipitation over land

Annual precipitation (for land areas only) in 2022 was +47 mm (the 2nd heaviest) above the 1991 – 2020 average, and has fluctuated periodically since 1901. In the Northern Hemisphere, records show large amounts of rainfall in the 1950s and after the mid-2000s (Figure 2.4-1). No long-term trends are observed because there are few observation data from the early statistical period and the margin of error is relatively large.

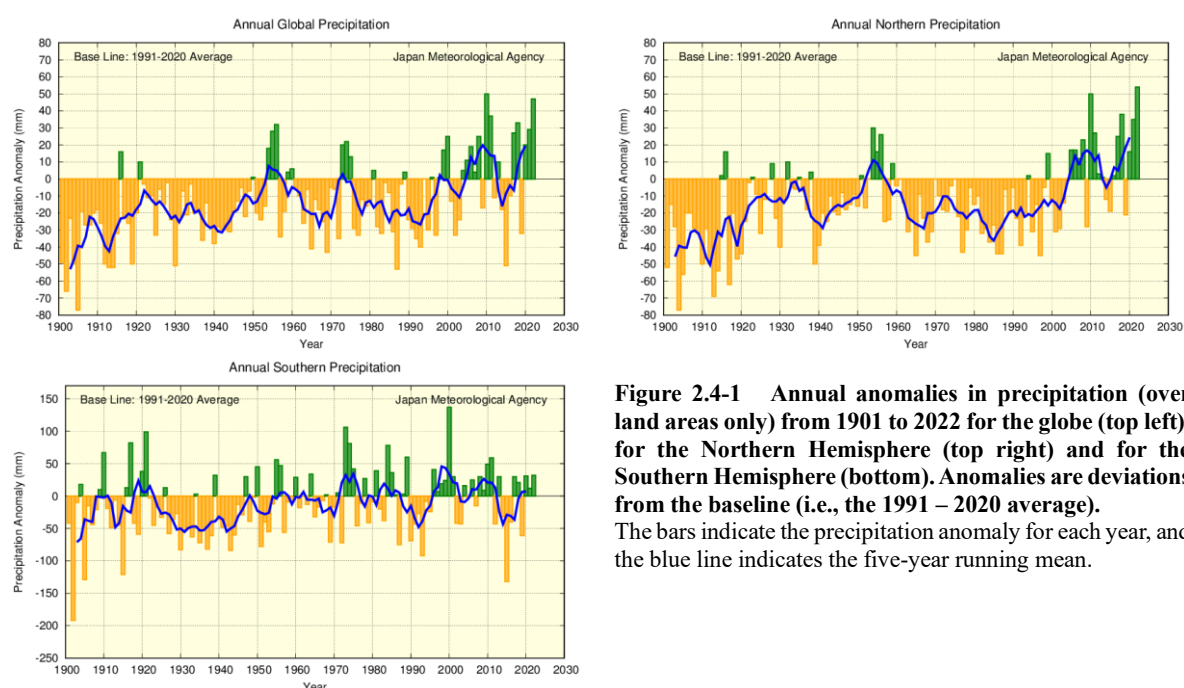


Figure 2.4-1 Annual anomalies in precipitation (over land areas only) from 1901 to 2022 for the globe (top left), for the Northern Hemisphere (top right) and for the Southern Hemisphere (bottom). Anomalies are deviations from the baseline (i.e., the 1991 – 2020 average). The bars indicate the precipitation anomaly for each year, and the blue line indicates the five-year running mean.

2.4.2 Precipitation over Japan

This section describes long-term trends in precipitation over Japan as derived from analysis of precipitation records from 51 observation stations (Table 2.4-1).

Annual precipitation in 2022 was –71.5 mm (the 43rd lightest since 1898) above the 1991 – 2020 average. Japan experienced relatively large amounts of rainfall until the mid-1920s, around the 1950s and after the 2010s. The annual figure exhibits greater variability for the period from the 1970s to the 2000s (Figure 2.4-2).

²⁸ Data on annual precipitation around the world and in Japan are published on JMA's website.

Table 2.4-1 List of 51 observation stations whose data are used to calculate precipitation anomalies and long-term trends in Japan.

Element	Observation stations
Precipitation (51 stations)	Asahikawa, Abashiri, Sapporo, Obihiro, Nemuro, Suttsu, Akita, Miyako, Yamagata, Ishinomaki, Fukushima, Fushiki, Nagano, Utsunomiya, Fukui, Takayama, Matsumoto, Maebashi, Kumagaya, Mito, Tsuruga, Gifu, Nagoya, Iida, Kofu, Tsu, Hamamatsu, Tokyo, Yokohama, Sakai, Hamada, Kyoto, Hikone, Shimonoseki, Kure, Kobe, Osaka, Wakayama, Fukuoka, Oita, Nagasaki, Kumamoto, Kagoshima, Miyazaki, Matsuyama, Tadotsu, Kochi, Tokushima, Naze, Ishigakijima, Naha

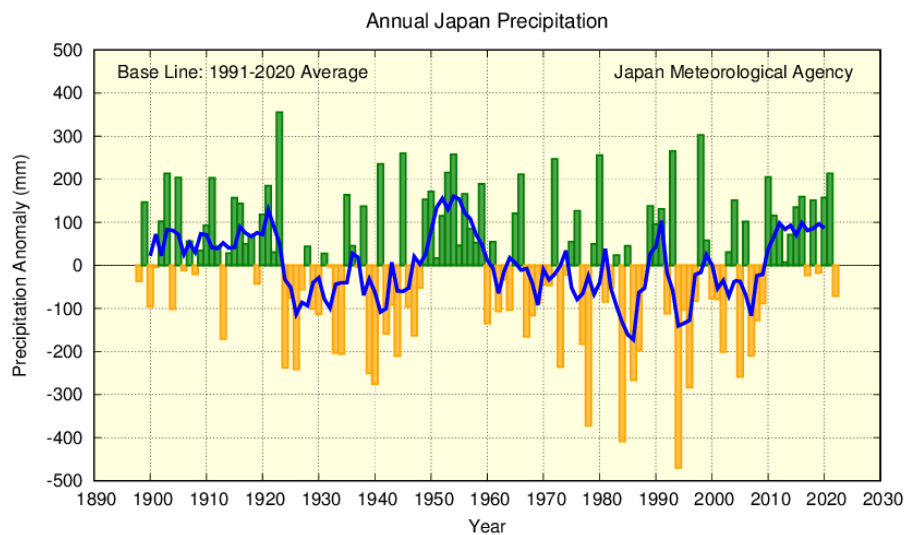


Figure 2.4-2 Annual anomalies in precipitation from 1898 to 2022 in Japan. Anomalies are deviations from the baseline (i.e., the 1991 – 2020 average).

The bars indicate the precipitation anomaly for each year, and the blue line indicates the five-year running mean.

2.4.3 Long-term trends of extreme precipitation events in Japan

(1) Extremely wet/dry months²⁹

This part describes long-term trends in frequencies of extremely wet/dry months and heavy daily precipitation events in Japan based on analysis of precipitation data from 51 observation stations.

It is virtually certain that the frequency of extremely dry months increased (Figure 2.4-3 left). There has been no discernible trend in the frequency of extremely wet months (Figure 2.4-3 right).

²⁹ Here, judgment of extremely heavy/light precipitation is based on the fourth–highest/lowest monthly values on record over about 120-year period from 1901. The frequency of occurrence of the highest/lowest to the fourth–highest/lowest values over this period is once approximately every 30 years, which is close to JMA’s definition of extreme climate events as those occurring once every 30 years or longer (See the Glossary for terms relating to Extreme climate event).

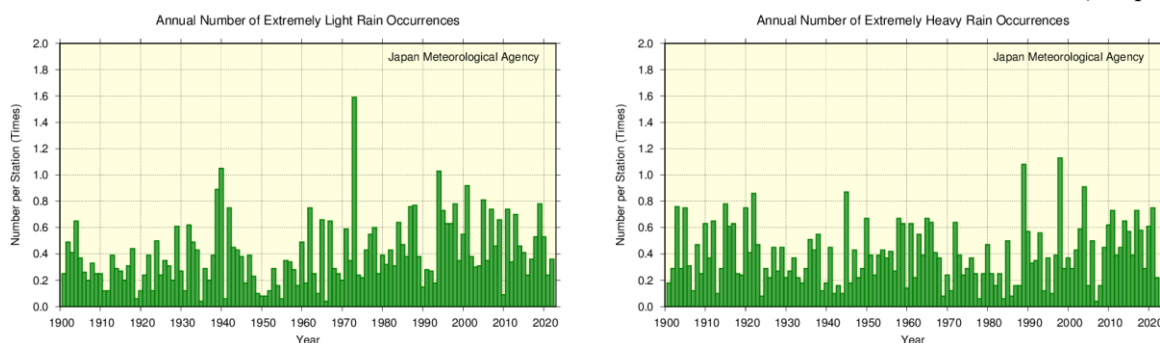


Figure 2.4-3 Annual number of extremely wet/dry months from 1901 to 2022.

The graphs show the annual number of occurrences of the first-to-forth heaviest/lightest precipitation values for each month. The green bars indicate annual occurrences of extremely heavy/light monthly precipitation divided by the total number of monthly observation data sets available for the year (i.e., the average occurrence per station).

(2) Annual number of days with precipitation of ≥ 100 mm, ≥ 200 mm and ≥ 1.0 mm

The annual number of days with precipitation of ≥ 100 mm and ≥ 200 mm are virtually certain to have increased during the period from 1901 to 2022 (both statistically significant at a confidence level of 99%) (Figure 2.4-4). The annual number of days with precipitation of ≥ 1.0 mm (Figure 2.4-5) is virtually certain to have decreased over the same period (statistically significant at a confidence level of 99%). These results suggest decrease in the annual number of wet days including light precipitation and in contrast, an increase in extremely wet days.

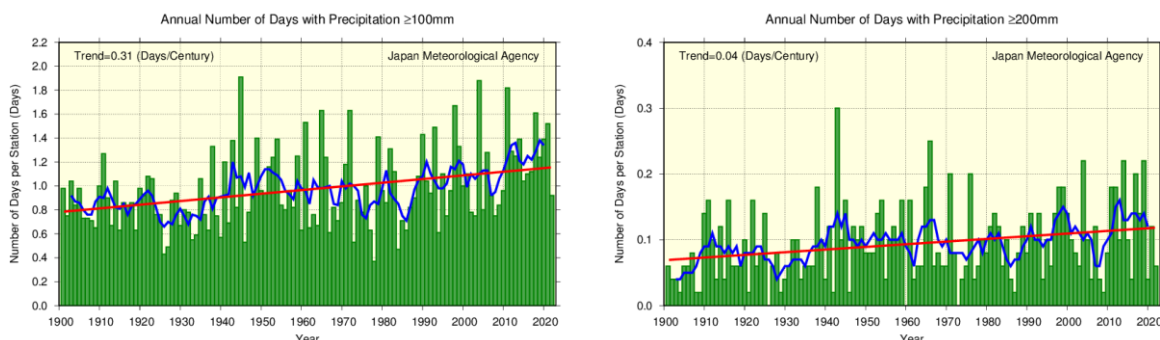


Figure 2.4-4 Annual number of days with precipitation ≥ 100 mm and ≥ 200 mm from 1901 to 2022.

The green bars indicate the annual number of days per station for each year. The blue line indicates the five-year running mean, and the straight red line indicates the long-term linear trend.

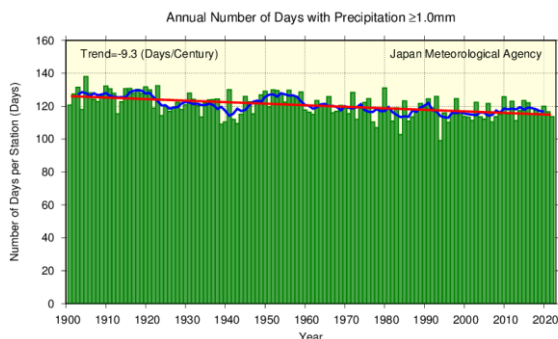


Figure 2.4-5 Annual number of days with precipitation of ≥ 1.0 mm from 1901 to 2022.

As per figure 2.4-4.

(3) Heavy rainfall frequency based on AMeDAS data

JMA operationally observes precipitation at about 1,300 unmanned regional meteorological observation stations all over Japan (collectively known as the Automated Meteorological Data Acquisition System, or AMeDAS). Observation was started in the latter part of the 1970s at many points, and observation data covering the approximately 50-year period through to 2022 are available³⁰. Although the period covered by AMeDAS observation records is shorter than that of Local Meteorological Observatories or Weather Stations (which have observation records for the past 120 years or so), there are around eight times as many AMeDAS stations as Local Meteorological Observatories and Weather Stations combined. Hence, AMeDAS is better equipped to capture heavy precipitation events that take place on a limited spatial scale.

It is virtually certain that annual numbers of heavy rainfall events have increased, also with greater intensity and higher frequency. In addition, the frequency of heavier rainfall (e.g., ≥ 80 mm per hour, ≥ 150 mm per 3 hours and ≥ 300 mm per day) has almost doubled since around 1980 (Table 2.4-2, Figure 2.4-6).

These increasing trends can be attributed to global warming. As the frequency of extreme precipitation events is low and the period covered by observation records is still relatively short, the addition of future observations to the data series is expected to increase the reliability of statistical trend detection.

³⁰ The number of AMeDAS station was about 800 in 1976, and had gradually increased to about 1,300 now. To account for these numerical differences, the annual number of precipitation events needs to be converted to a per-1,300-station basis. Data from wireless robot precipitation observation stations previously deployed in mountainous areas are also excluded.

Table 2.4-2 Changes in annual numbers of heavy rainfall events from 1976 to 2022 on AMeDAS data

Element	Trend	Frequency ratio (2013 – 2022 average vs. 1976 – 1985 average)
≥ 50 mm per hour	Virtually certain to have increased (statistically significant at a confidence level of 99%)	Approx. x 1.5 (Approx. 226 -> Approx. 328)
≥ 80 mm per hour	Virtually certain to have increased (statistically significant at a confidence level of 99%)	Approx. x 1.8 (Approx. 14 -> Approx. 25)
≥ 100 mm per hour	Extremely likely to have increased (statistically significant at a confidence level of 95%)	Approx. x 2 (Approx. 2.2 -> Approx. 4.4)
≥ 100 mm per 3 hours	Virtually certain to have increased (statistically significant at a confidence level of 99%)	Approx. x 1.6 (Approx. 155 -> Approx. 254)
≥ 150 mm per 3 hours	Virtually certain to have increased (statistically significant at a confidence level of 99%)	Approx. x 1.8 (Approx. 19 -> Approx. 34)
≥ 200 mm per 3 hours	Virtually certain to have increased (statistically significant at a confidence level of 99%)	Approx. x 2.1 (Approx. 2.8 -> Approx. 6.0)
≥ 200 mm per day	Extremely likely to have increased (statistically significant at a confidence level of 95%)	Approx. x 1.5 (Approx. 160 -> Approx. 239)
≥ 300 mm per day	Extremely likely to have increased (statistically significant at a confidence level of 95%)	Approx. x 1.8 (Approx. 28 -> Approx. 51)
≥ 400 mm per day	Extremely likely to have increased (statistically significant at a confidence level of 95%)	Approx. x 1.9 (Approx. 6.4 -> Approx. 12)

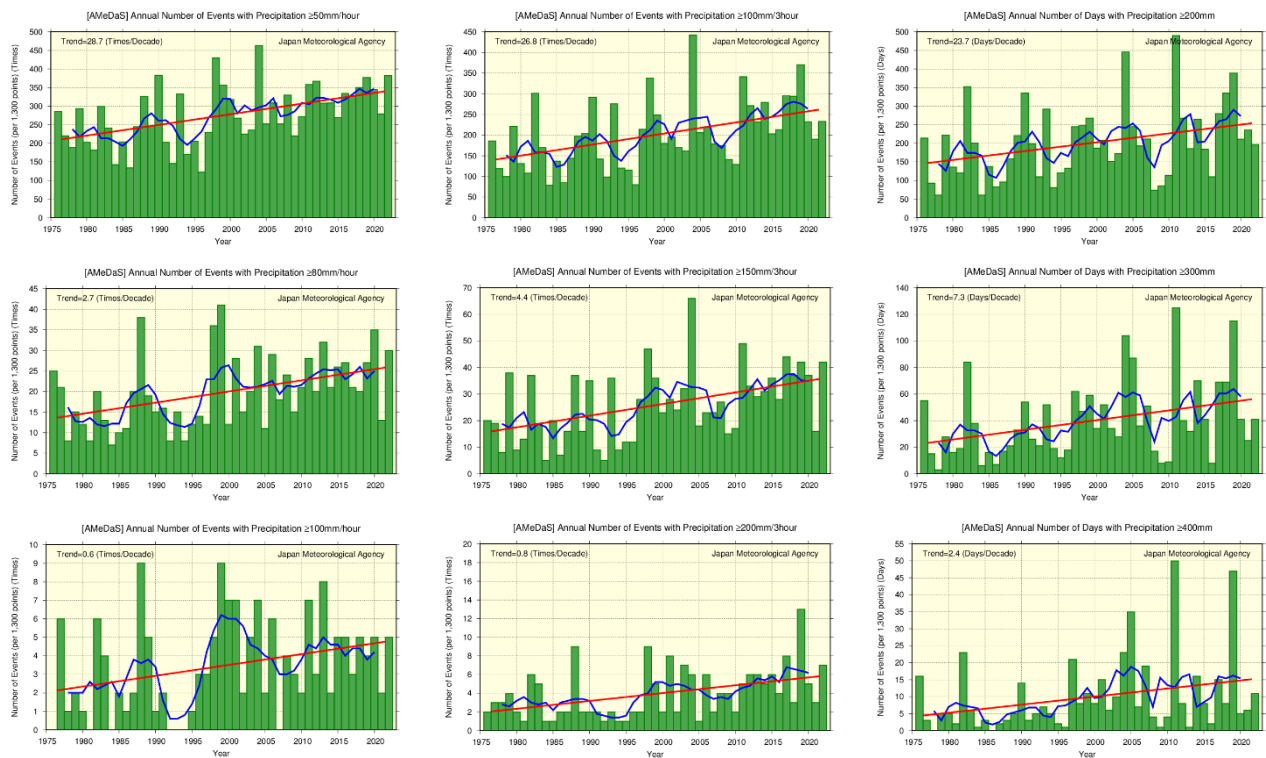


Figure 2.4-6 Annual numbers of heavy rainfall events from 1976 to 2022

Left: Events with precipitation of ≥ 50 mm (top), ≥ 80 mm (center) and ≥ 100 mm (bottom) per hour

Center: Events with precipitation of ≥ 100 mm (top), ≥ 150 mm (center) and ≥ 200 mm (bottom) per 3 hours

Right: Days with precipitation of ≥ 200 mm (top), ≥ 300 mm (center) and ≥ 400 mm (bottom)

The green bars indicate the annual number of events per 1,300 AMeDAS stations for each year. The blue line indicates the five-year running mean, and the straight red line indicates the long-term liner trend.

(4) Heavy rainfall intensity based on AMeDAS data

Changes in the intensity of annual maximum 24-, 48- and 72-hour precipitation over Japan were analyzed using data from 637 AMeDAS stations where ongoing observation was conducted from 1976 to 2022. Annual data are averages of ratios against the baseline (the 1991 – 2020 average).

It is extremely likely that annual maximum 24-, 48- and 72-hour precipitation increased at rates of 3.2%, 3.5% and 3.3% per decade (each statistically significant at a confidence level of 95%), respectively (Figure 2.4-7).

As for the relation between temperature and water vapor amounts, it is widely accepted that saturated water vapor amounts increase by approximately 7% for each 1°C increment in air temperature. The trend of increased intensity in extreme precipitation events in Japan may be attributable to a long-term increasing trend of the amount of water vapor in the atmosphere associated with a background of long-term temperature rising due to global warming. As per Section (3), the addition of future observations to the data series is expected to increase the reliability of statistical trend determination.

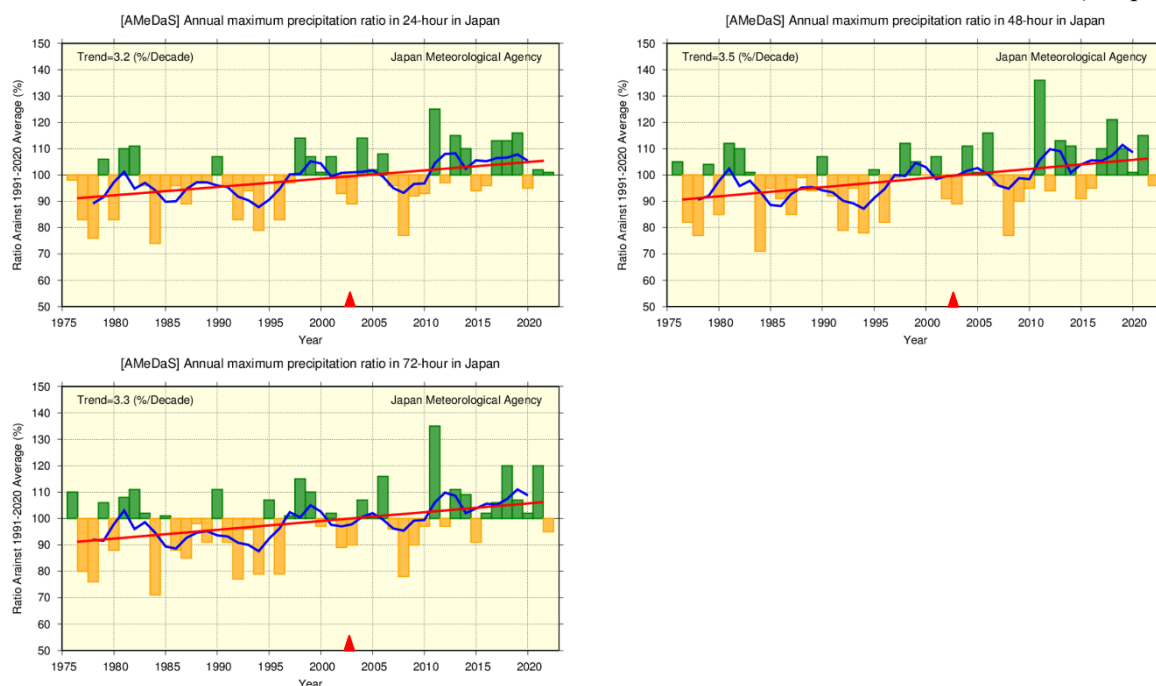


Figure 2.4-7 Annual maximum precipitation ratios (%) for 24-hour (top left) , 48-hour (top right) and 72-hour (bottom) periods over Japan for the period from 1976 to 2022.

Annual averages for each year are presented as ratios against the baseline (i.e., the 1991 – 2020 average). The green and yellow bars indicate the annual maximum precipitation ratios for each year based on 637 AMeDAS stations where ongoing observation was conducted from 1976. The blue line indicates the five-year running means, and the straight red line indicates the long-term linear trend. Red triangles (▲) indicate the change in observational periodicity for hourly precipitation from every hour to every 10 minutes in 2003³¹.

³¹As of 1 Jan. 2003, annual maximum precipitation is determined from 10-minute data as opposed to the previous hourly data. This creates a systematic difference ▲ (e.g., annual maximum daily precipitation ≥ 50 mm tends to average 8 mm more than before.)

2.5 Snow depth and snow cover

- It is extremely likely that a decreasing trend is observed in the interannual variability of the total snow cover extent in the Northern Hemisphere for January, June and the period from September to December and in Eurasia for the period from January to March, June and the period from September to December.
- In winter 2021/2022, there were more days of snow cover than normal over southwestern China, and fewer over central Europe and Central Asia.
- Snow depth on the Sea of Japan side is extremely likely to have decreased.

2.5.1 Snow cover in the Northern Hemisphere

JMA monitors snow-cover variations in the Northern Hemisphere using analysis data from satellite observations³² based on its own algorithm. The average seasonal migration of snow cover in the Northern Hemisphere normally peaks around January - February and decreases in spring.

In the Northern Hemisphere (north of 30°N), it is extremely likely (statistically significant at a confidence level of 95%) that a decreasing trend is observed in the interannual variability of the total snow cover extent over the 35-year period from 1988 to 2022 for January, June and the period from September to December, while no discernible trend is seen for the period from February to May (Figure 2.5-2 (a) and (c)). In Eurasia (north of 30°N from 0° to 180°E), it is extremely likely (statistically significant at a confidence level of 95%) that a decreasing trend is observed in the interannual variability of the total snow cover for the period from January to March, June and the period from September to December, while no discernible trend is seen for the period from April to May and the period from July to August (Figure 2.5-2 (b) and (d)). In winter (December to February) 2021/2022, there were more days of snow cover than normal over southwestern China, and fewer over central Europe and Central Asia (Figure 2.5-2 (e)). In November 2022, there were more days of snow cover in the northwestern USA, and fewer over Central Siberia and eastern Canada (Figure 2.5-2 (f)).

The albedo of snow-covered ground (i.e., the ratio of solar radiation reflected by the surface) is higher than that of snow-free ground. The variability of snow cover has an impact on the earth's surface energy budget and radiation balance, and therefore on the climate. In addition, snow absorbs heat from its surroundings and melts, thereby providing soil moisture and related effects on the climate system. The variability of atmospheric circulation and oceanographic conditions affects the amount of snow cover, which exhibits a close and mutual association with climatic conditions. Snow-cover variations in Eurasia and other parts of the Northern Hemisphere may affect climate conditions in Japan, but the mechanisms behind such a potential influence remain unclear. The accumulation of future observation data in addition to the current body of information and the implementation of related research are expected to increase the reliability of statistical work to identify trends of snow cover extent and help to elucidate how snow-cover variations affect climate conditions.

³² The Defense Meteorological Satellite Program (DMSP) polar-orbiting satellites of the USA, equipped with the Special Sensor Microwave/Imager (SSM/I) and the Special Sensor Microwave Imager Sounder (SSMIS), and the Japan Aerospace Exploration Agency (JAXA) Global Change Observation Mission – Water (GCOM-W) satellite, equipped with the Advanced Microwave Scanning Radiometer 2 (AMSR2)

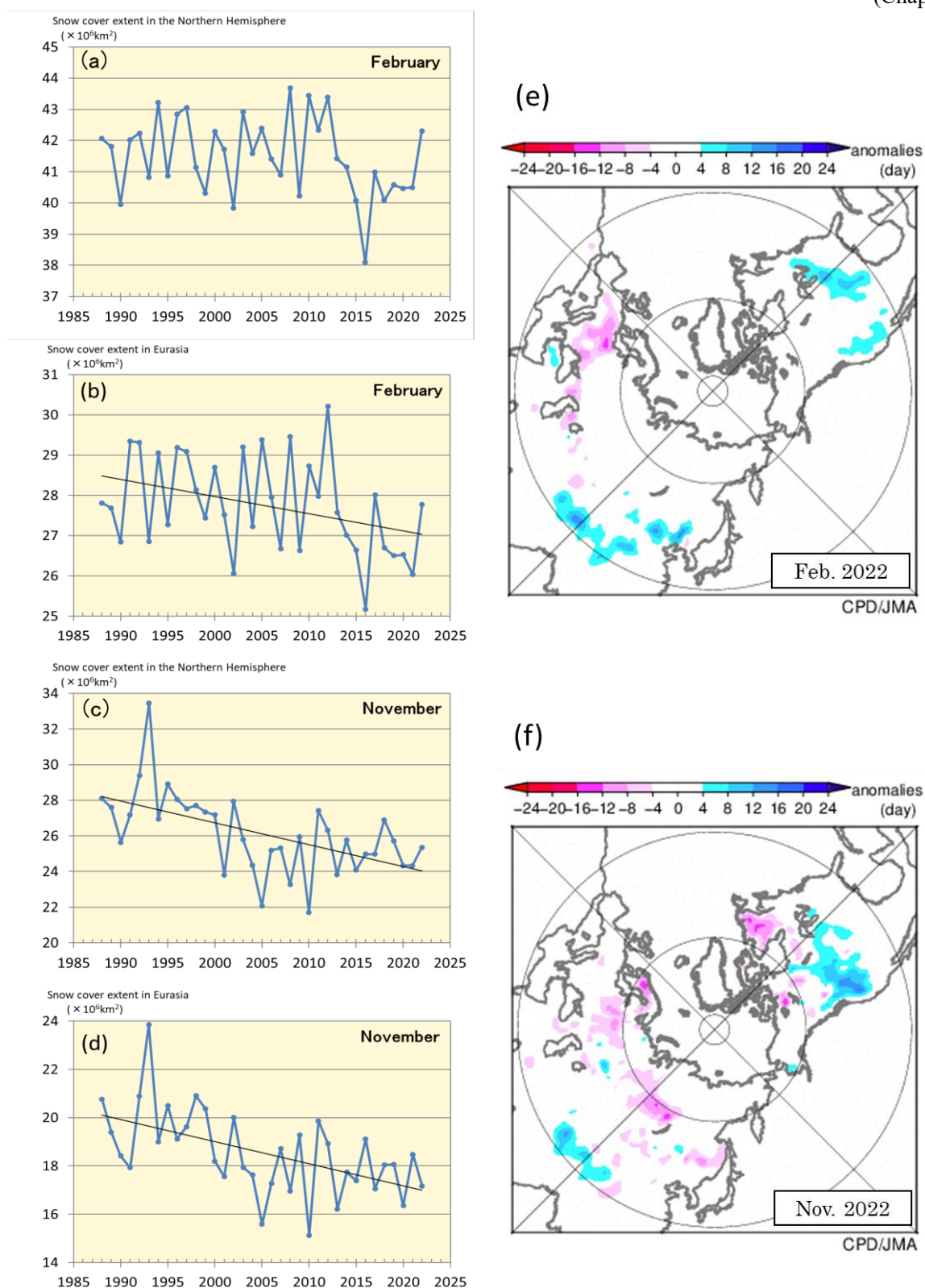


Figure 2.5-2 Interannual variations in the total area of monthly snow cover (km^2) in the Northern Hemisphere (north of 30°N) for (a) February and (c) November and in Eurasia (north of 30°N , from 0° to 180°E) for (b) February and (d) November from 1988 to 2022, and anomalies in the number of days with snow cover for (e) February and (f) November in 2022

(a) - (d): The blue lines indicate the total snow cover area for each year, and the black lines show linear trends (statistically significant at a confidence level of 95%).

(e) - (f): Blue (red) shading indicates more (fewer) days of snow cover.

The base period for the normal is 1991 – 2020.

2.5.2 Snow depth and Snowfall in Japan

(1) Annual maximum snow depth

Long-term trends in the annual maximum snow depth (represented in terms of a ratio against the 1991 – 2020 average) in Japan since 1962³³ are analyzed using observational records from stations located on the Sea of Japan coast (Table 2.5-1).

Table 2.5-1 Observation stations whose data are used to calculate snow depth ratios in Japan.

Region	Observation stations
Sea of Japan side of northern Japan	Wakkanai, Rumoi, Asahikawa, Sapporo, Iwamizawa, Suttsu, Esashi, Kutchan, Wakamatsu, Aomori, Akita, Yamagata
Sea of Japan side of eastern Japan	Wajima, Aikawa, Niigata, Toyama, Takada, Fukui, Tsuruga
Sea of Japan side of western Japan	Saigo, Matsue, Yonago, Tottori, Toyooka, Hikone, Shimonoseki, Fukuoka, Oita, Nagasaki, Kumamoto

The annual maximum snow depth ratio in 2022 was 145% relative to the 1991 – 2020 average for the Sea of Japan side of northern Japan, 82% for the same side of eastern Japan, and 62% for the same side of western Japan (Figure 2.5-2). On a longer time scale, the annual maximum snow depth ratio from 1962 on each area is very likely to have decreased (statistically significant at a confidence level of 90% for the Sea of Japan side of northern Japan and 95% for the same side of eastern and western Japan). The annual maximum snow depth reached a local peak in the early 1980s followed by a sharp decline until around the early 1990s. The decline was particularly striking on the Sea of Japan side of eastern and western Japan.

(2) Heavy snowfall frequency

This section describes long-term trends in frequencies of heavy daily snowfall since 1962 at stations on the Sea of Japan side of Japan (Table 2.5-1).

It is very likely that the annual number of heavy snowfall events (such as ≥ 20 cm per day) has decreased for the Sea of Japan side of eastern and western Japan (statistically significant at confidence levels of 95% and 99%, respectively), while that for the Sea of Japan side of northern Japan exhibits no statistically discernible trend (Table 2.5-2, Figure 2.5-3). The average annual number of days with snowfall of ≥ 20 cm per hour in each region from 2013 to 2022 was lower than that for 1962 to 1971 (Table 2.5-2).

The annual number of days with snowfall of ≥ 50 cm exhibits no statistically discernible trend for northern and western Japan (where such events occur only once every few years), possibly due to the rarity of such cases. Values for the Sea of Japan side of eastern Japan are very likely to have decreased (statistically significant at a confidence level of 95%).

Thresholds for extreme events may be inappropriate for some locations due to regional differences in snowfall patterns.

As annual maximum snow depth and snowfall fluctuate greatly and the period covered by observation records is still relatively short, addition of future observations to the data series is expected to increase the reliability of statistical trend determination.

³³ Annual statistical data here are focused on winter (e.g., the value for 1976 is from data for August 1975 – July 1976).

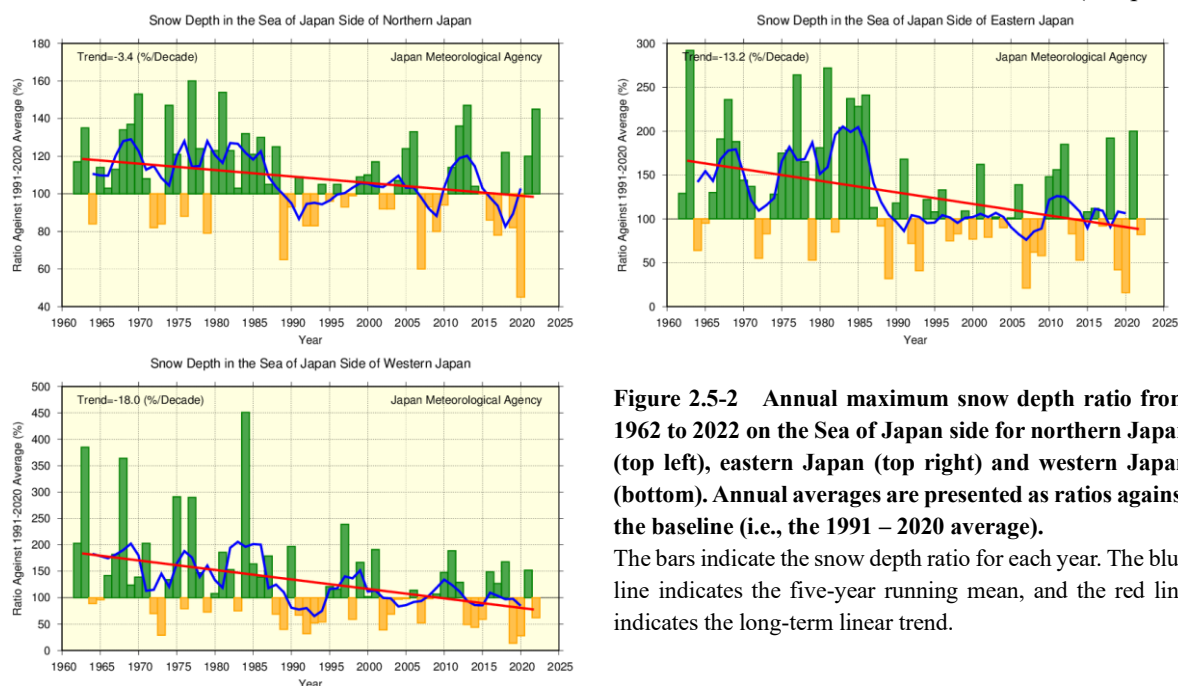
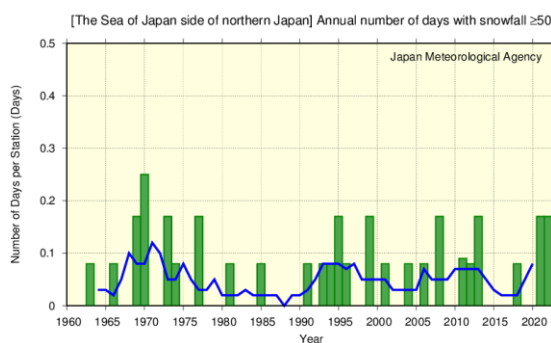
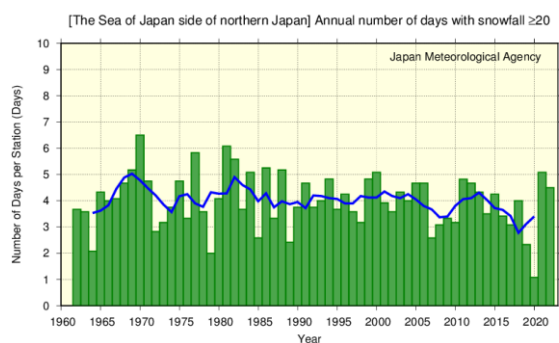


Figure 2.5-2 Annual maximum snow depth ratio from 1962 to 2022 on the Sea of Japan side for northern Japan (top left), eastern Japan (top right) and western Japan (bottom). Annual averages are presented as ratios against the baseline (i.e., the 1991 – 2020 average).

The bars indicate the snow depth ratio for each year. The blue line indicates the five-year running mean, and the red line indicates the long-term linear trend.

Table 2.5-2 Annual numbers of days with snowfall ≥ 20 cm from 1962 to 2022

Element	≥ 20 cm-per-day trend	Frequency ratio (2013 – 2022 average vs. 1962 – 1971 average)
Sea of Japan side of northern Japan	No statistically discernible trend	Approx. x 0.8 (Approx. 4.3 -> Approx. 3.6)
Sea of Japan side of eastern Japan	Extremely likely to have decreased (statistically significant at a confidence level of 95%)	Approx. x 0.5 (Approx. 3.9 -> Approx. 1.9)
Sea of Japan side of western Japan	Extremely likely to have decreased (statistically significant at a confidence level of 99%)	Approx. x 0.4 (Approx. 1.1 -> Approx. 0.5)



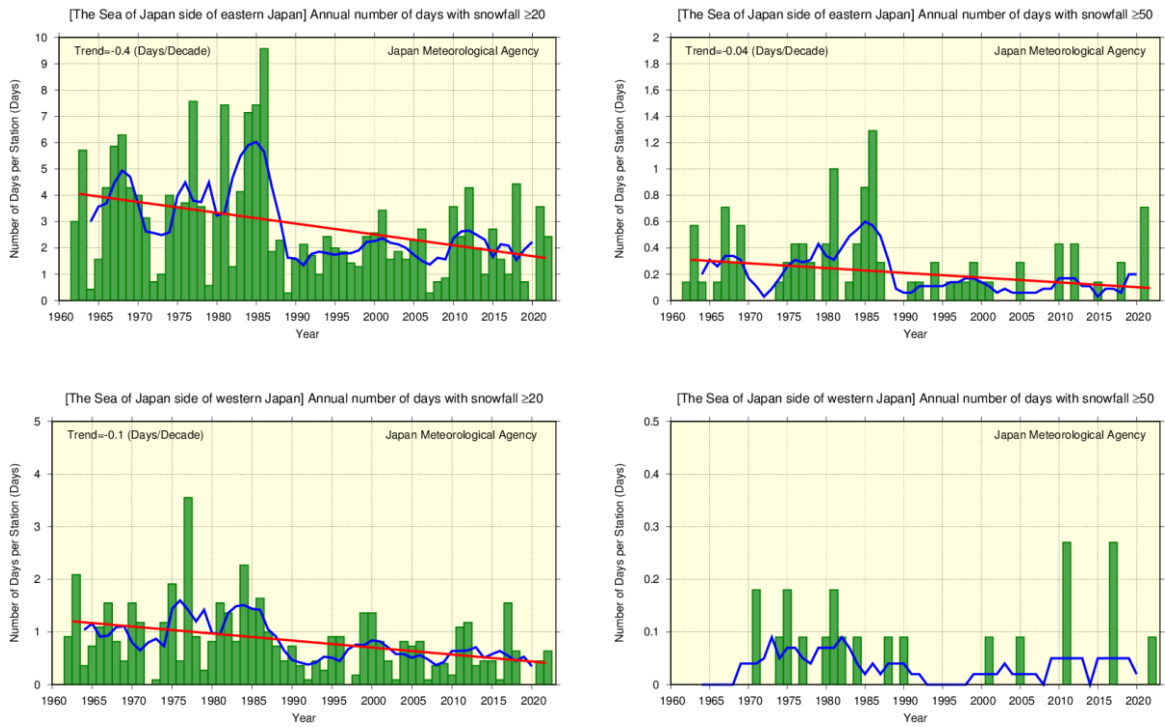


Figure 2.5-3 Annual numbers of days with snowfall of ≥ 20 cm and ≥ 50 cm per day from 1962 to 2022

Top: ≥ 20 cm (left) and ≥ 50 cm (right) for the Sea of Japan side of northern Japan

Middle: ≥ 20 cm (left) and ≥ 50 cm (right) for the Sea of Japan side of eastern Japan

Bottom: ≥ 20 cm (left) and ≥ 50 cm (right) for the Sea of Japan side of western Japan

Green bars indicate annual numbers of days averaged for each year and region (Table 2.5-1), blue lines indicate five-year running means, and red lines indicate long-term linear trends (for confidence levels $\geq 90\%$).

2.6 Tropical cyclones over the western North Pacific and the South China Sea

Sea

- A total of 25 tropical cyclones (TCs) with maximum wind speeds of 34 kt³⁴ or higher formed over the western North Pacific and the South China Sea in 2022, which was close to normal.
- The numbers of formations show no significant long-term trend.

In 2022, 25 tropical cyclones (TCs) with maximum wind speeds of ≥ 34 kt formed over the western North Pacific and the South China Sea (Figure 2.6-1), which was near normal (i.e., the 1991 – 2020 average) of 25.1. The numbers of formations show no discernible long-term trend during the analysis period from 1951 to 2022, while they have often been below normal from the latter half of the 1990s to the early 2010s. Numbers of TCs with maximum wind speeds of ≥ 34 kt approaching and making landfall in Japan were 11 and 3 (Figure 2.6-1), both of which were near normal of 11.7 and 3.0, respectively. The numbers of TCs approaching Japan also show no discernible long-term trend during the same period from 1951 to 2022.

IPCC AR6 WG1 (August 2021) reported that it is likely that the global proportion of major (Category 3–5³⁵) tropical cyclone (with wind speeds exceeding 50 m/s) occurrence has increased over the last four decades (medium confidence), and that it is very likely that the latitude where tropical cyclones in the western North Pacific reach their peak intensity has shifted northward (medium confidence). As long-term trends of strong TCs in the Northwest Pacific were not evaluated with a high degree of confidence in the latest IPCC report, ongoing higher-quality observation and monitoring of long-term trends in results are needed.

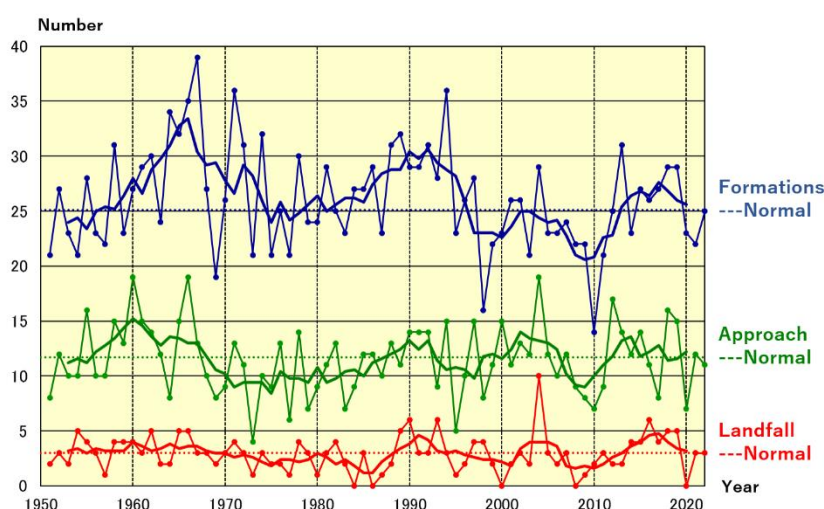


Figure 2.6-1 Time-series of the numbers of TCs with maximum wind speeds of ≥ 34 kt forming in the western North Pacific and the South China Sea (blue), approaching (green) and making landfall in Japan (red) from 1951 to 2022. The thin and thick lines represent annual and five-year running means, respectively.

³⁴ One knot (kt) is about 0.51 m/s

³⁵ "Category 4-5" mentioned here is classifications for hurricane intensity. JMA's evaluation of tropical cyclone intensity is based on 10-minute average wind speeds, while that for hurricanes is based on 1-minute values.

2.7 Phenology of cherry blossoms and acer leaves in Japan

- It is virtually certain that cherry blossoms have been flowering earlier.
- It is virtually certain that acer leaves have been changing color later.

JMA implements phenological observation to monitor seasonal progress, geographical variations and long-term changes in relation to the climate. Observation covers the first/full flowering and foliage color changes in several types of flora.

As part of its phenological monitoring, JMA observes cherry blossoms at 58 stations and acer leaves at 51 stations. Figure 2.7-1 shows interannual changes in the first reported dates of cherry blossom flowering and acer leaf color change between 1953 and 2022. The former exhibits a long-term advancing trend at a rate of 1.2 days per decade, while the latter shows a delaying trend at a rate of 3.0 days per decade (99% level of confidence for both cases). Table 2.7-1 compares climatological normals (based on 30-year averages) of the first reported date of cherry blossom flowering between 1961 – 1990 and 1991 – 2020 at stations in major Japanese cities. These phenomena are closely related to the surface mean temperature in the period before the event, and long-term warming is considered to be a major factor behind the trends observed.

IPCC AR6 WG1 reports several long-term trends in plant phenology. By way of example, peak blooming of cherry blossoms in Kyoto has been increasingly earlier in recent decades based on historical records covering several hundred years (Aono and Saito, 2010)

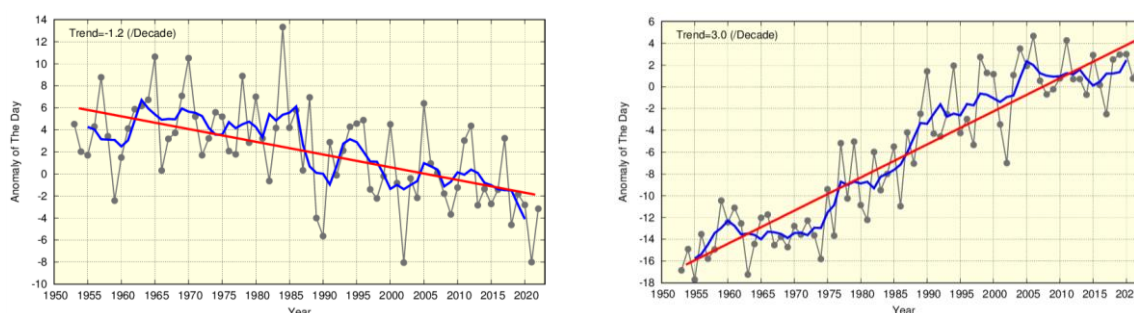


Figure 2.7-1 First reported dates of cherry blossom flowering (left) and acer leaf color change (right)

The black lines show annual anomalies of the first reported date averaged over all observation stations nationwide based on the normals for 1991 – 2020, and the blue lines indicate five-year running means. The red lines show the linear trend (cherry blossoms: -1.2 days per decade; acer leaves: $+3.0$ days per decade).

Table 2.7-1 Comparison of first reported dates of cherry blossom flowering

Differences in climatological normals for the first reported date of cherry blossom flowering between 1991 – 2020 and 1961 – 1990 at stations in major Japanese cities

	1961-1990 average	1991-2020 average	Difference (days)		1961-1990 average	1991-2020 average	Difference (days)
Kushiro	May 19	May 16	-3	Osaka	Apr 1	Mar 27	-5
Sapporo	May 5	May 1	-4	Hiroshima	Mar 31	Mar 25	-6
Aomori	Apr 27	Apr 22	-5	Takamatsu	Mar 31	Mar 27	-4
Sendai	Apr 14	Apr 8	-6	Fukuoka	Mar 28	Mar 22	-6
Niigata	Apr 13	Apr 8	-5	Kagoshima	Mar 27	Mar 26	-1
Tokyo	Mar 29	Mar 24	-5	Naha	Jan 16	Jan 16	0
Nagoya	Mar 30	Mar 24	-6	Ishigakijima	Jan 15	Jan 18	+3

2.8 Sea surface temperature³⁶

- The annual mean global average sea surface temperature (SST) in 2022 was 0.17°C above the 1991 – 2020 average, and was the sixth highest since 1891.
- The global average SST has risen at a rate of about +0.60°C per century.
- Globally integrated ocean heat content (OHC) exhibits a long-term increase.
- OHC has exhibited a higher rate of increase since the mid-1990s.
- Annual average SSTs around Japan have risen by +1.24°C per century.

2.8.1 Global sea surface temperature

The annual mean global average SST in 2022 was 0.17°C above the 1991 – 2020 average. This was the sixth highest since 1891. The years from 2013 to 2022 represent the top-ten warmest since 1891.

The linear trend from 1891 to 2022 shows an increase of +0.60°C per century (Figure 2.8-1). Although magnitudes of the long-term SST trend vary by area, it is extremely likely that SSTs have increased in many parts of the world's oceans (Figure 2.8-2). Global average SSTs and global average surface temperatures (Section 2.3) are affected by natural climate variability on inter-annual to inter-decadal time scales as well as by global warming.

On a multi-year time scale, global average SSTs showed a rising trend from the middle of the 1970s to around 2000, before remaining largely static until the early 2010s and thereafter re-assuming an upward trend (Figure 2.8-1, blue line). This is partly because rising trends overlap with decadal-to-multi-decadal variations in the climate system. It is important to estimate the contribution of these internally induced natural variations in order to properly understand global warming. In the next section, the Pacific Decadal Oscillation (PDO) is presented as a typical example of decadal variability observed in SSTs.

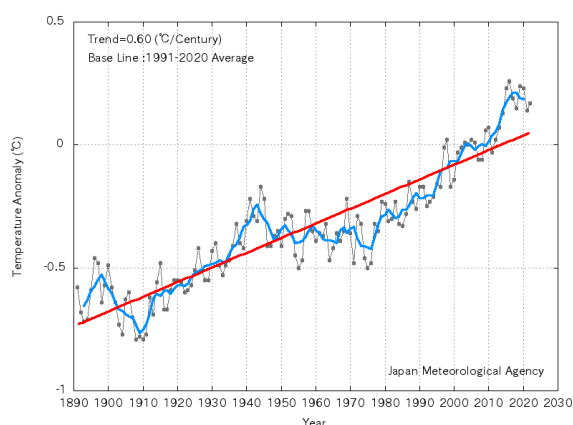


Figure 2.8-1 Time-series representation of global average sea surface temperature anomalies from 1891 to 2022

The black, blue and red lines indicate annual anomalies, the five-year running mean and the long-term linear trend, respectively. Anomalies are deviations from the 1991 – 2020 average.

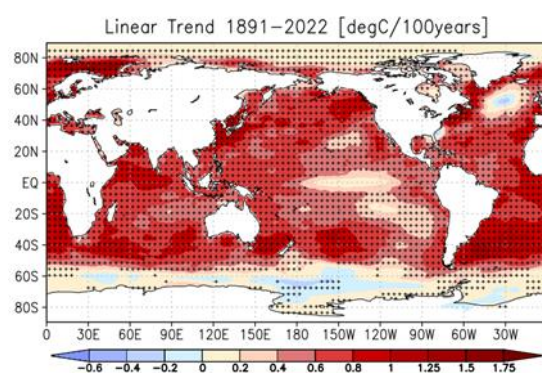


Figure 2.8-2 Linear trend of annual mean sea surface temperature during the period from 1891 to 2022 (°C per century)

Plus signs indicate statistically significant trends with a confidence level of 95%.

³⁶ The results of analysis regarding tendencies of SSTs worldwide and around Japan are published on JMA's website.

https://www.data.jma.go.jp/kaiyou/english/long_term_sst_global/glb_warm_e.html

https://www.data.jma.go.jp/kaiyou/english/long_term_sst_japan/sea_surface_temperature_around_japan.html

2.8.2 Global ocean heat content

Oceans have a significant impact on the global climate because they cover about 70% of the earth’s surface and have high heat capacity. IPCC AR6 WG1 (IPCC, 2021) said that approximately 90% of heat energy in the earth’s system was present in oceans since 1970.

It is virtually certain that globally integrated ocean heat content (OHC) from 0 to 2,000 m exhibits a long-term increase (statistically significant at a confidence level of 99%) (Figure 2.8-3). OHC had risen by approximately 47×10^{22} J in 2022 relative to 1955. Since the mid-1990s, the rate of increase (10.0×10^{22} J per decade for 1993 – 2022) has risen (3.9×10^{22} J per decade for 1955 – 1993). The Intergovernmental Panel on Climate Change Special Report on the Ocean and Cryosphere in a Changing Climate (IPCC, 2019) and IPCC (2021) also reported an accelerated increase of ocean heat uptake.

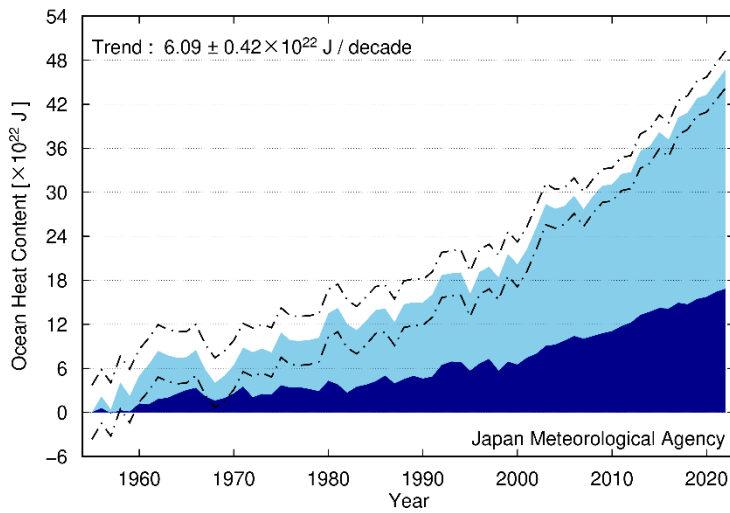


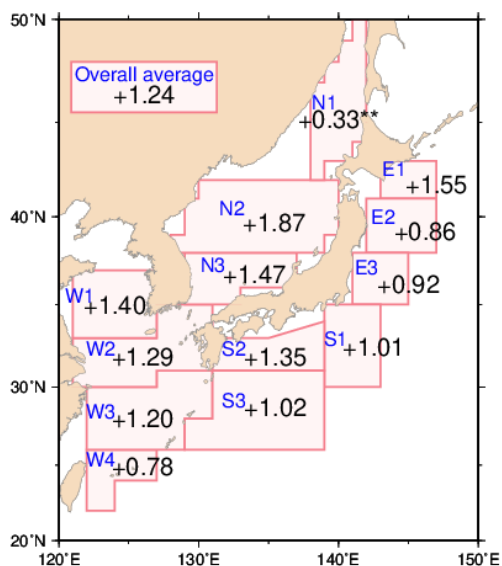
Figure 2.8-3 Time-series representation of globally integrated ocean heat content relative to 1955

The light- and dark-blue areas show annual means for global integrals of 0 to 700 m and 700 to 2,000 m, respectively, for ocean heat content relative to 1955. The dot-dash lines indicate a 95% confidence level for ocean heat content above 2,000 m.

2.8.3 Sea surface temperature (around Japan)

Figure 2.8-4 shows increase rates of area-averaged annual mean SSTs for 13 areas around Japan. Values for all areas have risen by $+1.24^{\circ}\text{C}$ per century, which is higher than the corresponding value for the North Pacific ($+0.62^{\circ}\text{C}$ per century). In addition to this long-term increase, SSTs fluctuate on time scales ranging from years to decades. Values have shown an upward trend in recent years, with 2022 being the second-highest after 2021.

It is virtually certain (statistically significant at a confidence level of 99%) that SSTs have risen by between $+0.78$ and $+1.87^{\circ}\text{C}$ per century in the sea off Kushiro, the sea off Sanriku, eastern and southern parts of the sea off Kanto, the sea off Shikoku and Tokai, east of Okinawa, the central and southwestern parts of the Sea of Japan, the Yellow Sea, the East China Sea, and the sea around the Sakishima Islands (areas E1-3, S1-3, N2-3, and W1-4). It is very likely (statistically significant at a confidence level of 90%) that SSTs in the northeastern part of the Sea of Japan (area N1) have risen by $+0.33^{\circ}\text{C}$ per century.



Area number	Area name
E1	Sea off Kushiro
E2	Sea off Sanriku
E3	Eastern part of the sea off Kanto
S1	Southern part of the sea off Kanto
S2	Sea off Shikoku and Tokai
S3	East of Okinawa
N1	Northeastern part of the Sea of Japan
N2	Central part of the Sea of Japan
N3	Southwestern part of the Sea of Japan
W1	Yellow Sea
W2	Northern part of the East China Sea
W3	Southern part of the East China Sea
W4	Sea around the Sakishima Islands

Figure 2.8-4 Increase rates of area-averaged annual mean SSTs around Japan from 1900 to 2022 (°C per century)
 Areas with no symbol and those marked with [**] have statistical significant trend at confidence levels of 99% and 90 %.

2.9 El Niño/La Niña³⁷ and PDO (Pacific Decadal Oscillation)³⁸

- The La Niña event that emerged in autumn 2021 continued in 2022.
- Negative PDO index values were generally observed from around 2000 to the early 2010s, positive values persisted in the late 2010s, and negative values have been observed since around 2021.

2.9.1 El Niño/La Niña

An El Niño event is a phenomenon in which sea surface temperatures (SSTs) are above normal over the equatorial Pacific from near the date line to the coast of South America for around a year. In contrast, a La Niña event is a phenomenon in which SSTs are below normal over the same area. Both events occur every few years, causing changes in global atmospheric circulations which result in abnormal weather conditions worldwide. In Japan, cooler summers and warmer winters tend to appear during El Niño events, while hotter summers and colder winters tend to appear during La Niña events.

Figure 2.9-1 shows a time-series representation of SST deviations from climatological means based on a sliding 30-year period for the El Niño monitoring region (5°N – 5°S, 150°W – 90°W) and SST deviations from reference values based on linear extrapolation with respect to the latest sliding 30-year period for the tropical western Pacific region (Eq. – 15°N, 130 – 150°E) since 2012. SSTs in the El Niño monitoring region were below related reference values from October 2021 to June 2022 and from August 2022 onward, and were near these values in July 2022. These variations are consistent with the presence of La Niña conditions from autumn 2021 onward. SSTs in the tropical western Pacific were above related reference values from August to November 2021, and near or below these values from December 2021 to August 2022.

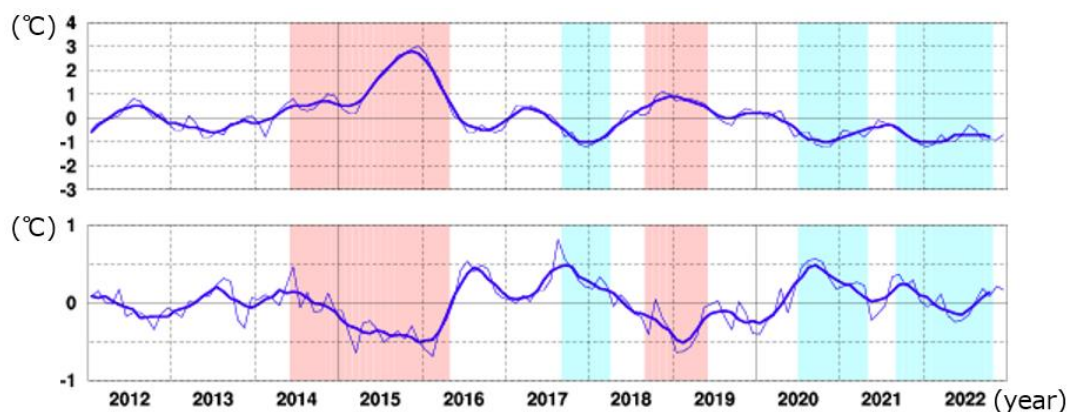


Figure 2.9-1 Time-series representations of SST deviations from the climatological mean based on a sliding 30-year period for the El Niño monitoring region (top) and SST deviations from reference values based on linear extrapolation with respect to the latest sliding 30-year period for the Western Pacific (bottom)

Thin lines indicate monthly means, and smooth thick curves indicate the five-month running mean.

Red shading denotes El Niño periods, and blue shading denotes La Niña periods.

³⁷ See the Glossary for terms relating to El Niño phenomena. Monthly diagnosis reports, ENSO monitoring products, ENSO indices and El Niño outlooks are published on JMA's website.

<https://www.data.jma.go.jp/tcc/tcc/products/elnino/index.html>

³⁸ The PDO index time series is published on JMA's website.

<https://www.data.jma.go.jp/tcc/tcc/products/elnino/decadal/pdo.html>

2.9.2 Pacific Decadal Oscillation

SST variability is also observed on time scales ranging from one to several decades in addition to El Niño/La Niña events, whose time scale is several years, and long-term trends associated with global warming. Among these, the atmosphere and oceans tend to co-vary with a period of more than ten years in the North Pacific in a phenomenon known as the Pacific Decadal Oscillation (PDO, Mantua et al. 1997). When SSTs are lower (higher) than their normals in the central part of the North Pacific, those in its part along the coast of North America are likely to be higher (lower) than their normals. This seesaw pattern changes slowly, and appears repeatedly with a period of more than ten years. The PDO index, which is defined by the SST anomaly pattern in the North Pacific, is used as a measure of phase and strength of the oscillation. Since both the PDO index and SST anomaly patterns associated with PDO are estimated based on monthly mean SST anomalies, it is noted that they include relatively short-timescale variabilities such as El Niño/La Niña events in addition to decadal to multi-decadal components.

When the PDO index is positive (negative), SSTs in the central part of the North Pacific are likely to be lower (higher) than their normals in addition to those along the coast of North America, and those in the equatorial part from near the date line to the coast of South America are likely to be higher (lower) than normal. This tendency is analogous to the patterns observed in El Niño (La Niña) events (Figure 2.9-2). Additionally, sea level pressures (SLPs) in the high latitudes of the North Pacific are likely to be lower (higher) than their normals in the same time (Figure 2.9-3). This indicates that the Aleutian Low is stronger (weaker) than its normal in winter and spring. These atmospheric variations affect meteorological conditions mainly in North America. When the PDO index is positive, winter temperatures tend to be high in the northwestern part of North America and the northern part of South America, and low in the southeastern part of the USA and in parts of China (Mantua and Hare, 2002).

The PDO index was generally positive from the late 1920s to the early 1940s, from the late 1970s to around 2000 and in the late 2010s, and was generally negative from the late 1940s to the mid-1970s and from around 2000 to the early 2010s (Figure 2.9-4). Negative values persisted since around 2021.

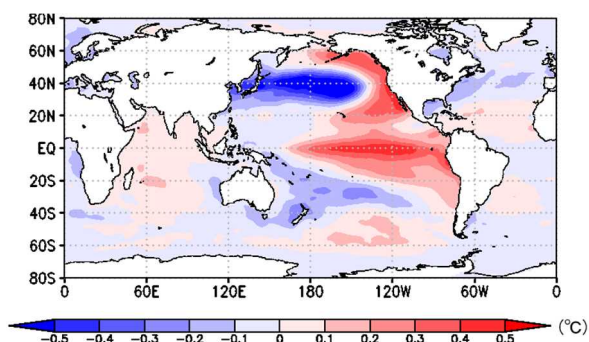


Figure 2.9-2 Typical SST anomaly patterns in the positive phase of the PDO

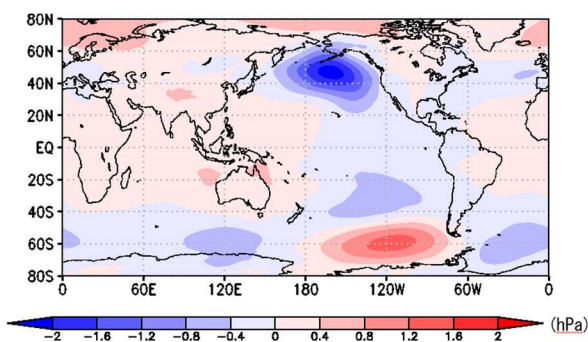


Figure 2.9-3 Typical SLP anomaly patterns in the positive phase of the PDO

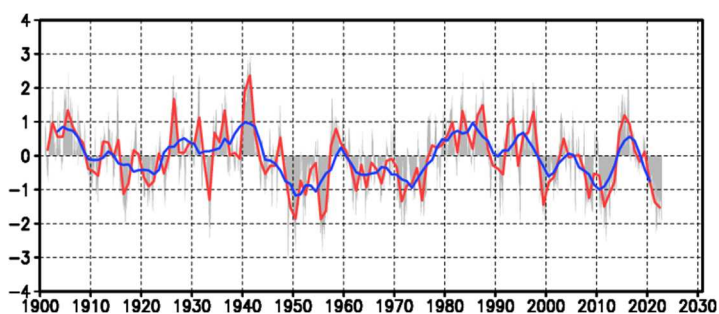


Figure 2.9-4 Time-series of the PDO index

The red line represents annual mean values for the PDO index, the blue line represents five-year running mean values, and the gray bars represent monthly values.

2.10 Sea levels around Japan³⁹

- No significant long-term trend of sea level rise has been observed around Japan over the last 100 years.
- A trend of sea level rise has been observed since the 1980s.

Sea levels in Japanese coastal areas exhibited no significant rise from 1906 to 2022 (Figure 2.8-1).

This is attributed to variations over 10- to 20-year and 50-year-plus periods for the period from 1906 to 2022. The major factor behind sea level variations with 10- to 20-year periods is the variability of atmospheric circulation over the North Pacific. Westerlies in the mid-latitudes of the Northern Hemisphere are strengthened in boreal winter, and the consequent decadal variations in turn cause sea level variations in the central North Pacific. These propagate westward due to the earth's rotation, causing sea level rise around Japan. The high sea levels observed around 1950 were induced by a weakening of the Aleutian low.

However, a trend of sea level rise has been observed since the 1980s. The annual mean sea level around Japan in 2022 was 63 mm higher than the normal (i.e., the 1991 – 2020 average), making it the second highest since 1906.

IPCC AR6 WG1 (IPCC, 2021) concluded: "heating of the climate system has caused global mean sea level rise through ice loss on land and thermal expansion from ocean warming. Global mean sea level increased by 0.20 [0.15 to 0.25] m⁴⁰ between 1901 and 2018. The average rate of sea level rise was 1.3 [0.6 to 2.1] mm/year between 1901 and 1971, increasing to 1.9 [0.8 to 2.9] mm/year between 1971 and 2006, and further increasing to 3.7 [3.2 to 4.2] mm/year between 2006 and 2018 (high confidence). Human influence was very likely the main driver of these increases since at least 1971." In contrast to the globally averaged rate noted in the IPCC report, sea levels in coastal areas of Japan exhibited no significant rise from 1906 to 2018. Recent rates of rise around the country have been 2.9 [0.8 to 5.0] mm/year from 2006 to 2018. These figures are comparable to those observed for the global average in recent years.

Sea levels along the coast of Japan are predominantly variable with decadal cycles, but the contributions of these variations and changes associated with global warming have not been quantitatively evaluated. Continuous monitoring is needed to determine the long-term trend of sea level rise caused by global warming.

³⁹ Sea levels around Japan are published on the JMA's website.

https://www.data.jma.go.jp/gmd/kaiyou/english/sl_trend/sea_level_around_japan.html

⁴⁰ The values in square brackets show the 90% uncertainty range.

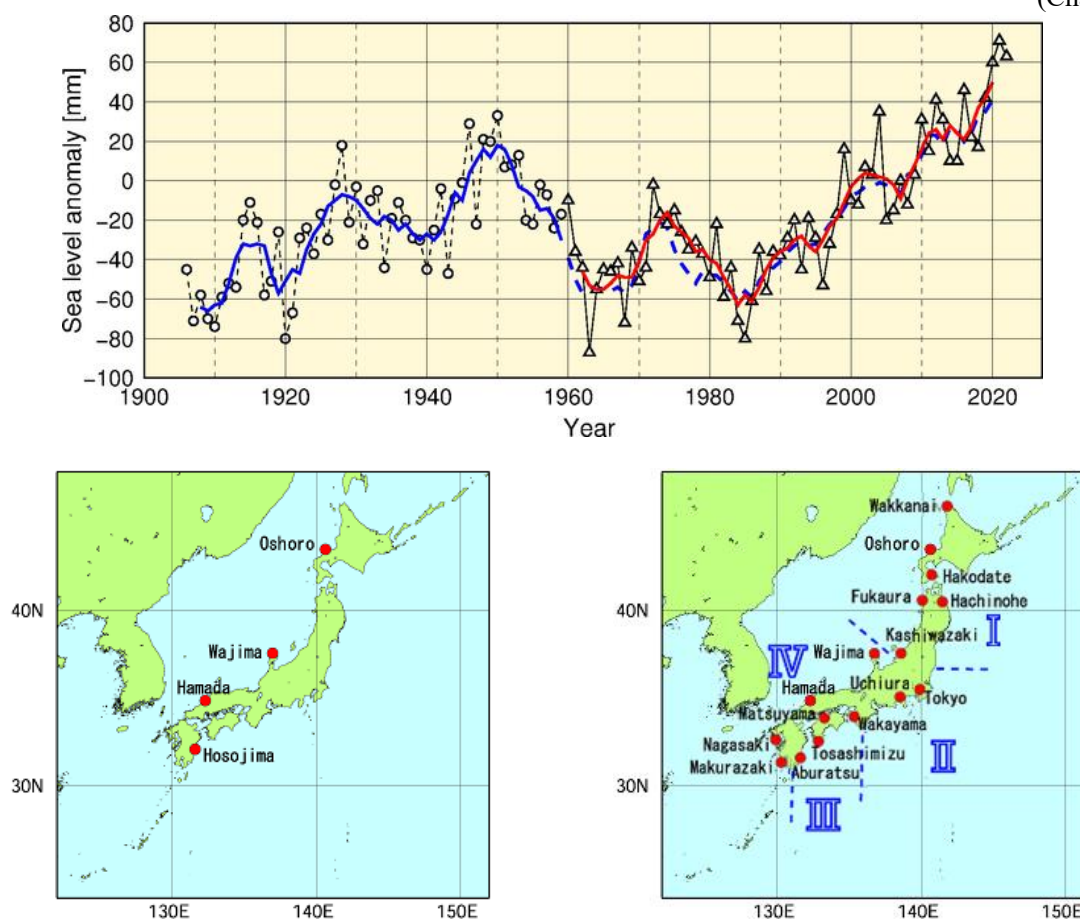


Figure 2.10-1 Time-series representation of annual mean sea levels (1906 – 2022) and locations of tide gauge stations

Tide gauge stations assessed as being affected to a lesser extent by crustal movement are selected. The four stations shown on the map on the left are used for the period from 1906 to 1959, and the sixteen shown on the right are used for the period since 1960. From 1906 to 1959, a time-series representation of mean annual mean sea level anomalies for the selected stations is shown. For the period since 1960, the nation's islands were then divided into four regions based on sea level variation characteristics, annual mean sea level anomalies were averaged for each of the regions, and the variations were plotted in the figure. The four regions are I: from Hokkaido to Tohoku district; II: from Kanto to Tokai district; III: from the Pacific coast of Kinki to that of Kyushu district; and IV: from Hokuiku to East China Sea coast of Kyushu district. Sea level variations are plotted on the chart as a time-series representation of annual mean sea level anomalies for each year, obtained using the 1991 to 2020 average as the normal. The solid blue line represents the five-year running mean of annual sea level anomalies averaged among the four stations shown in the lower left map, while the solid red line represents that averaged among the four divided regions in the lower right map. The dashed blue line represents the value averaged among the four stations shown in the lower left map for the same period shown by the solid red line (after 1960) for reference. The coefficient of correlation between the solid red line and the dashed blue line from 1962 to 2020 is as high as 0.99. Accordingly, the extent to which changing the tide gauge stations used in the monitoring affects the analysis of variance of sea level anomalies can be regarded as small. Among the tide gauge stations, those at Oshoro, Kashiwazaki, Wajima and Hosojima belong to the Geospatial Information Authority of Japan. Sea level data for the Tokyo station are available from 1968 onward. Sea level data for the period from 2011 to 2022 from Hakodate, Fukaura, Kashiwazaki, Tokyo and Hachinohe were not used due to possible influences from the 2011 off the Pacific coast of Tohoku Earthquake.

2.11 Sea ice⁴¹

- The sea ice extent in the Arctic Ocean is decreasing.
- The annual maximum sea ice extent in the Antarctic Ocean is extremely likely to increase.
- The maximum sea ice extent in the Sea of Okhotsk shows a decreasing trend of $0.056 \times 10^6 \text{ km}^2$ per decade.

2.11.1 Sea ice in Arctic and Antarctic areas

Sea ice is formed in the Arctic and Antarctic. As the albedo (reflection coefficient) of sea ice is greater than that of the ocean surface, sea ice extent reductions caused by global warming result in more solar energy absorption at the surface, which in turn accelerates global warming. Sea ice also affects deep-ocean circulation because the expelled salt as it forms increases the salinity (and therefore the density) of the water below it causing the water to sink.

It is virtually certain that there has been a long-term trend of decrease in sea ice extent in the Arctic Ocean since 1979 when continuous monitoring of sea ice using satellite sensors with similar properties started (statistically significant at a confidence level of 99%). In particular, the reduction in the annual minimum extent is notable. The rate of decrease in the annual minimum up to 2022 was $0.087 \times 10^6 \text{ km}^2$ per year. Meanwhile, it is extremely likely that there has been a long-term trend of increase in sea ice extent at a rate of $0.011 \times 10^6 \text{ km}^2$ per year in the annual maximum sea ice extent in the Antarctic Ocean (statistically significant at the confidence level of 95%). There have been no discernible trends in the annual and minimum sea ice extent in the Antarctic Ocean⁴². The annual mean and minimum sea ice extent in 2022 were both the lowest values since 1979.

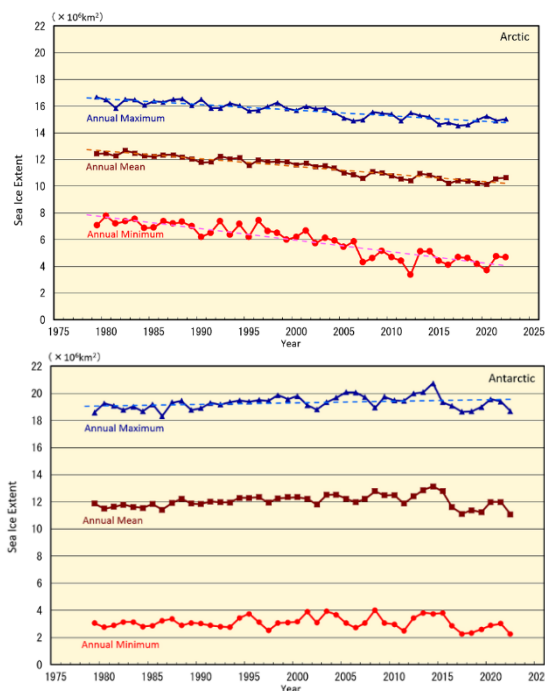


Figure 2.11-1 Time-series representations of annual maximum, annual mean, and annual minimum sea ice extent in the Arctic Ocean (including the Sea of Okhotsk and the Bering Sea) (upper) and in the Antarctic Ocean (lower) from 1979 to 2022

The solid blue, brown and red lines indicate the annual maximum, the annual mean, and the annual minimum sea ice extent, respectively. The dashed lines indicate the linear trends (statistically significant at the confidence level of 95%). Sea ice extents are calculated from brightness temperature data provided by NASA (the National Aeronautics and Space Administration) and NSIDC (the National Snow and Ice Data Center).

⁴¹ Information on sea ice in the Arctic/Antarctic, and in the Sea of Okhotsk are published on JMA's website.

https://www.data.jma.go.jp/kaiyou/english/seaiice_global/series_global_e.html (Arctic/Antarctic)

https://www.data.jma.go.jp/kaiyou/english/seaiice_okhotsk/series_okhotsk_e.html (Sea of Okhotsk)

⁴² It was reported in IPCC AR6 WG1 (2021) that there has been no significant trend in Antarctic sea ice area from 1979 to 2020 due to regionally opposing trends and large internal variability.

In 2022, the annual maximum Arctic sea ice extent was $15.01 \times 10^6 \text{ km}^2$ on February 22. The extent subsequently decreased during spring and summer in the Northern Hemisphere and reached its annual minimum of $4.67 \times 10^6 \text{ km}^2$ on September 17. Meanwhile, the Antarctic sea ice extent was at its annual minimum of $2.24 \times 10^6 \text{ km}^2$ on February 19, marking the lowest value since 1979. The extent subsequently increased during the autumn and winter months of the Southern Hemisphere and reached its annual maximum of $18.70 \times 10^6 \text{ km}^2$ on September 15 (Figures 2.11-2, 2.11-3).

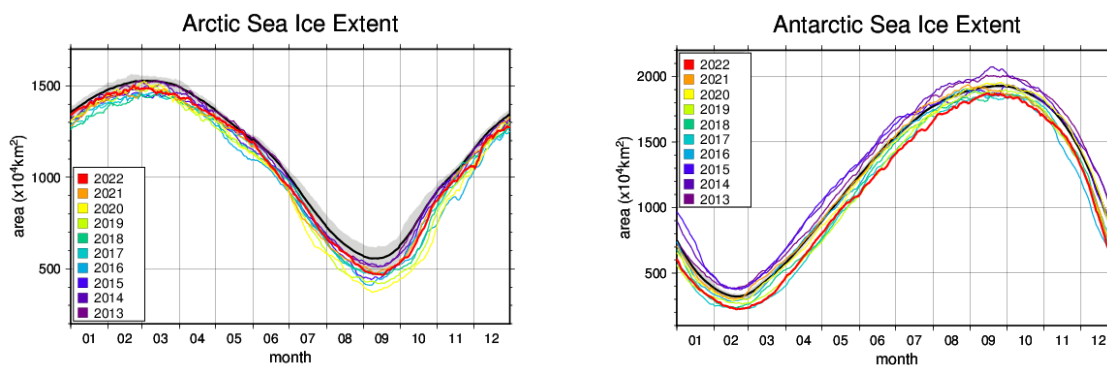


Figure 2.11-2 Annual variations of sea ice extent in the Arctic (left) and Antarctic (right) areas in 2022 (red line)
Black lines represent the normal, and shading represents the range of the normal.

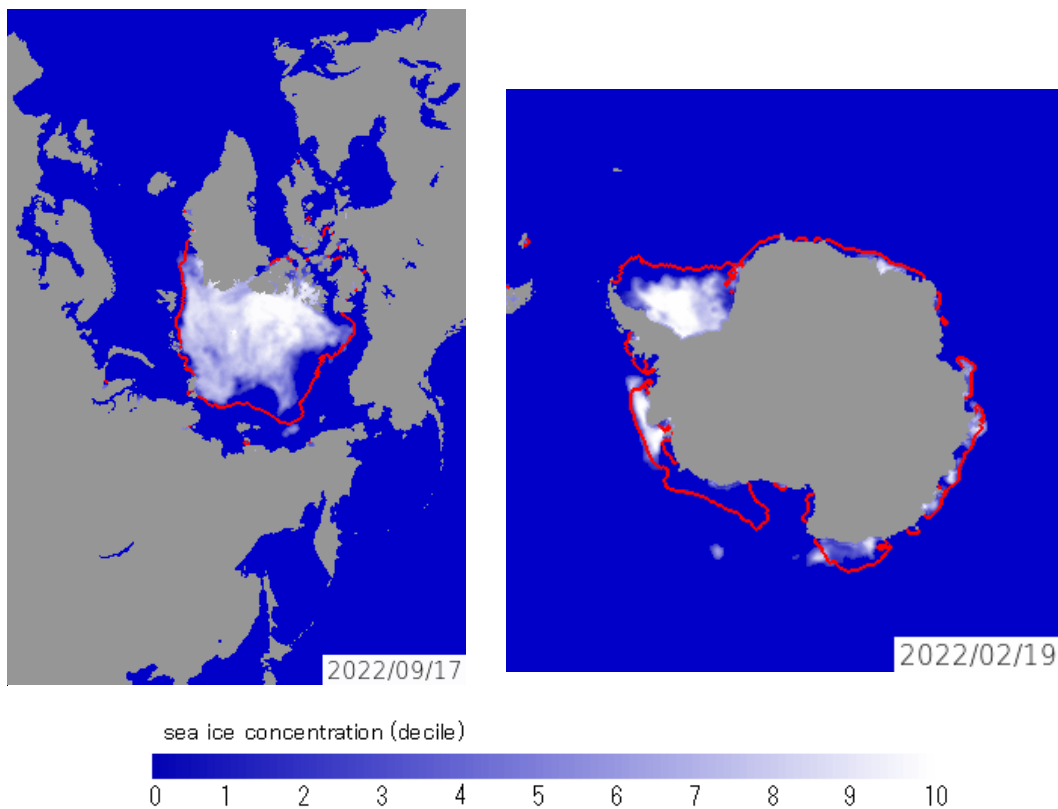


Figure 2.11-3 Annual minimum sea ice distribution for the Arctic and Antarctic
The figure on the left shows Arctic sea ice concentration on September 17 2022, and on the right is Antarctic sea ice concentration on February 19 2022. The red lines represent the normal sea ice edge for the relevant days.

2.11.2 Sea ice in the Sea of Okhotsk

The Sea of Okhotsk is the southernmost sea in the Northern Hemisphere where sea ice is observed across a wide area. The variation of the sea ice in the Sea of Okhotsk has effect on climate in coastal area facing the Sea of Okhotsk in Hokkaido and water quality of Oyashio.

The maximum⁴³ sea ice extent in the Sea of Okhotsk shows large interannual variations. However, it is virtually certain that it exhibited a long-term trend of decrease for the period from 1971 to 2022 (statistically significant at the confidence level of 99%). The maximum extent has decreased by $0.056 \times 10^6 \text{ km}^2$ per decade (corresponding to 3.5% of the Sea of Okhotsk's total area).

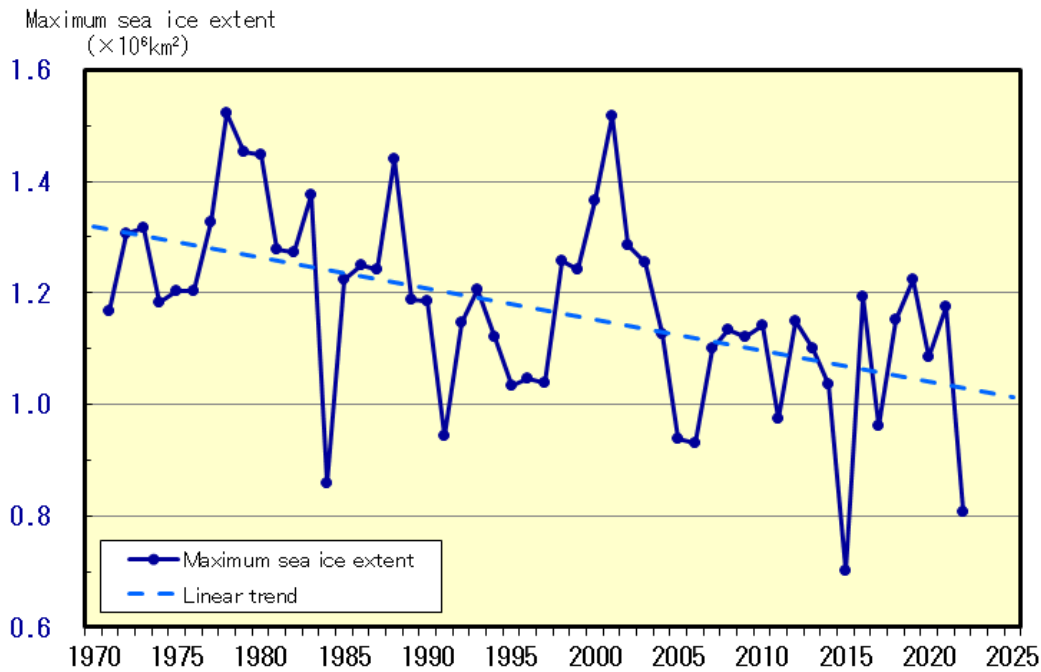


Figure 2.11-4 Time-series representations of maximum sea ice extent for the Sea of Okhotsk from 1971 to 2022

Straight line indicates the linear trend.

⁴³ The maximum sea ice extent: It shows sea ice extent that sea ice was the most expanding of every five days in the winter.

2.12 Ocean carbon dioxide and ocean acidification

- Concentrations of carbon dioxide in the air and in the oceans are increasing.
- Anthropogenic carbon dioxide is absorbed into the ocean and accumulates there.
- Oceanic acidity has increased due to accumulation of anthropogenic carbon dioxide.

The ocean acts as a large sink for CO₂ emitted as a result of human activity, and the chemical properties of seawater have changed due to the uptake and reserve of anthropogenic CO₂. Ocean acidification, known as the decrease in ocean pH (hydrogen ion exponents), is a particular issue of concern because it accelerates global warming by limiting the ocean's capacity of CO₂ uptake from the atmosphere and affects marine ecosystems by disturbing plankton growth. Numerical model experiments based on future CO₂ emission estimates show an ocean surface pH decrease of 0.16 – 0.44 from the end of the 19th century to the end of the 21st century (IPCC AR6: IPCC 2021). The CO₂ absorbed by the ocean is considered to have been transported into the ocean interior through ocean circulation and biological processes, and to be causing ocean acidification in the interior as well as in the surface layer.

2.12.1 Ocean carbon dioxide

(1) Ocean carbon dioxide in the western North Pacific

Based on data collected by JMA research vessels along the 137°E (3 – 34°N) and 165°E (5°S – 35°N) lines, oceanic and atmospheric *p*CO₂ are increasing in the western North Pacific area (Figures 2.12-1, 2.12-2). The growth rates for oceanic and atmospheric *p*CO₂ along the 137°E line from 1985 to 2022 were 1.6 – 2.1 and 1.8 – 2.0 μatm/year, respectively, while those along the 165°E line from 1996 to 2022 were 1.7 – 2.7 and 1.9 – 2.1 μatm/year, respectively. Oceanic *p*CO₂ exhibits seasonal variations, being higher in summer with higher SSTs and lower in winter with lower SSTs, and the range of variation is more volatile at higher latitudes along both lines. Meanwhile, atmospheric *p*CO₂ is constant and higher than those of oceanic *p*CO₂ except in summer. Consequently, the ocean absorbs atmospheric CO₂ emissions overall, other than in equatorial areas, resulting in a release of CO₂ into the atmosphere over the year because oceanic *p*CO₂ values are higher than those of atmospheric *p*CO₂.

The column inventory of ocean CO₂ was estimated using long-term time-series data on dissolved inorganic carbon from 1990s (Figure. 2.12-3). The column inventory rates of ocean CO₂ between the sea surface and 27.2 σ_θ (approx. 1,000 m in depth) along 137°E, 165°E and 24°N are approximately 4 – 11 tC·km⁻²·year⁻¹. The column inventory rates of ocean CO₂ around 20 – 30°N are higher than those at 10°N and 35°N. This is caused by the transport of CO₂ from the surface to the ocean interior by water masses known as North Pacific subtropical mode water and North Pacific intermediate water.

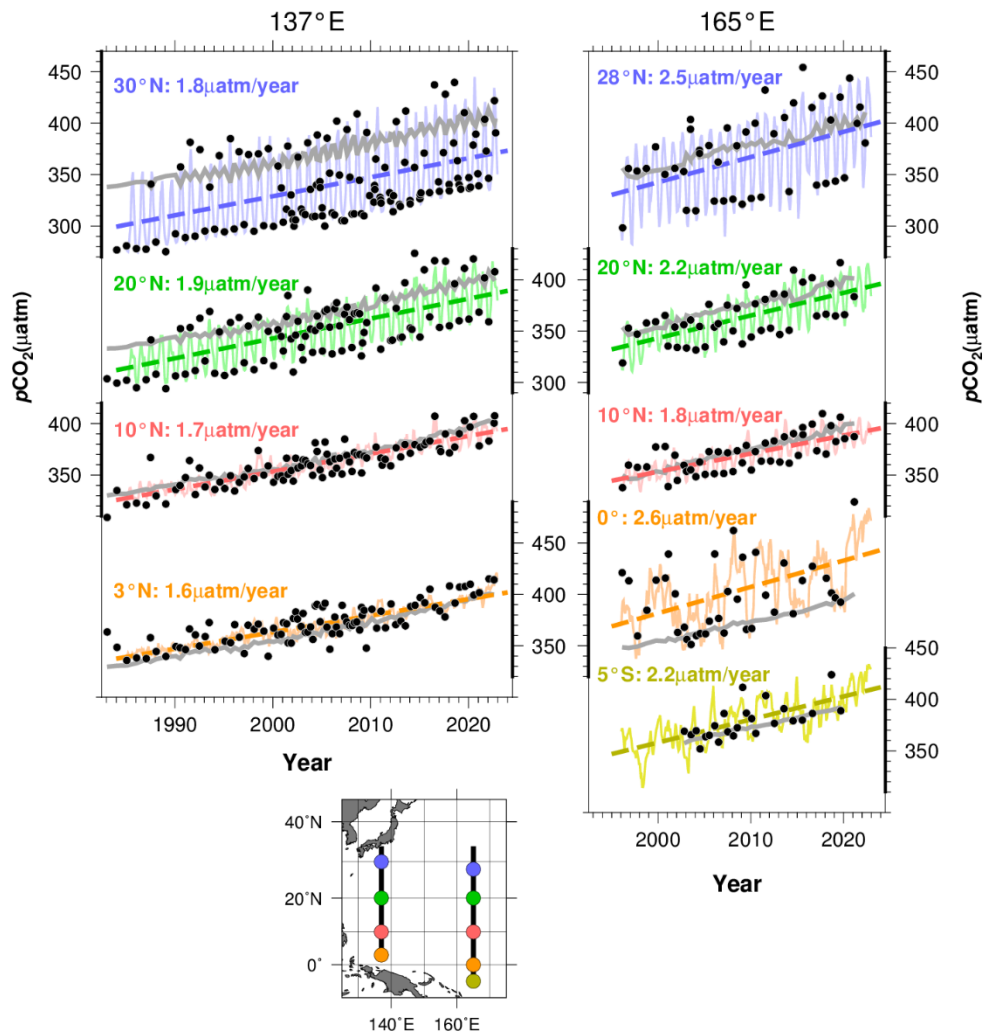


Figure 2.12-1 Annual changes in oceanic and atmospheric $p\text{CO}_2$ along the 137°E (left) and the 165°E (right) lines
 Black plots show oceanic $p\text{CO}_2$ observation values. Solid lines represent monthly oceanic $p\text{CO}_2$ values reconstructed using the method of Ishii et al. (2011), dashed lines show the long-term trend of oceanic $p\text{CO}_2$, and gray lines indicate the observed values of atmospheric $p\text{CO}_2$.

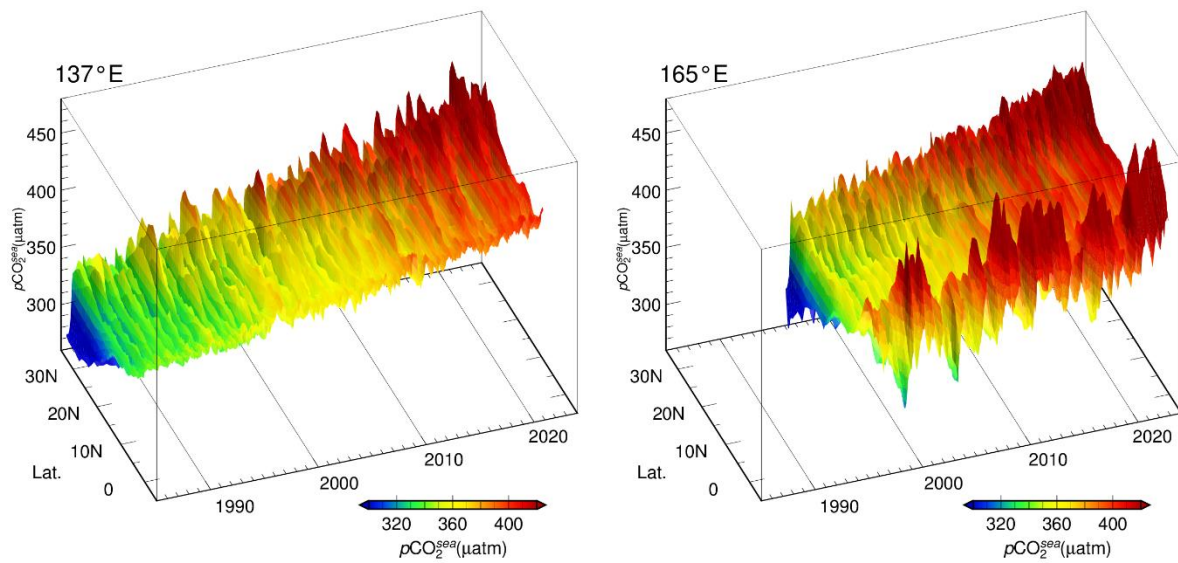


Figure 2.12-2 Time-latitude distribution of oceanic $p\text{CO}_2$ along the 137°E (left) and the 165°E (right) lines
 Colors indicate reconstructed monthly oceanic $p\text{CO}_2$ value. The part on the left shows oceanic $p\text{CO}_2$ along the 137°E (3-34°N) since 1985 and the part on the right shows oceanic $p\text{CO}_2$ along the 165°E (5°S-35°N) since 1996.

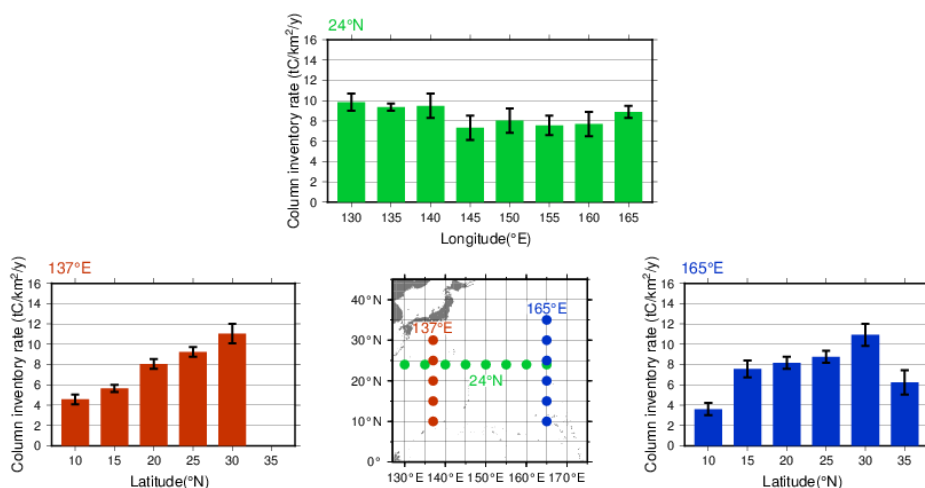


Figure 2.12-3 Changes in ocean CO₂ between the sea surface and 27.2 σ_θ (approx. 1,000 m in depth) along 137°E, 165°E and 24°N for the periods 1994 – 2022, 1992 – 2022 and 1992 – 2022, respectively.

Error bars denote a 95% confidence level

(2) Global ocean carbon dioxide uptake

Analysis of observation data reveals relationships between surface ocean CO₂ concentrations and other oceanographic parameters such as sea surface temperature (SST), salinity and chlorophyll-a concentration, which differ by region. Global ocean CO₂ concentrations were estimated using datasets of such parameters based on these relationships, and CO₂ exchanges between the atmosphere and the ocean were calculated (Iida *et al.*, 2021). It was found that the ocean releases CO₂ into the atmosphere in equatorial regions and the northern Indian Ocean, where seawater with a high CO₂ concentration upwells and absorbs CO₂ in other regions (Figure 2.12-4 (a)). Lower SSTs in winter and biological CO₂ consumption in spring/autumn result in lower surface ocean CO₂ concentrations and therefore higher CO₂ uptake, especially in the mid-to-high latitudes. Figure 2.12-4 (b) and (c) show monthly and annual variations in global ocean CO₂ uptake, respectively. The estimated mean annual global ocean CO₂ uptake during 1990 to 2021 was 2.0 GtC per year. Considering natural CO₂ efflux of 0.6 GtC per year (IPCC, 2021), which results from riverine input to the oceans, the amount of ocean CO₂ uptake corresponds to a quarter of all anthropogenic CO₂ emission, which IPCC (2021) estimates to be 10.9 GtC per year. Global ocean CO₂ uptake is affected by the variability of global SST distribution and biological activity, and decreases/increases in boreal summer/winter (Figure 2.12-4 (b)). The estimated annual global ocean CO₂ uptake has increased during the period.

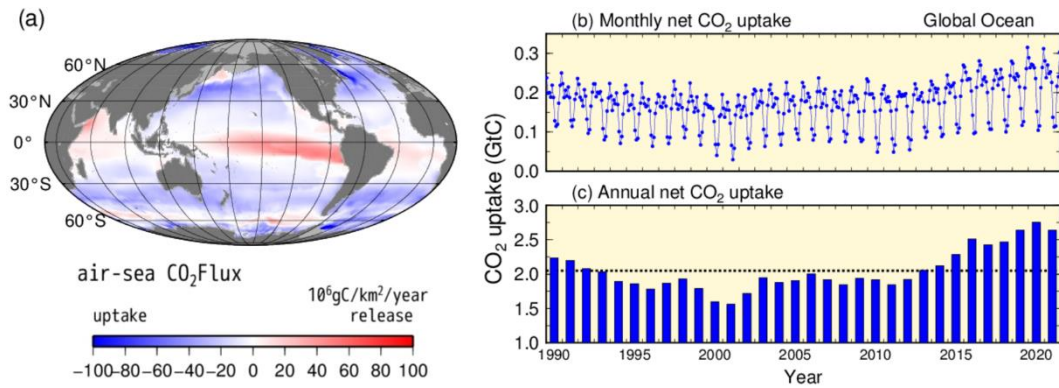


Figure 2.12-4 Distribution of global ocean CO₂ uptake/release for 2021 (a) and time-series representations of monthly (b) and annual (c) CO₂ uptake from 1990 to 2021

The blue/red area in the map on the left (a) indicates ocean uptake/release of CO₂ from/into the atmosphere. The grey area shows the border of the region analyzed. The dotted line in graph (c) shows the 2.0 GtC average for the period from 1990 to 2021.

2.12.2 Ocean acidification

(1) Ocean acidification around Japan

To monitor the long-term variability of ocean acidification, JMA has analyzed monthly sea surface pH values since 1998 based on data from its oceanographic observations and related database content. The results show a clear trend of in-situ pH decrease in seas around Japan ranging from 0.019 per decade around Kyushu and Okinawa to 0.022 per decade in the Sea of Japan. The average trend in sea areas around Japan is 0.020 per decade. These values are similar to observed rates of pH decrease in worldwide open oceans as recorded in the IPCC special report (SROCC; IPCC, 2019).

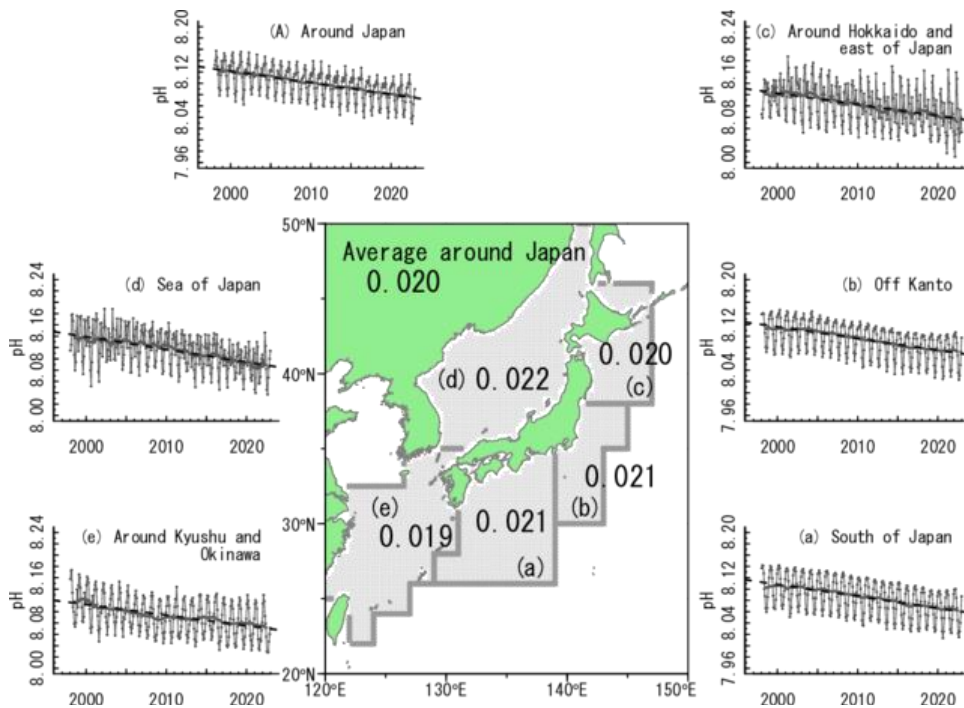


Figure 2.12-5 Long-term trends of pH in sea areas around Japan

Black points with lines, bold lines and dashed lines indicate average pH values, yearly running means and long-term trends in areas (a) to (e), and the average around Japan, respectively.

(2) Ocean acidification in the western North Pacific

JMA monitors long-term trends in surface and interior ocean pH along repeat hydrographic lines at 137°E and 165°E, and performs analysis to determine the average decrease in surface ocean pH throughout the Pacific using data on oceanic CO₂ concentration and related factors. The results clearly show a decreasing trend in surface ocean pH for the whole Pacific, and 0.015 to 0.021 and 0.017 to 0.027 per decade at individual stations on the 137°E and 165°E lines, respectively (Figures 2.12-6 and 2.12-7). Ocean interior pH along these lines also shows decreasing trends of 0.012 to 0.031 per decade (Figure 2.12-8) with higher rates in the northern than the southern subtropics due to greater accumulation of anthropogenic CO₂ in the former.

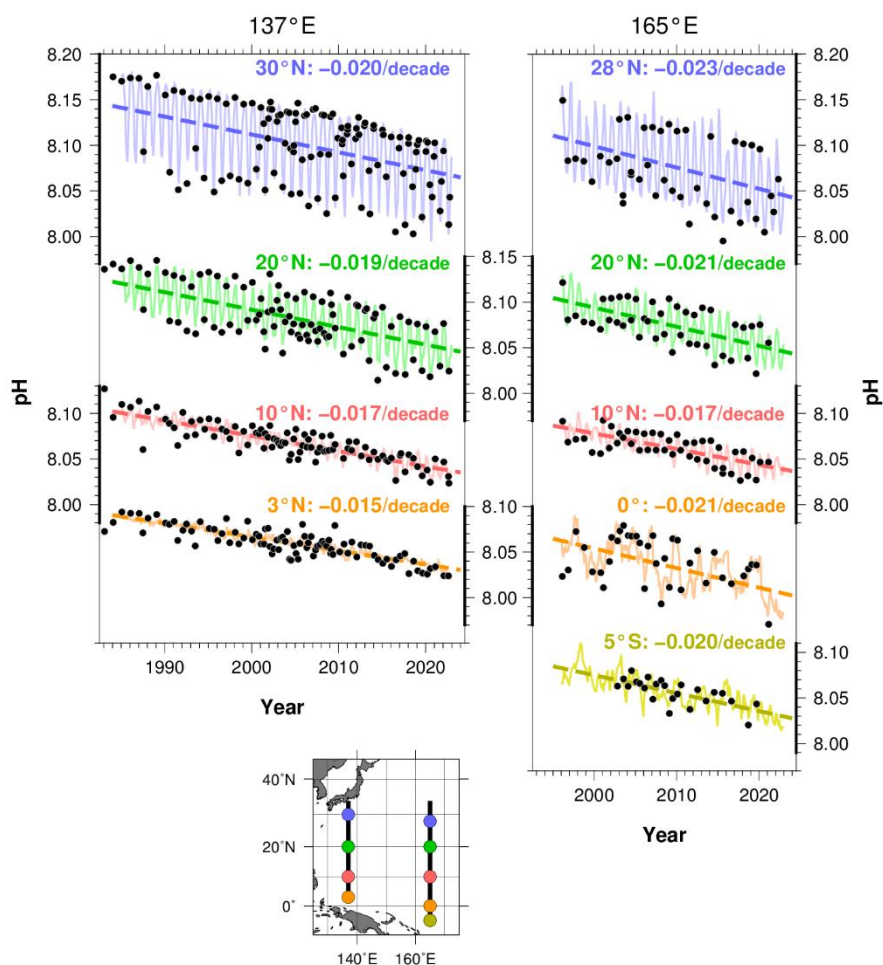


Figure 2.12-6 Long-term trends of pH at each latitude in JMA's repeat hydrographic lines at 137°E (left) and 165°E (right)

Black plots show pH observation values based on $p\text{CO}_2$ observation data. Solid lines represent monthly pH values reconstructed using the method of Ishii et al. (2011), dashed lines show the long-term trend of pH, and numbers indicate rates of change at each latitude.

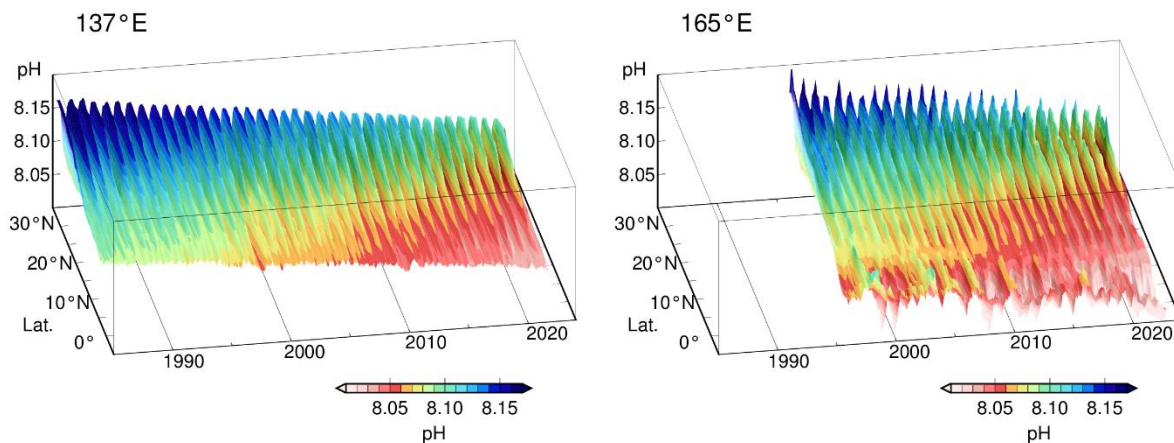


Figure 2.12-7 Time-latitude distribution of pH along the 137°E (left) and the 165°E (right) lines
 Colors indicate reconstructed monthly pH values. The part on the left shows pH along 137°E (3-34°N) since 1985, and the part on the right shows pH along 165°E (5°S-35°N) since 1996.

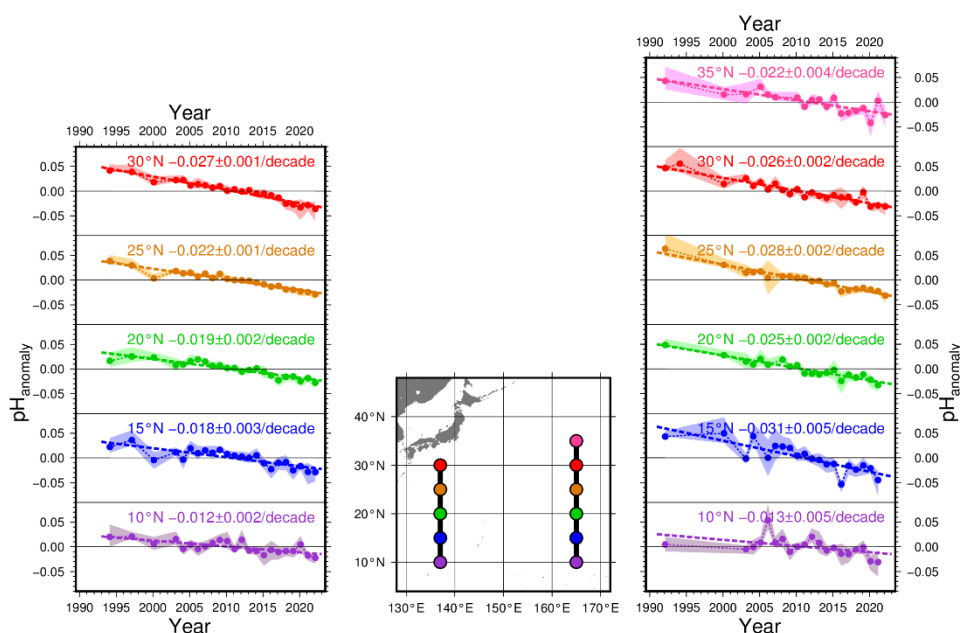


Figure 2.12-8 Long-term trends of pH between 25.0 σ_θ and 26.9 σ_θ (a depth range of about 150~800 m) along 137°E (left) and 165°E (right)
 Plots show pH anomalies from averages for the whole period on the isopycnals at each latitude. The shaded areas and bold dotted lines represent the standard deviation range ($\pm 1 \sigma$) and the long-term trend, respectively. The numbers indicate rates of change at each latitude.

(3) Ocean acidification in the global ocean

JMA has analyzed monthly sea surface pH values since 1990 using a global oceanographic observation database via the method outlined in 2.12-1 (2). The results show a clear trend of in-situ pH decrease at 0.019 per decade in the global ocean. The rates of decrease are 0.019, 0.018 and 0.020 pH per decade in the Pacific, the Atlantic and the Indian Ocean, respectively.

The pH in surface ocean waters varies by area due to differences in ocean circulation, biological activity and seasonal change. In the equatorial area, upwelling CO₂-rich seawater causes relatively low pH values. Subtropical (subpolar) areas show higher pH values than equatorial areas with seasonal changes of higher (lower) pH in winter and lower (higher) pH in summer.

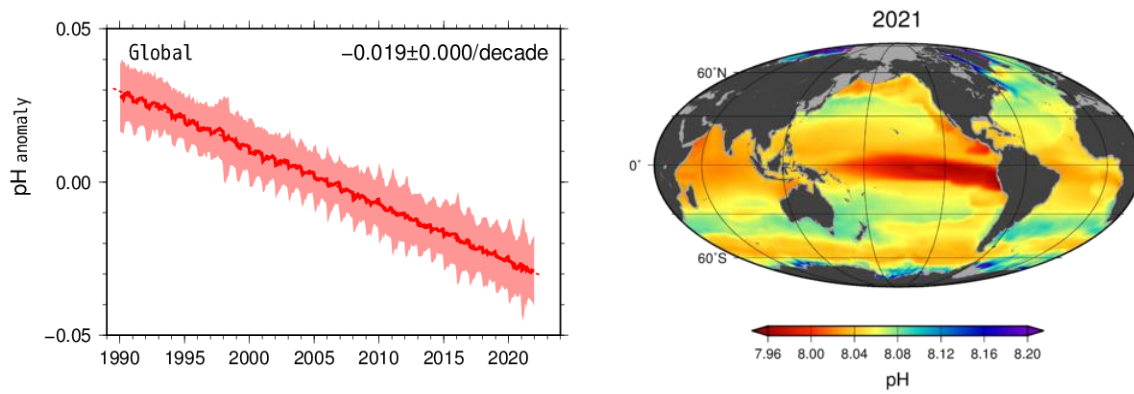


Figure 2.12-9 Long-term trend of surface ocean pH (left) and pH distribution in 2021 (right) in the global ocean

Left: Rate of pH change in the global ocean. The solid line is a time-series representation of the pH anomaly from the average from 1991 to 2020 in the global ocean. The shaded area and dotted line represent the standard deviation range ($\pm 1\sigma$) and the long-term trend, respectively. The ' \pm ' symbol indicates a 95% confidence interval.

Right: Lower pH values are represented as warmer colors..

Explanatory note on detection of statistical significance in long-term trends

Meteorological observation data, including those relating to temperature and precipitation, are subject to large amplitude fluctuations due to the influence of atmospheric and oceanic dynamics on a broad spectrum of spatial and temporal scales. To examine the possible presence of long-term climate system trends associated with global warming in consideration of natural variability, raw climate data need to be converted into suitable statistical time-series representations and subjected to statistical testing in order to highlight the likelihood of systematic temporal trends that cannot be explained by random variability alone. When the results of such testing allow reasonable conclusion that random variability is unlikely to be the sole factor at work, a change is described as statistically significant.

In this report, the likelihood of a systematic long-term change existing in a time-series representation is based on the results of statistical significance testing performed at confidence levels of 99, 95 and 90%. The following terminology summary describes each level:

Level of confidence	Term
$\geq 99\%$	Virtually certain to have increased/decreased (statistically significant at a confidence level of 99%)
$\geq 95\%$	Extremely likely to have increased/decreased (statistically significant at a confidence level of 95%)
$\geq 90\%$	Very likely to have increased/decreased (statistically significant at a confidence level of 90%)
Other than those above	No discernible trend

The following statistical methods are applied for the data used in this report:

- i) For statistical variables whose annual fluctuation component can be assumed to follow normal distribution
 For temperature anomalies, trend-removed annual variability data are expected to approximately follow normal distribution. T-testing is performed for statistical variables assumed to be normally distributed using a coefficient of correlation between years and values.

- ii) For statistical variables whose annual fluctuation component cannot be assumed to follow normal distribution
 The assumption of normality may not be applicable to frequency statistics regarding weather conditions, including those for extremely warm days, tropical nights and hourly precipitation amounts exceeding 50 mm. Accordingly, non-parametric testing, which does not depend on underlying assumptions about distribution, is applied to such variables.

It should be noted that statistical tests are in theory inevitably susceptible to the establishment of false conclusions even if the results indicate a statistically significant trend. Even outcomes indicating statistical

significance at confidence levels of 90, 95 or 99% imply that there are small inherent probabilities of up to 10, 5 and 1%, respectively, of the significance being erroneously detected when in fact the observed long-term change occurred by mere random chance. Conversely, when a systematic long-term change actually exists, statistical testing may fail to detect the significance correctly. In general, test results are not considered highly stable if they are based on observation records that are temporally limited, influenced by large annual fluctuations/rare events or subject to change when new observations are added to a data sequence. Readers are encouraged to interpret the analytical results presented in the report appropriately with due note of these considerations.

Glossary

Aerosols

Aerosols are airborne solids or liquids in fine particle form. Their many types include particles of natural origin blown up from land/sea surfaces, anthropogenic particles and secondary aerosols formed from anthropogenic and biogenic precursors. In addition to absorbing and scattering sunlight, they also provide condensation nuclei for clouds. Particulate matter 2.5 (PM_{2.5}) is the name given to aerosol particles measuring 2.5 micrometers or less in diameter (about 30 times thinner than a human hair), and is considered to have possible adverse effects on human health when inhaled.

Anthropogenic

Resulting from or produced by human activity.

Arctic Oscillation

The Arctic Oscillation (AO) is a major atmospheric circulation variation exhibiting an annular pattern of sea-level pressure anomalies in a seesaw fashion with one sign over the Arctic region and the opposite sign over the mid-latitudes. Its negative phase, which is characterized by positive and negative sea-level pressure anomalies over the Arctic region and the mid-latitudes, respectively, helps cold Arctic air move into the mid-latitudes. The positive phase, whose sea-level pressure anomaly pattern is reversed, keeps Arctic air over the Arctic region.

Extreme climate event

In general, an extreme climate event is recognized as an unusually severe or rare climate event creating disaster conditions or exerting significant socio-economic influence. The definition includes severe weather conditions covering periods ranging from only a few hours (such as heavy rain or strong wind) to several months (such as drought or cold summer conditions). JMA defines extreme climate events as those occurring once every 30 years or longer.

IPCC (Intergovernmental Panel on Climate Change)

The Intergovernmental Panel on Climate Change (IPCC) is an international organization established by the United Nations Environment Programme (UNEP) and the World Meteorological Organization (WMO) in 1988. It reviews and assesses scientific, technical and socio-economic information on climate change, the potential impacts of such change and related vulnerability, and options for adaptation and mitigation, in collaboration with scientists and experts on an international basis. The Panel's reports highlight common understanding of such information to support political matters such as treaty negotiations on global warming.

Kosa (Aeolian dust)

Kosa (Aeolian dust) is a meteorological phenomenon in which fine dust is blown up to an altitude of several thousand meters by cyclonic or other wind systems from deserts or cropland in semi-arid areas of the Asian continent, and is transported over long distances by westerly winds, resulting in haze or dustfall in downstream areas. It is often observed between March and June in Japan and makes the sky yellow and hazy. Heavy Kosa can affect transportation by obstructing visibility.

Monsoon

The term *monsoon* primarily refers to seasonally reversing winds, and by extension includes related seasonal rainfall change with wet and dry phases. Monsoon climate regions where seasonal winds prevail are found in numerous places around the world, with a major one located over a broad area from the Asian continent to northern Australia.

Normals

Normals represent climatic conditions at meteorological stations, and are used as a base to evaluate meteorological variables (e.g., temperature, precipitation and sunshine duration) and produce generalizations (e.g., cool summer, warm winter and dry/wet months) for particular periods. JMA uses averages for the most recent three decades (currently 1991 – 2020) as normals, which are updated every decade in line with WMO Technical Regulations.

Terms relating to surface temperature variations

El Niño/La Niña events: In an El Niño event, sea surface temperatures (SSTs) are higher than normal across a wide region from near the date line to the area off the coast of South America in the equatorial Pacific for about a year. In a La Niña event, SSTs are lower than normal in the same area. Both occur every few years, and are associated with frequent extreme climate conditions worldwide.

JMA recognizes the occurrence of an El Niño event when the five-month running mean of SST deviations from the climatological means (based on a sliding 30-year period averaged over the NINO.3 El Niño Monitoring Region (5°N – 5°S, 150°W – 90°W; Figure A)) remains +0.5°C or above for a period of six months or more. Similarly, a La Niña event is recognized when the corresponding figure is –0.5°C or below for the same area/period.

Figure B shows typical SST deviations from the normal during El Niño and La Niña events. The dark red and blue shading seen from the date line to the coast of South America indicates large deviations.

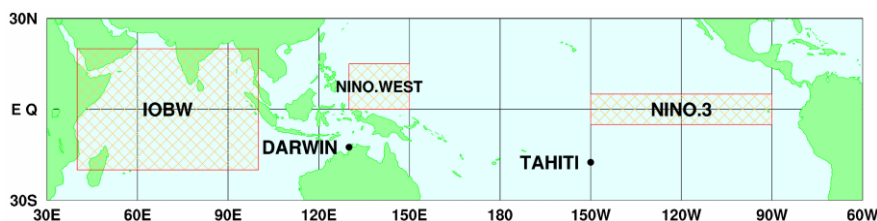


Figure A El Niño monitoring regions

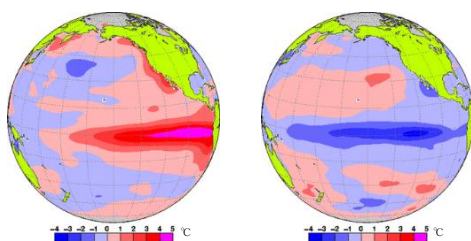


Figure B Left: monthly mean SST anomalies for El Niño (November 1997); right: for La Niña (December 1998)

Red and blue shading represents positive and negative SST deviations, respectively. Darker shading indicates larger deviations. The unit of temperature is degrees Celsius.

Southern Oscillation: El Niño and La Niña events are closely related to trade winds (easterlies blowing around the tropical Pacific), which tend to be weak during the former and strong during the latter. The strength of such winds is closely related to the sea level pressure difference between eastern and western parts of the Pacific. This pressure difference varies in a phenomenon known as the Southern Oscillation. El Niño/La Niña events and the Southern Oscillation are not independent of each other; they are different manifestations of the same phenomenon involving atmospheric and oceanic interaction, and are referred to as ENSO (El Niño – Southern Oscillation) for short.

Pacific Decadal Oscillation (PDO): A phenomenon in which variables in the atmosphere and oceans tend to co-vary with a period of more than ten years in the North Pacific. When sea surface temperatures are lower (higher) than their normals in the central part of the North Pacific, those in its part along the coast of North America are likely to be higher (lower) than their normals, and sea level pressures in the high latitudes of the North Pacific are likely to be lower (higher) than their normals. These atmospheric variations affect meteorological conditions in North America and elsewhere.

Indian Ocean Dipole mode (IOD) event: A phenomenon in which sea surface temperatures (SSTs) are below normal in the south eastern part of tropical Indian Ocean (off the Sumatra Island) and above normal in the western part during the northern hemisphere summer and autumn (June - November). This east-west contrast of SST anomaly pattern is called dipole mode. On the other hand, a phenomenon in which SSTs are above normal off the Sumatra Island and below normal in the western part is called negative IOD event. These phenomena affect the climate near Japan and Australia through the changes of atmospheric circulation caused by atmospheric active (inactive) convections over above (below) normal SST area.

Terms relating to the greenhouse effect

Greenhouse effect: The earth's atmosphere contains small amounts of greenhouse gases, which absorb a large part of the infrared radiation emitted from the earth's surface and re-emit it back, thereby warming the surface. This process is known as the greenhouse effect. Without it, the earth's average surface temperature of around 14°C would be approximately -19°C. Increased concentrations of greenhouse gases enhance the greenhouse effect, thereby producing higher surface temperatures. Major greenhouse gases include carbon dioxide, methane and nitrous oxide. Although water vapor has the strongest greenhouse effect, its main influencing factor is temperature rather than emissions relating to human activity. Water vapor is not usually regarded as a greenhouse gas in the context of global warming because it is considered a feedback factor rather than a forcing factor in climate change.

Carbon dioxide: Of all greenhouse gases, carbon dioxide (CO₂) is the most significant contributor to global warming. Since the start of the industrial era in the mid-18th century, related atmospheric concentrations have increased as a result of emissions associated with human activity such as fossil fuel combustion, cement production and land-use change (e.g., deforestation). Around half of all cumulative anthropogenic CO₂ emissions have remained in the atmosphere. The rest was removed from the atmosphere and stored in natural terrestrial ecosystems and oceans (IPCC, 2021).

Methane: Methane (CH₄) is the second most significant greenhouse gas after CO₂, and has a significant radiative effect around 27.9 times greater than that of CO₂ per unit mass. Around 40% of CH₄ released into the atmosphere is of natural origin (wetlands, termites, etc.), and around 60% is from human-related activity sources (ruminant animals, rice paddy fields, fossil fuel mining, landfill, biomass burning, etc.) (WMO, 2022). CH₄ has a short atmospheric lifetime (approx. 11.8 years) because it is primarily removed from the atmosphere via photochemical reaction with reactive and unstable hydroxyl (OH) radicals.

Nitrous oxide: Nitrous oxide (N₂O) is a significant greenhouse gas because of its large radiative effect per unit mass (about 273 times greater than that of CO₂) and its long lifetime (about 109 years) in the atmosphere. Around 57% of N₂O released into the atmosphere is of natural origin (oceans, soil, etc.), and around 43% is from human activity-related sources (biomass burning, nitrate fertilizers, various industrial processes, etc.) (WMO, 2022). It is photo-dissociated in the stratosphere by ultraviolet radiation.

Halocarbons: Halocarbons are generally carbon compounds containing halogens such as chlorine and bromine, many of which are powerful greenhouse gases whose atmospheric concentrations have increased rapidly since the second half of the 20th century due to artificial production. Although their atmospheric concentrations are only around a millionth those of CO₂, their greenhouse effect per unit mass is several thousand times greater. Chlorofluorocarbons (CFC-11, CFC-12 and CFC-113 among others), carbon tetrachloride, hydrochlorofluorocarbons (HCFCs), 1,1,1-trichloroethane, chloromethane, halons and bromomethane are greenhouse gases and ozone-depleting substances (ODSs). Hydrofluorocarbons (HFC-134a, HFC-152a, etc.) are also included in the definition.

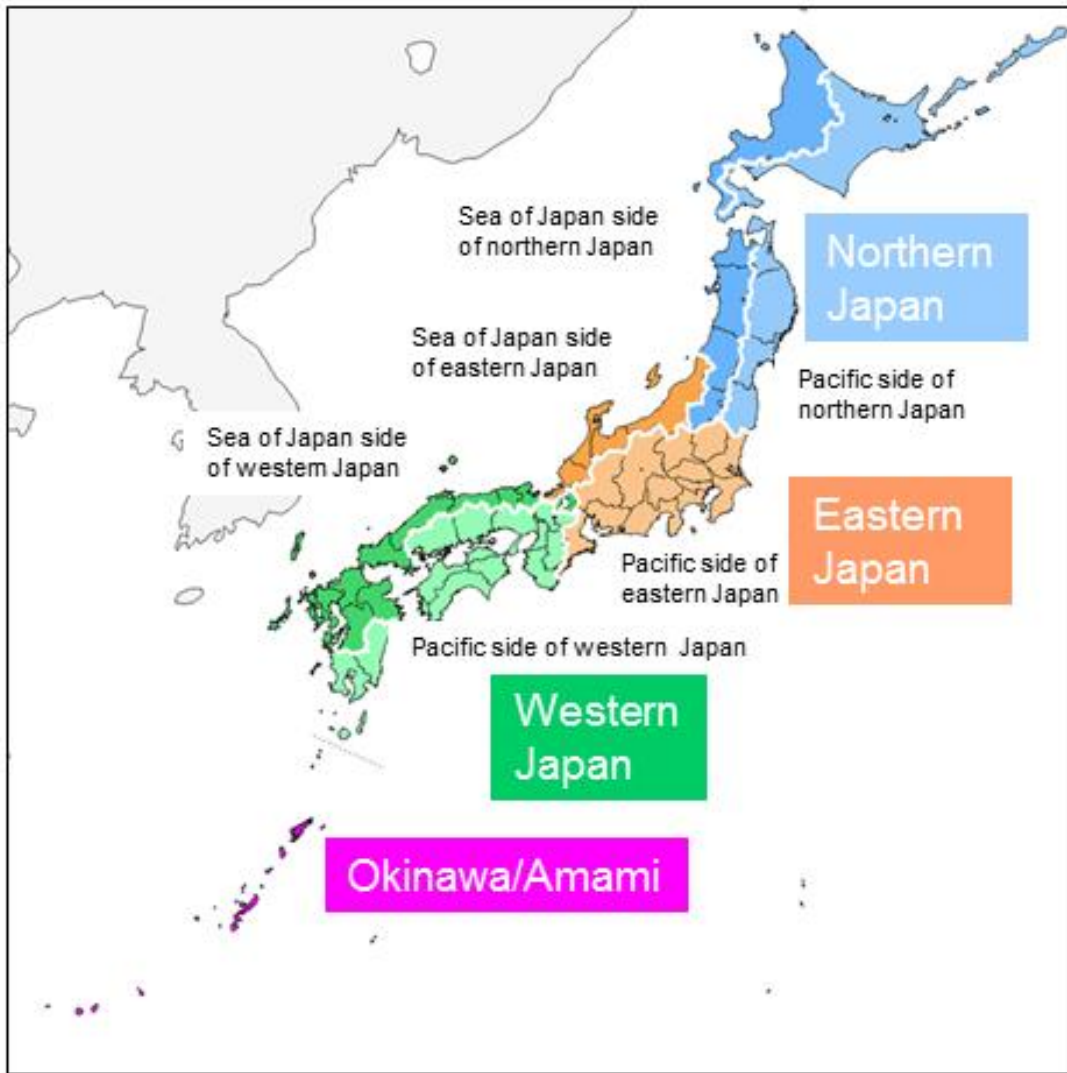
Montreal Protocol: The Montreal Protocol on Substances that Deplete the Ozone Layer (a protocol to the Vienna Convention for the Protection of the Ozone Layer) is an international treaty designed to protect the ozone layer by phasing out the production of numerous substances believed to be responsible for ozone depletion. The treaty was opened for signatures in 1987 and came into force in 1989. Since then, it has undergone several revisions. Japan ratified the protocol in 1988.

ppm, ppb, ppt: In this report, greenhouse gas concentrations are described in terms of mole fractions in units of ppm/ppb/ppt, representing the numbers of molecules of the gas per million/billion/trillion molecules of dry air, respectively.

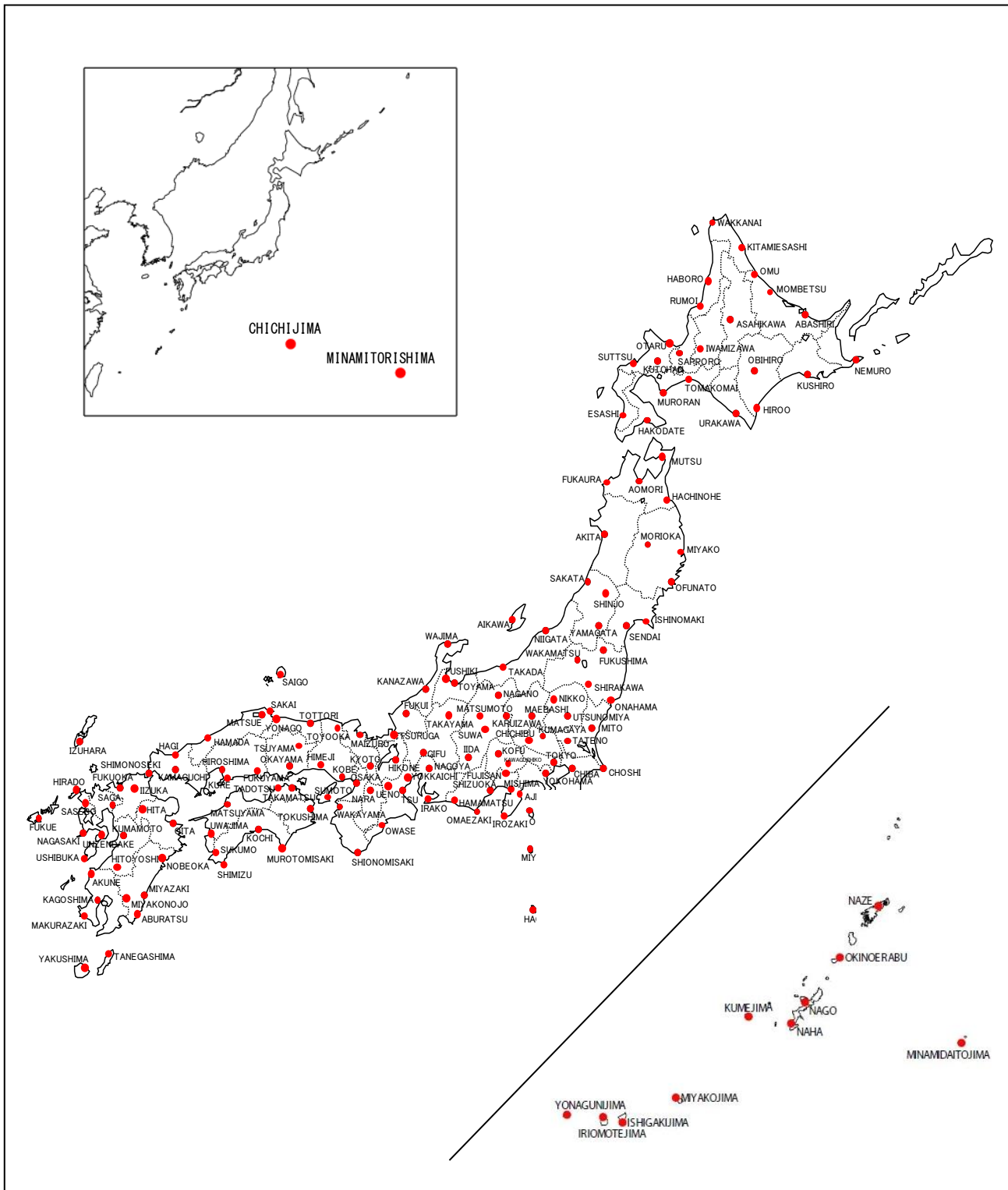
Terms relating to water masses

North Pacific Subtropical Mode Water (NPSTMW) area: A thermostat between the seasonal and main thermoclines. The NPSTMW area is considered to form in the surface mixed layer just south of the Kuroshio Extension as a result of huge heat loss in winter. It is defined as an area of 16 – 18-degree water at depths of 100 to 400 m at around 20 to 30°N along the 137°E line.

North Pacific Intermediate Water (NPIW) area: The NPIW area forms in the mixed region between the Kuroshio Extension and the Oyashio front. It is defined as water with a salinity level of 34.0 or less at a depth of around 800 m at around 20 to 30°N along the 137°E line.



Names of Japanese regions used in this report



Distribution of surface meteorological observation stations in Japan

References

News

- Carn, S. A. et al., 2022: Out of the blue: Volcanic SO₂ emissions during the 2021–2022 eruptions of Hunga Tonga—Hunga Ha’apai (Tonga), *Front. Earth Sci.*, 10:976962, <https://doi.org/10.3389/feart.2022.976962>.
- Feng, L. et al., 2022: Methane emissions responsible for record-breaking atmospheric methane growth rates in 2020 and 2021, *Atmos. Chem. Phys. Discuss.* [preprint], <https://doi.org/10.5194/acp-2022-425>, in review.
- IPCC, 2013: *Climate Change 2013: The Physical Science Basis. Contribution of Working Group I to the Fifth Assessment Report of the Intergovernmental Panel on Climate Change* [Stocker, T.F., D. Qin, G.-K. Plattner, M. Tignor, S.K. Allen, J. Boschung, A. Nauels, Y. Xia, V. Bex and P.M. Midgley (eds.)]. Cambridge University Press, Cambridge, United Kingdom and New York, NY, USA, 1535 pp.
- IPCC, 2019: *IPCC Special Report on the Ocean and Cryosphere in a Changing Climate* [H.-O. Pörtner, D.C. Roberts, V. Masson-Delmotte, P. Zhai, M. Tignor, E. Poloczanska, K. Mintenbeck, A. Alegría, M. Nicolai, A. Okem, J. Petzold, B. Rama, N.M. Weyer (eds.)]. Cambridge University Press, Cambridge, UK and New York, NY, USA, 755 pp. <https://doi.org/10.1017/9781009157964>.
- IPCC, 2021: *Climate Change 2021: The Physical Science Basis. Contribution of Working Group I to the Sixth Assessment Report of the Intergovernmental Panel on Climate Change* [Masson-Delmotte, V., P. Zhai, A. Pirani, S.L. Connors, C. Péan, S. Berger, N. Caud, Y. Chen, L. Goldfarb, M.I. Gomis, M. Huang, K. Leitzell, E. Lonnoy, J.B.R. Matthews, T.K. Maycock, T. Waterfield, O. Yelekçi, R. Yu, and B. Zhou (eds.)]. Cambridge University Press, Cambridge, United Kingdom and New York, NY, USA, 2391 pp. doi:10.1017/9781009157896.
- Khaykin, S. et al., 2022: Global perturbation of stratospheric water and aerosol burden by Hunga eruption, *Commun. Earth Environ.*, 3, 316, <https://doi.org/10.1038/s43247-022-00652-x>.
- Kitajima, T. et al., 2021: *Weather Service Bulletin (Sokko-Jiho)*, 88, 19-28 (in Japanese).
- Kuroda, H. and T. Setou, 2021: Extensive Marine Heatwaves at the Sea Surface in the Northwestern Pacific Ocean in Summer 2021. *Remote Sens.* 2021, 13, 3989. <https://doi.org/10.3390/rs13193989>.
- Legras, B. et al., 2022: The evolution and dynamics of the Hunga-Tonga Ha’apai sulfate aerosol plume in the stratosphere, *Atmos. Chem. Phys.*, 22, 14957–14970, <https://doi.org/10.5194/acp-22-14957-2022>.
- Millán, L. et al., 2022: The Hunga Tonga-Hunga Ha'apai hydration of the stratosphere, *Geophys. Res. Lett.*, 49, e2022GL099381, <https://doi.org/10.1029/2022GL099381>.
- Miyama T, Minobe S and H. Goto, 2021: Marine Heatwave of Sea Surface Temperature of the Oyashio Region in Summer in 2010–2016. *Front. Mar. Sci.* 7:576240. doi: 10.3389/fmars.2020.576240.
- Poli, P. and N. M. Shapiro, 2022: Rapid characterization of large volcanic eruptions: Measuring the impulse of the Hunga Tonga Ha’apai explosion from teleseismic waves, *Geophys. Res. Lett.*, 49, e2022GL098123, <https://doi.org/10.1029/2022GL098123>.
- Proud, S. R., A. T. Prata and S. Schmauss, 2022: The January 2022 eruption of Hunga Tonga-Hunga Ha’apai volcano reached the mesosphere, *Science*, 378, 554–557, <https://doi.org/10.1126/science.abo4076>.
- Sellitto, P. et al., 2022: The unexpected radiative impact of the Hunga Tonga eruption of 15th January 2022, *Commun. Earth Environ.*, 3, 288, <https://doi.org/10.1038/s43247-022-00618-z>.
- Taha, G. et al., 2022: Tracking the 2022 Hunga Tonga-Hunga Ha'apai aerosol cloud in the upper and middle stratosphere using space-based observations, *Geophys. Res. Lett.*, 49, e2022GL100091, <https://doi.org/10.1029/2022GL100091>.

- Witze, A., 2022: Why the Tongan volcanic eruption was so shocking, *Nature*, 602, 376–378, <https://doi.org/10.1038/d41586-022-00394-y>
- WMO, 2009: Technical report of global analysis method for major greenhouse gases by the World Data Center for Greenhouse Gases. GAW Report , 184, WMO/TD, 1473.
- WMO, 2022: WMO Greenhouse Gas Bulletin, 18. https://library.wmo.int/index.php?lvl=notice_display&id=3030
- WMO, 2023: WMO WDCGG DATA SUMMARY, WDCGG No.47, GAW Data Volume IV-Greenhouse Gases and Other Atmospheric Gases, published by the Japan Meteorological Agency in co-operation with World Meteorological Organization. Available at <https://gaw.kishou.go.jp/publications/summary>. (in preparation)
- Xu, J. et al., 2022: Large amounts of water vapor were injected into the stratosphere by the Hunga Tonga–Hunga Ha’apai volcano eruption, *Atmosphere*, 13, 912, <https://doi.org/10.3390/atmos13060912>.
- Yamauchi, T., 1995: Statistical analysis of atmospheric turbidity over Japan: The influence of three volcanic eruptions, *J. Meteor. Soc. Japan*, 73, 91-103.
- Yoshida, M. et al., 2018: Common retrieval of aerosol properties for imaging satellite sensors, *J. Meteor. Soc. Japan*, 96B, 193-109, doi:10.2151/jmsj.2018-039.
- Zhang, H. et al., 2022: Potential impact of Tonga volcano eruption on global mean surface air temperature, *J. Meteor. Res.*, 36(1), 1–5, doi: 10.1007/s13351-022-2013-6.
- Zhu, Y. et al., 2022: Perturbations in stratospheric aerosol evolution due to the water-rich plume of the 2022 Hunga-Tonga eruption, *Commun. Earth Environ.*, 3, 248, <https://doi.org/10.1038/s43247-022-00580-w>.

Chapter 1

- EM-DAT: The OFDA/CRED International Disaster, Database – www.emdat.be – Université Catholique de Louvain – Brussels – Belgium
- JMA, 1997: Monthly Report on Climate System, June 1997.
- Ishii, M., A. Shouji, S. Sugimoto and T. Matsumoto, 2005: Objective Analyses of Sea-Surface Temperature and Marine Meteorological Variables for the 20th Century Using ICOADS and the KOBE Collection. *Int. J. of Climatology*, 25, 865-879.
- Kobayashi et al., 2015: The JRA-55 Reanalysis: General specifications and basic characteristics. *J. Meteor. Soc. Japan.*, 93, 5-48.

Chapter 2

- Aono and Saito, 2010: Cherry blossom phenology and temperature reconstructions at Kyoto. <http://atmenv.envi.osakafu-u.ac.jp/aono/kyophenotemp4/>
- Dettinger, M. D. and M. Ghil, 1998: Seasonal and interannual variations of atmospheric CO₂ and climate. *Tellus*, 50B, 1–24.
- Friedlingstein, P., et al., 2022: Global Carbon Budget 2022, *Earth Syst. Sci. Data*, doi:10.5194/essd-14-4811-2022.
- Fujibe, F., 1999: Time of observation bias in the climatological data of daily minimum and maximum temperature in Japan. *Tenki*, 46, 819-830 (in Japanese with English abstract)
- Iida, Y., et al., 2021: Global trends of ocean CO₂ sink and ocean acidification: an observation-based reconstruction of surface ocean inorganic carbon variables. *J. Oceanogr.*, doi.org/10.1007/s10872-020-00571-5.
- IPCC, 2019: IPCC Special Report on the Ocean and Cryosphere in a Changing Climate [H.-O. Pörtner, D.C. Roberts, V. Masson-Delmotte, P. Zhai, M. Tignor, E. Poloczanska, K. Mintenbeck, A. Alegría, M. Nicolai,

- A. Okem, J. Petzold, B. Rama, N.M. Weyer (eds.]. Cambridge University Press, Cambridge, UK and New York, NY, USA, 755 pp. <https://doi.org/10.1017/9781009157964>.
- IPCC, 2021: Climate Change 2021: The Physical Science Basis. Contribution of Working Group I to the Sixth Assessment Report of the Intergovernmental Panel on Climate Change [Masson-Delmotte, V., P. Zhai, A. Pirani, S.L. Connors, C. Péan, S. Berger, N. Caud, Y. Chen, L. Goldfarb, M.I. Gomis, M. Huang, K. Leitzell, E. Lonnoy, J.B.R. Matthews, T.K. Maycock, T. Waterfield, O. Yelekçi, R. Yu, and B. Zhou (eds.)]. Cambridge University Press, Cambridge, United Kingdom and New York, NY, USA, 2391 pp. doi:10.1017/9781009157896.
- Ishii, M., A. Shouji, S. Sugimoto and T. Matsumoto, 2005: Objective Analyses of Sea-Surface Temperature and Marine Meteorological Variables for the 20th Century Using ICOADS and the KOBE Collection. *Int. J. of Climatology*, 25, 865-879.
- Ishii, M., Y. Fukuda, H. Hirahara, S. Yasui, T. Suzuki, and K. Sato, 2017: Accuracy of Global Upper Ocean Heat Content Estimation Expected from Present Observational Data Sets. *SOLA*, Vol. 13, 163-167, doi:10.2151/sola.2017-030.
- Keeling, C. D., et al., 1995: Interannual extremes in the rate of rise of atmospheric carbon dioxide since 1980. *Nature*, 375, 666–670.
- Keeling, R. F., et al., 1996: Global and hemispheric CO₂ sinks deduced from changes in atmospheric O₂ concentration. *Nature*, 381, 218-221.
- Kudo, R., et al., 2012: Aerosol impact on the brightening in Japan. *J. Geophys. Res.*, 117(D07208), doi:10.1029/2011JD017158.
- Le Quéré, C., et al., 2016: Global Carbon Budget 2016, *Earth Syst. Sci. Data*, 8, 605-649, doi:10.5194/essd-8-605-2016.
- Mantua, N. J. and S. R. Hare, 2002: The Pacific Decadal Oscillation. *J. Oceanogr.*, 58, 35 – 44, doi: 10.1023/A:1015820616384.
- Montzka, S. A. et al., 2018: An unexpected and persistent increase in global emissions of ozone-depleting CFC-11, *Nature*, 557, 413-417, doi:10.1038/s41586-018-0106-2.
- Montzka, S. A. et al., 2021: A decline in global CFC-11 emissions during 2018-2019. *Nature*, 590, 428-432, <https://doi.org/10.1038/s41586-021-03260-5>.
- Niwa, Y., et al., 2014: Seasonal Variations of CO₂, CH₄, N₂O and CO in the Mid-Troposphere over the Western North Pacific Observed Using a C-130H Cargo Aircraft. *J. Meteorol. Soc. Japan*, 92(1), 50-70, doi:10.2151/jmsj.2014-104.
- Norris, J. R., and M. Wild, 2009: Trends in aerosol radiative effects over China and Japan inferred from observed cloud cover, solar “dimming,” and solar “brightening.”. *J. Geophys. Res.*, 114(D00D15), doi:10.1029/2008JD011378.
- Ohmura, A., 2009: Observed decadal variations in surface solar radiation and their causes. *J. Geophys. Res.*, 114(D00D05), doi: 10.1029/2008JD011290.
- Park, S., et al., 2021: A decline in emissions of CFC-11 and related chemicals from eastern China. *Nature*, 590, 433-437, <https://doi.org/10.1038/s41586-021-03277-w>.
- Rayner, P. J., et al., 1999: Reconstructing the recent carbon cycle from atmospheric CO₂, δ¹³C and O₂/N₂ observations. *Tellus*, 51B, 213-232.
- Rigby, M., et al., 2019: Increase in CFC-11 emissions from eastern China based on atmospheric observations, *Nature*, 569, 546-550, doi:10.1038/s41586-019-1193-4.
- Saito, T., et al., 2015: Extraordinary halocarbon emissions initiated by the 2011 Tohoku earthquake. *Geophys. Res. Lett.*, 42, doi:10.1002/2014GL062814.

- Sweeney, C., et al., 2015: Seasonal climatology of CO₂ across North America from aircraft measurements in the NOAA/ESRL Global Greenhouse Gas Reference Network, *J. Geophys. Res. Atmos.*, 120, 5155-5190, doi:10.1002/2014JD022591.
- Tsuboi, K., et al., 2013: Evaluation of a new JMA aircraft flask sampling system and laboratory trace gas analysis system. *Atmos. Meas. Tech.*, 6, 1257–1270, doi:10.5194/amt-6-1257-2013.
- Umezawa, T., et al., 2018: Seasonal evaluation of tropospheric CO₂ over the Asia-Pacific region observed by the CONTRAIL commercial airliner measurements, *Atmos. Chem. Phys.*, 18, 14851-14866, doi:10.5194/acp-18-14851-2018.
- WCRP, 2010: Summary Report from the Eleventh Baseline Surface Radiation Network (BSRN) Scientific Review and Workshop. WCRP Informal Report No. 08/2010, 21pp.
- Wild, M., 2009: Global dimming and brightening: A review. *J. Geophys. Res.*, 114(D00D16), doi:10.1029/2008JD011470.
- Wild, M. and A. Ohmura, 2004: BSRN longwave downward radiation measurements combined with GCMs show promise for greenhouse detection studies. *GEWEX news*, 14, 4, 20 pp.
- WMO, 2009: Technical report of global analysis method for major greenhouse gases by the World Data Center for Greenhouse Gases. GAW Report , 184, WMO/TD, 1473.
- WMO, 2018a: Scientific assessment of ozone depletion: 2018. Global Ozone Research and Monitoring Project-Report, 58.
- WMO, 2018b: WMO Greenhouse Gas Bulletin, 14.
https://library.wmo.int/index.php?lvl=notice_display&id=3030
- WMO, 2022: WMO Greenhouse Gas Bulletin, 18.
https://library.wmo.int/index.php?lvl=notice_display&id=3030
- WMO, 2023: WMO WDCGG DATA SUMMARY, WDCGG No.47, GAW Data Volume IV-Greenhouse Gases and Other Atmospheric Gases, published by the Japan Meteorological Agency in co-operation with World Meteorological Organization. Available at <https://gaw.kishou.go.jp/publications/summary>. (in preparation)